Mass Photometry: Weighing Single Molecules with Interferometric Scattering Microscopy



Gavin Young

Magdalen College

University of Oxford

A thesis submitted for the degree of

Doctor of Philosophy in Theoretical and Physical Chemistry

10th October, 2019

Acknowledgements

Over the course of this work, I have been lucky enough to be supported by a great many wonderful people both scientifically and personally. I should also mention the financial support provided to me by Magdalen College through their Zvi and Ofra Meitar graduate scholarship, which has enabled me to study here and for which I am very grateful.

Firstly, I would like to thank my supervisor, Philipp Kukura, for the seemingly endless stream of ideas to try and readily available guidance on how best to progress, and also for running the group in such a way as to create a friendly, co-operative working environment. Indeed, the Kukura group has been a lively and exciting place to work both inside the lab and out, with very free discussion of ideas, no matter how silly they seem, over coffee, food and beers. In particular, I thank Dan Cole for his major role in my development as a scientist and the development of the projects described in this thesis, initially teaching me how to build an iSCAT microscope, and then working so closely with me on the work presented in Chapter 3 especially. Special thanks should also go to the 'bio-postdocs' Joanna Andrecka, Nikolas Hundt and Manish Kushwah for teaching me not to be afraid of the wet lab and for running the more involved assays, and also to Max Hantke and Adar Sonn-Segev for very fruitful discussions around the data analysis.

It has also been a pleasure to work with several collaborators on various projects over the past few years, and I thank them both for their thoughts on what directions to take with respect to developing mass photometry and for

providing countless samples to measure. Weston Struwe, and Justin Benesch and his group deserve particular mention in this regard.

Last but not least, I would like to thank my parents and brothers for their all round support, encouragement and entertainment over the years.

Statement of Originality

The research described in this thesis was carried out by the author between October 2015 and September 2019 and includes nothing which is the outcome of work done in collaboration, except where specifically indicated in the text. The use of the first person plural is strictly a matter of style in keeping with standard scientific convention.

List of Publications

The work carried out by the author between October 2015 and September 2019 led to the following publications:

1. D. Cole*, G. Young*, A. Weigel, A. Sebesta and P. Kukura, Label-Free Single-Molecule Imaging with Numerical-Aperture-Shaped Interferometric Scattering Microscopy, *ACS Photonics*, 4, 211-216 (2017).

2. G. Young*, N. Hundt*, D. Cole, A. Fineberg, J. Andrecka, A. Tyler, A. Olerinyova, A. Ansari, E. G. Marklund, M. P. Collier, S. A. Chandler, O. Tkachenko, J. Allen, M. Crispin, N. Billington, Y. Takagi, J. R. Sellers, C. Eichmann, P. Selenko, L. Frey, R. Riek, M. R. Galpin, W. B. Struwe, J. L. P. Benesch and P. Kukura, Quantitative mass imaging of single biological macromolecules, *Science*, 360, 423-427 (2018).

3. K. Haeussermann, G. Young, P. Kukura and H. Dietz, Dissecting FOXP2 oligomerization and DNA binding, *Angewandte Chemie*, 131, 7744–7749 (2019).

4. G. Young and P. Kukura, Interferometric Scattering Microscopy, *Annual Review of Physical Chemistry*, 70, 301-322 (2019).

Abstract

Interferometric scattering microscopy (iSCAT) has emerged in recent years as a highly sensitive imaging technique, capable of detecting the scattering signal even from single unlabelled proteins in suitably designed *in vitro* single molecule assays where the scattering background is kept to a minimum. Here we present numerical aperture filtering in an iSCAT microscope for enhanced contrast of point-like scatterers, and show that it can lead to improved sensitivity through enabling the use of higher incident light intensities.

We apply this development to measuring the scattering contrast of proteins at the single molecule level. This scattering contrast shows the expected linear dependence on molecular weight, allowing the extraction of mass distributions built up from the quantification of one molecule at a time, an approach we refer to as mass photometry. The mass measured in this way shows $\sim$2% mass accuracy and $\sim$2% precision. Distinct species are resolved with a full width at half maximum as low as 20 kDa, although this increases with mass, sufficient for low-order homo-oligomeric resolution. These capabilities are exemplified with measurements of the equilibrium constants for the BanLec-induced aggregation of the HIV protein Env, and dynamic imaging of the early stages of α-synuclein aggregation on supported lipid bilayers. We conclude with a detailed discussion of considerations relevant to the acquisition and analysis of high quality, reproducible mass photometry data.

Contents

List of Figures **v**

List of Abbreviations **vii**

1 Introduction **1**

2 Interferometric Scattering Microscopy: Background and Overview **5**

2.1 Introduction 5

2.1.1 Scattering and Absorption as a Contrast Mechanism . 6

2.1.2 Interference-based Microscopy 9

2.1.3 Ultrasensitive Extinction Microscopy 12

2.1.4 Interferometric Scattering microscopy 14

2.2 Single-Particle Tracking 15

2.2.1 High-Speed Single Particle Tracking 16

2.2.2 High Precision Single-Particle Tracking 18

2.2.3 Tracking Molecules on Cells 19

2.3 Label-Free Imaging of Nanoscopic Assembly 21

2.3.1 Label-Free Tracking 23

2.3.2 Lipid Assemblies and Their Dynamics 23

2.3.3 Virus Particle Dynamics 25

2.4 Label-Free Single-Molecule Imaging 26

2.4.1 Nonresonant Single-Protein Detection and Imaging . . 28

2.5 Conclusion 30

3 Experimental Methods, Data Analysis, Observations and Limitations of Mass Photometry **31**

3.0.1 Contributions 32

3.1 Light scattering 32

3.2 iSCAT microscopy 37

3.3 Standard Experimental Procedure 43
3.4 Data Analysis Routine 44
3.4.1 Analysis of Protein Binding Events 46
3.4.2 Analysis of Mobile Proteins on Supported Lipid Bilayers 58
3.5 Observations and Considerations 63
3.5.1 Determination of Optimal Focus Position 63
3.5.2 Selection of Optimal Averaging Window 65
3.5.3 Spatial Correlation of Binding Events 68
3.6 Limitations and Future Directions 72
3.6.1 Mass Resolution 72
3.6.2 Precision 76
3.6.3 Sensitivity 81

4 Numerical Aperture Filtering in Interferometric Scattering Microscopy 85
4.0.1 Contributions 85
4.1 Introduction 85
4.2 Results and Discussion 90
4.2.1 Increased Scattering Contrast 90
4.2.2 Single-molecule Sensitivity 93
4.2.3 Effect on Larger Scatterers 95
4.2.4 NA Filtering in Combination with Beam-scanning Illumination 97
4.3 Conclusions 99
4.4 Methods 101

5 Mass Photometry 105
5.0.1 Contributions 105
5.1 Introduction 106
5.2 Results and Discussion 109
5.2.1 Validation and Characterisation 109
5.2.2 Beyond Amino Acids 116
5.2.3 Quantifying Protein-Protein Interactions 119
5.2.4 Surface vs Solution Distributions 121
5.2.5 Imaging Mass Photometry 126
5.3 Conclusions 129
5.4 Methods 132

6 Summary and Outlook **141**

References **147**

List of Figures

2.1 Sensitivity limits of light microscopy illustrated with tubulin and microtubules. 7

2.2 Tracking of molecular motors with gold nanoparticle labelling with high spatial precision and temporal resolution. 18

2.3 iSCAT tracking on cells. 20

2.4 Label-free imaging of nanoscopic (dis)assembly. 22

2.5 Label-free single-particle tracking. 24

2.6 Label-free imaging of lipid assemblies. 25

2.7 Nonresonant label-free imaging of single biomolecules. 29

3.1 Scattering by small particles 34

3.2 Schematic of typical iSCAT microscope 39

3.3 Example of size filtering ratiometric images. 48

3.4 Workflow of the particle detection algorithm. 50

3.5 Example of model PSF fitting. 55

3.6 Time-dependence of a protein binding signal under ratiometric processing. 57

3.7 Comparison of the two background estimation approaches. . . 59

3.8 Tracking of unlabelled protein molecules diffusing on a supported lipid bilayer. 62

3.9 Glass contrast vs focus position. 65

3.10 Effect of averaging time on measured mass distributions. 67
3.11 Spatial distribution of binding events. 71
3.12 Influence of local reflectivity on protein contrast. 74
3.13 Precision on the mean contrast within a single acquisition. . . 78
3.14 Limitations in the detection of small species. 82

4.1 Concept and realisation of numerical aperture-filtered interferometric scattering microscopy. 89
4.2 Effect of a partial reflector on iSCAT contrast. 92
4.3 Ratiometric iSCAT imaging for detection of weak scatterers. . 93
4.4 Large field-of-view single protein detection. 94
4.5 Normalised iSCAT image of a single microtubule bound non-specifically to microscope cover glass. 97
4.6 Numerical-aperture filtered iSCAT using rapid beam scanning. 98

5.1 Calculated distributions of refractive index and specific volume of protein sequences. 108
5.2 Concept of mass photometry. 110
5.3 Characterisation of mass accuracy, precision, and dependence on molecular shape and identity. 114
5.4 Shape-dependence, noise and resolution characterisation. . . . 116
5.5 Single-molecule mass analysis of heterogeneous protein assembly. 121
5.6 Solution vs surface mass distributions. 124
5.7 Imaging mass photometry 128

List of Abbreviations

BFP	Back focal plane
BSA	bovine serum albumin
CMOS	complementary metal oxide semiconductor
CSR	complete spatial randomness
DoG	difference of Gaussians
FFT	fast Fourier transform
FWHM	full width at half maximum
GNP	gold nanoparticle
iSCAT	interferometric Scattering Microscopy
LoG	Laplacian of Gaussian
MSP	membrane scaffold protein
NND	nearest neighbour distance
PP	particle probability
PSF	point spread function
QE	quantum efficiency
SLB	supported lipid bilayer
SNR	signal-to-noise ratio
SPT	single particle tracking
STD	standard deviation
ThT	thioflavin T

Chapter 1

Introduction

Purely optical detection of single molecules was first achieved 30 years ago, initially with the measurement of light absorption by a single molecule at low temperatures,[1] followed shortly thereafter by the detection of fluorescence from a single molecule, also at low temperature.[2] Since then, the field of single-molecule optics has expanded rapidly, with room temperature, solution-phase detection of single molecule fluorescence now routine, finding particular application in the life sciences. Leaving aside force-based single molecule techniques such as optical tweezers,[3] magnetic tweezers[4] and atomic force microscopy,[5] single-molecule optics has been dominated by fluorescence-based detection. The red shift of the emitted light with respect to the excitation light enables efficient background rejection with optical filters, while genetically encodable fluorescent proteins facilitate the labelling of recombinant proteins for single molecule studies.[6] In addition, the blinking and switching behaviour of fluorescent molecules[7] has enabled the development of super-resolution microscopy that circumvents the diffraction limit through either deterministic[8] or stochastic[9,10] switching of molecules between fluorescent and non-fluorescent states.

Single molecule fluorescence is not without its limitations, however. Not least among these is the requirement for labelling of the protein of interest,

since most molecules are non-fluorescent. In addition, the limited photon flux imposes restrictions on the achievable signal to noise ratio in an image for a given time resolution. In combination with rising interest in the ability to optically interrogate nanoparticles, these factors have provided an impetus for the development of alternative highly sensitive imaging techniques based on other contrast mechanisms.

Among the various ensuing developments are those based on light scattering. Experiments based on the tracking of gold nanoparticles as scattering labels at the plasma membrane of a cell demonstrated enormous improvements in temporal resolution compared to tracking of fluorescent labels,[11,12] and imaging of 40 nm gold nanoparticles with nanometre precision and sub-millisecond temporal resolution is now readily possible with certain dark field microscopes.[13] Pushing beyond this, interference-based techniques such as interferometric scattering microscopy (iSCAT) would seem to hold particular promise for highly sensitive imaging of very small objects. Indeed, the utility of iSCAT in this regard has been demonstrated with the localisation and tracking of 20 nm gold nanoparticles at high spatiotemporal precision,[14,15] imaging of unlabelled biomolecular assemblies,[16–18] and even the detection and tracking of single unlabelled protein molecules.[19,20]

In this work we describe recent technical developments in iSCAT for improved detection sensitivity, and the resulting application of such microscopes to weighing large biomolecular complexes through quantification of their scattering contrast, an approach we have named mass photometry. We characterise this new application of iSCAT, illustrate its potential usefulness with measurements on a couple of heterogeneous systems, and discuss areas for future development to broaden the capabilities of this approach.

In chapter 2 we provide an overview of the development of iSCAT as an

ultrasensitive extinction-based imaging method within the historical context of other interference-based imaging modalities. In addition, we review recent applications that make use of this sensitivity, in particular for single-particle tracking and label-free imaging even down to the single (macro)molecule level.

Chapter 3 recaps the fundamentals of light scattering, and details the instrument used for the acquisition of (most of) the data presented in the rest of this thesis. It then describes in detail the image processing and data analysis methods developed for the quantitative imaging of single protein molecules under two different scenarios. We discuss a few considerations and observations relating to the acquisition and analysis of mass photometry data, and consider the current limitations in terms of mass resolution, precision and sensitivity, with a view towards possible improvements.

Chapter 4 introduces the concept of numerical aperture filtering for facilitating quantitative single molecule imaging by circumventing current hardware limitations. This includes details on the experimental implementation, and simple illustrations for both weak scatterers and larger (here, meaning extending beyond the diffraction limit) objects.

We further explore the implications of these capabilities in chapter 5, introducing the concept of mass photometry. We provide a justification for the use of scattering contrast as a proxy for molecular mass, and characterise the current capabilities of an iSCAT microscope as a mass measurement device. We apply these capabilities to the highly heterogeneous Env/BanLec system, and illustrate the utility of the spatially resolved nature of this technique with measurements of α-synuclein aggregation on supported lipid bilayers.

Finally, in chapter 6 we provide a brief summary of the contents of this thesis and an outlook towards future directions for mass photometry.

Chapter 2

Interferometric Scattering Microscopy: Background and Overview

This chapter has been adapted from the following publication: G. Young and P. Kukura, Interferometric Scattering Microscopy, *Annual Review of Physical Chemistry*, 70, 301-322 (2019).[21] Republished with permission of Annual Reviews; permission conveyed through Copyright Clearance Center, Inc.

2.1 Introduction

The primary objective of microscopy is to apply the fundamental laws of physics to visualise structure and dynamics on small length scales. Our perception of the meaning of the word small in the context of what can be imaged has evolved dramatically since Hooke's observation of individual cells 350 years ago,[22] all the way to clear images of individual atoms.[23] The use of visible light to image the species of interest has and continues to be important in the context of the life sciences, owing to its comparatively noninvasive nature and three-dimensional imaging capability. Frustratingly, however, light microscopy has until relatively recently been restricted to modest gains in resolution

and sensitivity, largely limited by the achievable numerical aperture and the resulting mismatch between the area to which light can be confined and the size of even relatively large molecules (Figure 2.1a).

Being able to 'see small' ultimately comes down to addressing three challenges: resolution, specificity and sensitivity. Here, we focus on imaging sensitivity, which is determined by a combination of two factors: the ability to detect a weak signal and the ability to distinguish that signal from any background. The most intuitive way to achieve the latter involves removing all other objects, i.e. trapping in a vacuum, which led to the first observation of individual ions.[24] It took almost another decade until similar sensitivity levels were reported in the condensed phase, using absorption as a contrast mechanism in combination with a sophisticated double-modulation approach at cryogenic temperatures.[1] Soon thereafter, the same molecular system was investigated using fluorescence detection as in the original ion work, demonstrating significantly enhanced signal-to-noise ratios (SNRs) compared to the absorption case but with a considerably simpler experimental setup.[2] The difference in achievable SNRs between the two experiments is representative of the ease with which one can remove background signatures arising from the bulk.

2.1.1 Scattering and Absorption as a Contrast Mechanism

The challenge in moving away from fluorescence towards the more universal extinction as a contrast mechanism rests on our ability to reject background signatures that overpower the signal of interest. In fluorescence detection, the ability to suppress illumination light by more than six orders of magnitude using optical filters while detecting at a different wavelength with essentially no losses generates a vacuum-equivalent scenario in an optical sense. The object

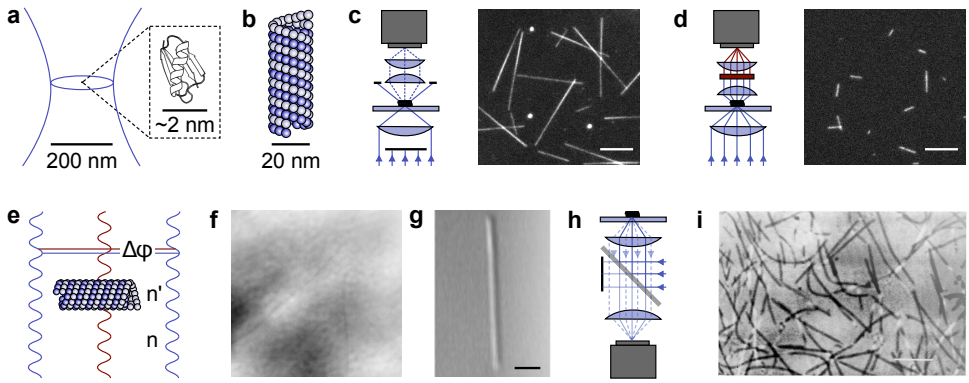


Figure 2.1: Sensitivity limits of light microscopy illustrated with tubulin and microtubules. (a) Illustration of the size mismatch between the diffraction-limited area of visible light focused with a high numerical aperture objective and that of the tubulin dimer. (b) Simplified microtubule structure. (c) Schematic of a typical dark-field microscope and example image of individual microtubules acquired using such a microscope. Scale bar: 5 μm. (d) Schematic of a fluorescence microscope operating in transmission mode and an example image of fluorescently labelled microtubule seeds. Scale bar: 5 μm. (e) Schematic of interference-based optical detection of a nano-object. (f) Phase contrast image of microtubules. Image size: 30 μm. (g) Differential interference contrast image of a single microtubule. Scale bar: 2 μm. (h) Schematic of reflection-based interference microscopy. (i) Image of individual microtubules taken on a laser-scanning confocal microscope in reflection mode. Scale bar: 4 μm. Panel f adapted from reference 25 with permission. Panel i adapted from reference 26 with permission. The dark field and fluorescence images in panels (c) and (d) were kindly provided by Anne Straube.

becomes completely isolated from other optical signals, as long as none of the surrounding molecules and optics fluoresce at the detection wavelength. It is therefore not surprising that fluorescence detection has been the dominant mechanism for single-molecule optics since its inception and has become a routine approach through the directed improvement of associated detectors and optics.

Efficiently separating illumination and detection, however, does not necessarily require a difference in wavelength between the two processes. Using the simple concept of orthogonal illumination and detection pathways, Siedentopf and Zsigmondy[27] recorded optical signatures from nanometre-sized gold colloids as early as 1903 using what they called an 'ultramicroscope'. The general concept of removing excitation light while detecting scattered light

has become known as dark-field microscopy, which has traditionally been the gold-standard for ultrasensitive light microscopy beyond fluorescence. As an example, dark-field observation of individual microtubules (Figure 2.1b,c) can produce images of near-identical quality to those achievable with fluorescence staining (Figure 2.1d).[28] Given the similarity of these images in terms of their contrast, the immediate question arises as to why dark-field microscopy cannot detect single molecules if fluorescence can. While factors such as labelling density affect the fluorescence contrast to some degree, the key difference is how the signal magnitude scales with the number of molecules present.

Assuming for simplicity that every tubulin dimer is fluorescently labelled, and given that the structure of microtubules implies the presence of of approximately 300 dimers per diffraction-limited spot, we would accordingly expect the signal to drop 300-fold in fluorescence detection when comparing the signal from a microtubule and a single tubulin dimer. By contrast, the dark-field scattering signal scales with the square of the object volume, which this case is roughly equivalent to the square of the number of proteins, amounting to a signal drop of $\sim 10^5$. Ultimately, this dramatic signal scaling with object size makes the detection of single molecules in pure scattering so challenging. The problem is not that scattering or extinction signals become intrinsically too small to detect, as we know from the observation of single atoms in vacuum,[29] but because it becomes increasingly difficult to detect these signals in the presence of background light caused by the sample or imperfections in the optics. Even if the background were constant (and could be measured independently of the signal of interest, e.g. if the molecules of interest are moving) and could be subtracted, the measurement would have to be performed with extremely high dynamic range to visualise and quantify the tiny single-molecule signal over the dominant background.

2.1.2 Interference-based Microscopy

The drastic drop in scattering signal with particle volume can be partially addressed by employing an interferometric detection scheme, since the interferometric signal scales linearly with object size compared with a square-dependence for pure scattering.[30] Here, the object is detected as a consequence of interference between background light and light phase-shifted by interaction with the object (Figure 2.1e). That such an approach may indeed be worth pursuing in the context of visualising small objects was already confirmed by the first report on single-molecule detection,[1] which was enabled by modulating the interference between light interacting with the molecule and background light. Taken together, interference thus seems to be well-suited for ultrasensitive optical microscopy down to the single-molecule level, with the continuing caveat of sufficient background suppression.

Perhaps the first microscope to explicitly make use of interference as a contrast mechanism was the phase contrast microscope conceived in 1935 by Zernike,[31] which introduces a phase shift to the transmitted light in a conventional microscope to increase the contrast of transparent objects. This was followed in the 1950s by differential interference contrast microscopy,[32,33] where the interference takes place between a pair of slightly displaced beams to reveal interfaces between regions of different refractive index. A major advantage of both approaches is the use of common path interferometry, where the two interfering light fields travel along almost identical routs, minimising the influence of external perturbations. Nevertheless, the images of microtubules using these contrast mechanisms fail to achieve image quality comparable with that of dark-field microscopy: in phase contrast, microtubules are barely visible owing to illumination, transmission and detection inhomogeneities (Figure 2.1f),[25] whereas differential interference contrast improves the image quality (Figure

1g)[28] but still with inferior SNR compared to dark-field imaging. Although such transmission-based schemes have struggled to reach the extreme sensitivity levels required for single-molecule detection, there have been significant developments using advanced illumination and detection schemes, which are particularly powerful for label-free imaging of cellular structures.[34,35]

Operating interference-based microscopy in reflection rather than transmission is advantageous for the detection of small objects, because the majority of incident light passes the sample unaffected, while only a small portion is reflected (Figure 2.1h). Assuming that light scattering from subdiffraction objects is the same in the forward and backward directions, the combination of weakly reflecting illumination and backscattered light results in enhanced interferometric contrast. It is important to realise that this approach does not improve the ideal SNR of the measurement (assuming a detector capable of detecting as much light as is incident upon it). The contrast simply increases at the expense of the total number of detected photons, resulting in the same SNR for shot-noise-limited detection.[36]

There have been numerous implementations of common path interferometry in reflection for microscopic contrast, taking advantage of different illumination and detection schemes, but they all share the same underlying idea. A transparent substrate supporting the sample is illuminated through the same objective lens as is used for imaging. A small portion of the incident light is reflected at the interface between the glass and the sample, serving as a reference field. The majority of the incident light propagates past the interface and interacts with objects in the sample. The back-reflected light from the interface and some of the light scattered by the sample are collected by the objective lens and used to form an image (Figure 2.1h). The detected intensity,

I_{det}, at a given point in the image is then given by

$$I_{det} = I_{inc}[r^2 + |s|^2 + 2r|s|cos\phi] \tag{2.1}$$

where I_{inc} is the incident intensity, r^2 is the reflectivity of the glass-water interface, s is the scattering amplitude of the particle in the sample and ϕ is the phase difference between the reflected and scattered fields. From Mie theory, the scattering amplitude by a small spherical particle can be written as

$$s = \eta\epsilon_m\pi\frac{D^3}{2}\frac{\epsilon_p - \epsilon_m}{\epsilon_p + 2\epsilon_m} \tag{2.2}$$

where $\epsilon_{m/p}$ are the dielectric functions of the surrounding medium/particle respectively, D is the diameter of the spherical particles, and η is a constant factor accounting for the detection efficiency of the setup.[30] Here the origin of the intensity scaling for pure versus interferometric detection discussed above becomes immediately clear: whereas the pure scattering terms, $|s|^2$, scales with the square of the volume of the scattering object, the interferometric term scales linearly, causing a much slower signal drop with decreasing object size. Indeed, for weak scatterers such that $r \gg |s|$, the pure scattering term, $|s|^2$ in Equation 2.1 becomes negligible, and the interferometric contrast, defined as the normalised difference in signal in the presence of a particle compared to the absence, becomes

$$C = \frac{I_{part}}{I_{bgd}} - 1 = \frac{2|s|}{r}cos\phi \tag{2.3}$$

where $I_{part/bgd}$ is the detected intensity in the presence/absence of a particle, respectively. It is this interferometric contribution that is of particular interest for ultrasensitive imaging.

Initially, it was the phase change caused by an optical path difference between the two fields that attracted most interest. When implemented in a reflection geometry, this results in a signal that is highly sensitive to the axial

separation between a glass coverslip surface and objects in the sample, and so used to measure cellular adhesion in a method termed interference reflection microscopy (or IRM).[37] Developments in the experimental implementation, primarily the introduction of the antiflex method to reduce stray reflections from optical components,[38] and in the theoretical framework of the technique[39] followed, though the inherent optical complexity of the biological cell limited interpretation of the images obtained to a mostly qualitative nature.[40] Subsequent work was thus aimed at better-defined model systems, enabling quantitative measurements on colloidal particles, giant unilamellar vesicles and lipid bilayers,[41,42] with the technique by that point known as reflection interference contrast microscopy (or RICM).

2.1.3 Ultrasensitive Extinction Microscopy

While the improved scaling of the interferometric scattering signal versus that of pure scattering assists in the detection of weakly scattering objects, the associated signals still decrease linearly with volume, making very small objects such as single molecules difficult to detect. Under ideal experimental conditions, the only noise source would be the shot noise associated with counting photons. Were one to realise such ideal detection, the use of lasers as an illumination source could be advantageous due to the high incident power densities of monochromatic light that they enable, although bringing additional difficulties associated with coherent illumination, such as a risk of increased speckle corrupting the image.

The first explicit example of imaging subdiffraction objects in a reflected light microscope using laser illumination made use of a laser-scanning confocal microscope that was equipped with a beam splitter, rather than the more conventional dichroic mirror used in fluorescence imaging, to study microtubule

dynamics (Figure 2.1i).[26] Although performing a quantitative comparison is difficult, it is clear that the interferometric contrast is enhanced compared with differential interference contrast and the SNR is at least qualitatively comparable with dark-field imaging. Given that apparently little optimisation of the equipment was done for the detection modality apart from the minor modification of the beam splitter, single-molecule detection sensitivity does not seem completely impossible. Nevertheless, interest in this approach to interferometric detection essentially vanished with the influx of genetically encodable fluorescent proteins[6] and the immense promise of fluorescent imaging for cellular and single-molecule imaging. Interest in fluorescence-free imaging of nanoparticles only reemerged alongside the advent of nanoscience and when the fundamental limitations associated with fluorescence-based methodologies were encountered.

A step change in detection sensitivity was achieved by an absorption-mediated modulation approach called photothermal microscopy, enabling the observation of 5-nm gold particles.[43] Here, background suppression was achieved by basing the contrast mechanism on a phase shift induced by local heating of the sample, and ensuring that the local heating was exclusively due to light absorption by the nanoparticle of interest. Subsequently, Lindfors et al.[44] demonstrated detection and spectroscopic investigation of gold nanoparticles (GNPs) as small as 5 nm in diameter for interferometric imaging in reflection with a supercontinuum laser source. Reverting to the illumination scheme used by Amos and Amos in reference 26 allowed for more rapid monochromatic imaging of nonmetallic objects such as microtubules[45] and viruses,[46] as well as an implementation of wide-field imaging.[45]

2.1.4 Interferometric Scattering microscopy

The term interferometric scattering microscopy (iSCAT) was coined in the context of a study reporting on the diffusional dynamics of individual viruses on supported lipid bilayers.[16] While technologically similar to the work of Amos and Amos in reference 26 in recording the interference of scattered and back-reflected laser light from a sample with an inverted microscope, it introduced a few concepts that have since been crucial to the evolution of the technology. Principal among these is the in hindsight trivial realisation that for shot-noise-limited detection the SNR of an interferometric signal, S, scales as $S \times N^{1/2}$, where N is the total number of detected photons. Given that N for a given exposure time is directly proportional to the illumination intensity, the SNR could therefore in principle be improved indefinitely by simply detecting more photons, either by increasing the laser power or the exposure time. The underlying challenge, therefore, is to maintain shot-noise-limited imaging performance. This was addressed in two ways, which have been and continue to remain central to all iSCAT experiments since: (a) wide-field detection with speckle-free illumination to eliminate image noise caused by laser-based fluctuations that make shot-noise-limited detection impossible, and (b) efficient (digital) background subtraction, in particular of residual substrate signature, spurious reflections and illumination inhomogeneities, which otherwise dominate the image.

The result of this evolution is a light microscope capable of - at least in principle - detecting and localising any changes in local optical properties relative to the surrounding medium (see Eq 2). Here, we will review recent demonstrations of these capabilities, firstly looking at high-speed and/or highly precise single-particle tracking (SPT) of GNPs as the area of application that has thus far received most attention (Section 2.2), before considering the

direct (i.e. unlabelled) imaging of biological nano-objects made of lipids or peptides and their (dis)assembly dynamics (Section 2.3), the limit of which is the label-free detection of single protein molecules (Section 2.4).

2.2 Single-Particle Tracking

SPT interrogates the motion of single molecules or larger assemblies at a level of detail inaccessible to ensemble techniques.[47] In its fluorescence-based implementation, the object of interest is typically labelled with a dye molecule, fluorescent protein or semiconductor quantum dot. The optical image of a subdiffraction species returns the point spread function (PSF) of the microscope centred on the location of the object. Although the width of the PSF is typically on the order of 200 nm for visible light and a high numerical aperture objective lens, finding the centre of mass of the PSF, for example by fitting a model PSF such as a two-dimensional Gaussian function, returns the position of the emitter with a precision much higher than the resolution of the microscope. The achievable precision in the absence of noise sources other than shot noise can be approximated as $\sigma/N^{1/2}$, where σ is the standard deviation of the Gaussian and N is the number of detected photons.[48] In this way, localisation precision on the order of a few nanometres is achievable for $N > 10^4$.[49]

The key advantage of fluorescence-based SPT is its compatibility with live-cell imaging because of its powerful background rejection capability and the possibility of using molecular-sized dye labels or genetically encodable fluorescent proteins.[6] Photoblinking and bleaching, however, limit the total observation time and can produce gaps in the acquired trajectories, resulting in poor statistics. More fundamentally, however, optical saturation caps the maximum achievable photon flux from single emitters. Combined with the dependence of localisation precision on photon count mentioned above, this

results in a rule of thumb that the achievable spatiotemporal precision is on the order of 1 nm/Hz$^{1/2}$. Although these limitations can be addressed by reducing the observation duration per trajectory[50,51] or using advanced illumination approaches,[52] the majority of single-emitter-based studies exhibit comparable performance characteristics.[49,53–57]

These limitations are absent for iSCAT, as for all scattering-based approaches, because scattering labels do not bleach or blink, nor do they saturate regardless of illumination power. If the SNR $\propto S \times N^{1/2}$, as enabled by background subtraction and shot-noise-limited detection, then one can maintain a given localisation precision irrespective of exposure time, which determines the time resolution, by proportionally increasing the incident light intensity. As a result, within the limits set by photodamage, one can achieve essentially arbitrary combinations of localisation precision and time resolution for high speed (Section 2.2.1) and high-precision (Section 2.2.2) SPT. This comes at the cost of requirement for larger labels, usually on the order of 20 nm diameter GNPs in vitro, and 40 nm diameter or larger for cellular studies (Section 2.2.3). At the same time, however, label-free imaging of biological nanoparticles can be performed directly, obviating the need for labelling altogether (Section 2.3).

2.2.1 High-Speed Single Particle Tracking

The capabilities of iSCAT for SPT are well introduced by recent experiments on the processivity of myosin 5, a molecular motor that has been studied in much detail at the single-molecule level over the past decades.[58] Using single-molecule fluorescence, it has been shown to walk in a hand-over-hand fashion along actin, taking 74 nm steps (Figure 2.2a) and consuming one ATP molecule per step.[49,59,60] As a consequence of the limitations in spatial precision and temporal resolution achievable with fluorescence imaging, these experiments

could provide information on the motor only while bound to the underlying actin filament, leaving much of the stepping mechanism in the dark. Using iSCAT imaging of 20 nm gold labels attached to one of the motor domains revealed detailed signatures of a previously reported intermediate state[61] persistently to one side of the actin filament (Figure 2.2b). This transient state exhibited kinetics associated with ATP hydrolysis, which is required before the moving head can rebind to actin to complete the step, suggesting that it is a signature of the step being taken. In combination with a series of control experiments, this finding led to a model for the efficiency of myosin 5 processivity based on a restricted relative motion between the two heads of the protein.[15] The clear observation and characterisation of this state was enabled by the simultaneous nanometre spatial precision and millisecond temporal resolution, which are highly beneficial for mechanistic studies of motor proteins.[62,63]

While these imaging speeds are sufficient to reveal many new details of motor protein motility, where the relevant timescales are determined by the mechanochemical cycle of the protein, following processes such as diffusion in lipid bilayers requires much higher time resolution.[11] The absence of saturation in the scattering signal also allows access to these temporal regimes with iSCAT, enabling not only detection[45] but also nanometre-precise tracking with submillisecond exposure times.[14,36,64] Frame rates have even approached 1 MHz with an appropriately fast camera.[65] Accessing these temporal and spatial domains with SPT is significant because, for example, it allows for the observation of transient events which would otherwise go unnoticed, such as heterogeneity of diffusion in ternary lipid bilayers over length scales <20 nm on microsecond timescales.[66]

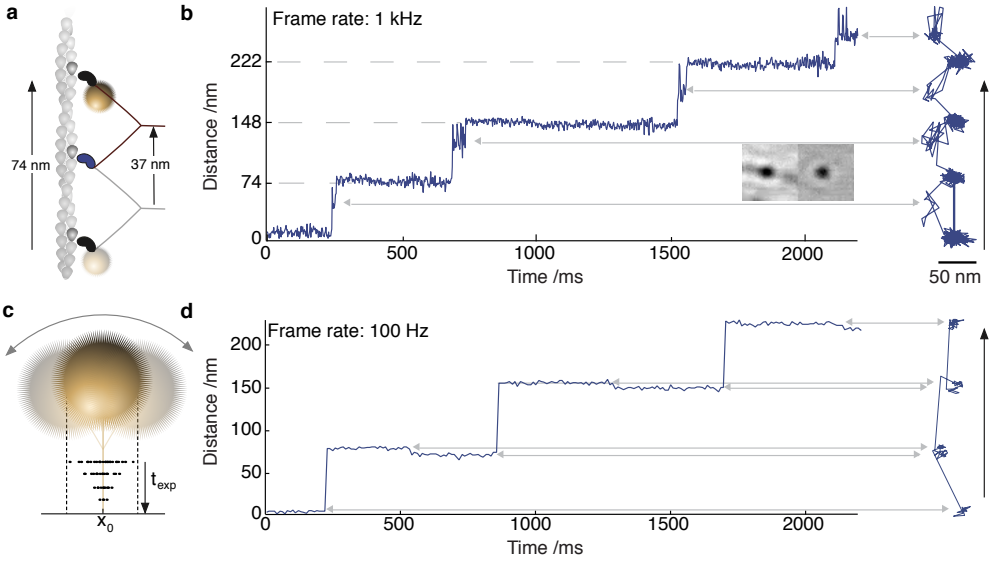


Figure 2.2: Tracking of molecular motors with gold nanoparticle labelling with high spatial precision and temporal resolution. (a) Schematic of a gold-labelled myosin 5 motor stepping along an actin filament. (b) Distance-time trace and accompanying XY trajectory of a myosin 5 molecule stepping along actin, imaged at 1 kHz. The transient state when the motor takes a step is localised to one side of the actin filament. (Inset) Image of a 20-nm gold nanoparticle label before and after background subtraction. (c) Schematic of the concept of temporal averaging to improve localisation precision, through averaging the motion of the scattering label. (d) Distance-time trace and accompanying XY trajectory of a myosin 5 molecule stepping along actin, after frame averaging to 100 Hz. A small transition can be observed while the labelled head is bound to actin. Figure adapted from reference 15.

2.2.2 High Precision Single-Particle Tracking

Aiming for ever higher temporal resolutions with label sizes on the order of several tens of nanometres, however, contains a potential pitfall: one begins to observe not only the motion of the object to which the label is attached, but also the motion of the label itself.[64] As a result, even if the nominal localisation precision is high at very low exposure times, trajectories become blurred by the motion of the particle about its attachment point, which is superimposed onto the motion of the object of interest. Moving in the opposite direction of longer integration times, for example by temporal averaging of frames, effectively eliminates this effect because the label motion averages out and very high SNRs

are enabled through large total numbers of detected photons per exposure, thus allowing very high localisation precision (Figure 2.2c). One therefore has either to accept slightly lower than theoretically achievable localisation precision[15] or to sacrifice some temporal resolution for spatial precision.[67]

As an example, in the case of myosin 5, reducing the imaging speed from 1 kHz to 100 Hz improved the localisation precision to 1.6 nm. As a result, the traditional distance vs time traces now exhibited not only the expected 74 nm step of the labelled head but also an additional, much smaller, apparent backwards motion of the label coinciding with stepping of the unlabelled head (Figure 2.2d). The key outcome here is the ability to maintain few-nanometre localisation precision even at speeds almost 100-fold higher than achievable with single-molecule fluorescence for prolonged imaging, thereby accumulating sufficient statistics to clearly visualise the previously hidden transition. An additional salient point is that the concept of repeated measurement can be reused to improve precision with respect to the localisation of the bound states, with subnanometre precision possible in principle.

2.2.3 Tracking Molecules on Cells

High-performance SPT, in addition to detecting sufficient photons, rests on the ability to estimate and remove the background, not just from the optical setup but also, and more challengingly, from scattering within the sample. The samples considered so far are reconstituted systems where the sample-specific background can be well controlled. More highly scattering environments such as living cells, however, prove to be more of a challenge, although such measurements are possible provided that the background varies much more slowly than the motion of the particle of interest. As an example, it has proven possible to track 40 nm GNP-labelled membrane proteins with 3 nm localisation preci-

sion at 40 kHz on thin regions of U2OS cells and the axons of neuronal cells (Figure 2.3a-c).[68] In agreement with the arguments outlined above concerning the balance between temporal resolution and achievable localisation precision as a consequence of label motion, temporal averaging to 2 kHz frame rate revealed signatures of compartmentalised diffusion. The resulting periodicity on the order of 200 nm (Figure 2.3d) matched the periodicity of actin-spectrin rings previously reported in axons,[69] suggesting that subcellular structures nontrivially affect the mobility of membrane proteins. Furthermore, the interferometric nature of iSCAT enabled the observation of three-dimensional motion of the molecule on the circumference of the tube-like axon structure (Figure 2.3e). More recently, SPT on living cells was demonstrated with μs temporal resolution and nm spatial precision in three dimensions.[70]

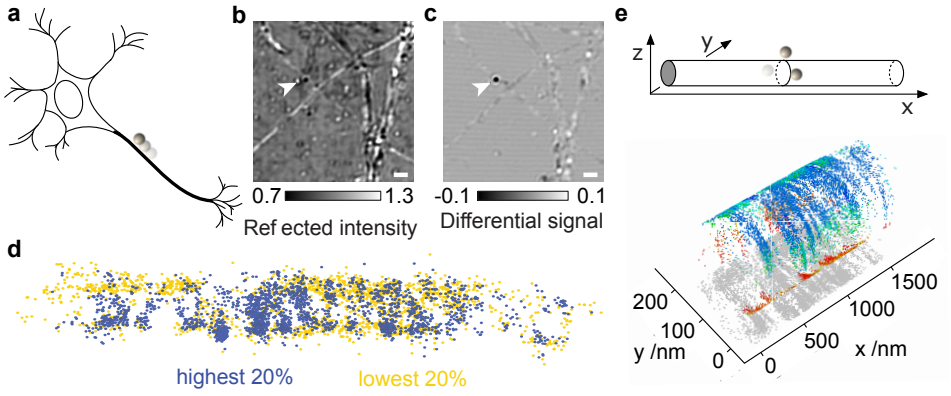


Figure 2.3: iSCAT tracking on cells. (a) Schematic of gold nanoparticle (GNP) tracking on an axon of a neuronal cell. (b) Raw iSCAT image of a 40-nm GNP-labelled membrane protein on a neuronal cell. The white arrow marks a GNP. Scale bar: 2 μ. (c) Background-subtracted image of a 40-nm GNP-labelled membrane protein on a neuronal cell; a yellow arrow marks the GNP. Scale bar: 2 μm. (d) Selected localisations from a 2 kHz trajectory of 40-nm GNP-labelled glycosylphosphatidylinositol-green fluorescent protein on an axon. The 20% of all localisations exhibiting the highest confinement are shown in blue, whereas the 20% exhibiting the lowest confinement are shown in yellow. (e) Schematic of a three-dimensional reconstruction from the geometry of the neurite and example three-dimensional trajectory. Figure adapted from reference 68.

An alternative approach to reducing scattering background from the cell involves performing the measurement in transmission, because it avoids col-

lecting reflections from the combination of nearby glass-water and cell-water interfaces.[71,72] While the tracked objects in recent reports were comparatively large (>200 nm virus particles and vesicles), there is clear opportunity for future improvements in sensitivity. In addition, more sophisticated background estimation methods may further extend the applicability of iSCAT-based SPT, as exemplified in recent work that estimates the background in cases where the particle of interest moves by less than the size of the diffraction-limited PSF.[73]

2.3 Label-Free Imaging of Nanoscopic Assembly

The fact that the interferometric contrast relies on a difference in optical properties of the object compared to its surroundings implies that iSCAT can be viewed more generally as a highly sensitive refractive index microscope in the sense that any nanoscopic changes in optical properties can in principle be detected and quantified. To illustrate this, consider the hypothetical (dis)assembly of a nanoscopic structure, such as a GNP, on a glass substrate in solution (Figure 2.4a). In the absence of the particle, we would expect no scattering signal from the diffraction-limited volume, because the optical properties of said volume are indistinguishable from the surrounding bulk. This situation changes upon assembly of the GNP, because the local optical properties have now changed, as the local concentration of gold atoms has increased dramatically within the diffraction-limited volume. Of course, this is applicable not simply to GNPs. Rather, it is clear from Eq 2.2 that any object with a refractive index different from that of the surrounding medium will scatter light, providing a route to high SNR visualisation of assemblies of biological materials such as proteins and lipids, without the need for labelling

As a result, iSCAT can be used to monitor not only the motion of objects

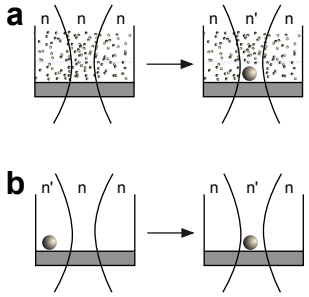


Figure 2.4: Label-free imaging of nanoscopic (dis)assembly. (a) Schematic of nanoparticle assembly, leading to a local refractive index change that can be visualised in iSCAT. (b) Schematic of nanoparticle motion as a local refractive index modulation.

with high spatiotemporal resolution but also changes to their structure such as their formation or disassembly. In fact, even SPT can be regarded as a special form of the more general concept of local changes in optical properties (Figure 2.4b), just with different underlying dynamics in that the object moves, rather than forming, disappearing or binding/unbinding.

As an aside, a highly simplified but potentially very useful way to think about iSCAT imaging is to completely abandon the concepts of extinction and interference and think about changes in surface reflectivity. According to the Fresnel equations, the reflectivity of an interface for normal incidence is given by $R = |\frac{n_1-n_2}{n_1+n_2}|^2$, where n_1 and n_2 are the refractive indices of the two bulk materials forming the interface. In the absence of an object at the interface, $n_1 = n_{glass}$ and $n_2 = n_{H_2O}$, but in its presence $n_2 \neq n_{H_2O}$, causing a local change in reflectivity which can then be detected and imaged. Although these considerations ignore the subtleties at play, they distil the problem to a very simple scenario: iSCAT microscopy, just like interference reflection microscopy or reflection interference contrast microscopy, is a tool that images the reflectivity of an interface. The higher the sensitivity, the smaller the local change in refractive index that can be measured.

2.3.1 Label-Free Tracking

Noting that the contrast of an individual microtubule in iSCAT is rather similar to that of a 20 nm diameter GNP,[45] one would expect similar levels of spatiotemporal precision to be achievable. Indeed, under essentially identical imaging conditions as in reference 15, the centre of mass of individual microtubules (Figure 2.5a) could be determined with a localisation precision of 1.4 nm at 1 kHz, improving to 0.4 nm at 100 Hz (Figure 2.5b).[18] This is sufficient to distinguish not only the 8 nm steps characteristic of a microtubule bound to a single kinesin motor, but also smaller steps of 4 nm and 2 nm at higher motor densities. In addition to following the centre of mass, the length of microtubules could also be followed with a precision of 1 nm at 100 Hz (Figure 2.4c), which, in combination with the lack of photobleaching, meant that the shrinkage of microtubules upon washout of taxol could be followed with high spatiotemporal precision over long timescales. Given that most individual proteins (especially those of molecular mass greater than 20 kDa or so) are of diameter >2 nm,[74] these results illustrate that in principle it should be possible to monitor the assembly dynamics of large biological complexes at the single-molecule level in a universally applicable way.

2.3.2 Lipid Assemblies and Their Dynamics

A well-studied but difficult to visualise example of nanoscopic dynamics is the formation of supported lipid bilayers by the vesicle fusion method, which involves the transition of a lipid bilayer from a nanoscopic sphere to a supported sheet (Figure 2.6a). Given that the optical properties of a lipid bilayer are different to those of glass or water, iSCAT can be used to visualise individual vesicles bound to microscope cover glass directly, with a signal that increases with average particle diameter (Figure 2.6b).[17] Importantly, however, rupture

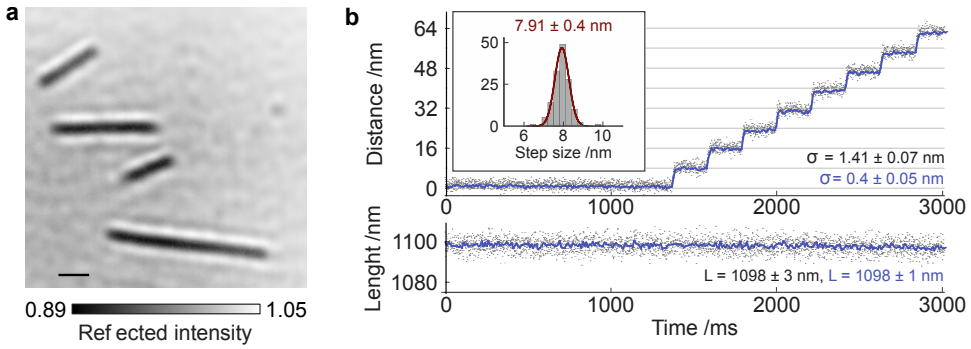


Figure 2.5: Label-free single-particle tracking. (a) iSCAT image of individual microtubules bound to microscope cover glass. Scale bar: 0.5 μm. (b) Tracking of artificial 8 nm steps performed by moving the sample of microtubules bound to cover glass with a nanometric stage (top) and accompanying measurement of the length of the microtubule as it is translated (bottom): Grey dots represent localisation acquired at 1 kHz frame rate and the blue line represents localisation after averaging to 100 Hz. Figure adapted from reference 18.

of the vesicles on the glass surface to form a planar bilayer causes a change in the amount of material present in a diffraction-limited spot because of the difference in surface area of a sphere compared with that of a disc. As a result, iSCAT can monitor not only the adsorption of single vesicles to a glass substrate, which is the first step in the formation of supported lipid bilayers, but also their rupture, which is the critical next event (Figure 2.6c). Combining these observations with changes to vesicle size and substrate properties enables direct observation and characterisation of supported lipid bilayer formation, revealing the interplay between factors such as critical concentration of surface-bound vesicles and the surface-substrate interaction strength.

The concept of imaging changes in local refractive index can also be applied to dynamics within the membrane, such as local phase separation. Such processes have traditionally been visualised using fluorescence imaging with dye molecules that preferentially compartmentalise into one of the different membrane phases.[76–78] Phase separation often involves differences in lipid order and membrane thickness, with associated differences in the local reflectivity that can be imaged with iSCAT. As a result, the appearance and growth of lipid

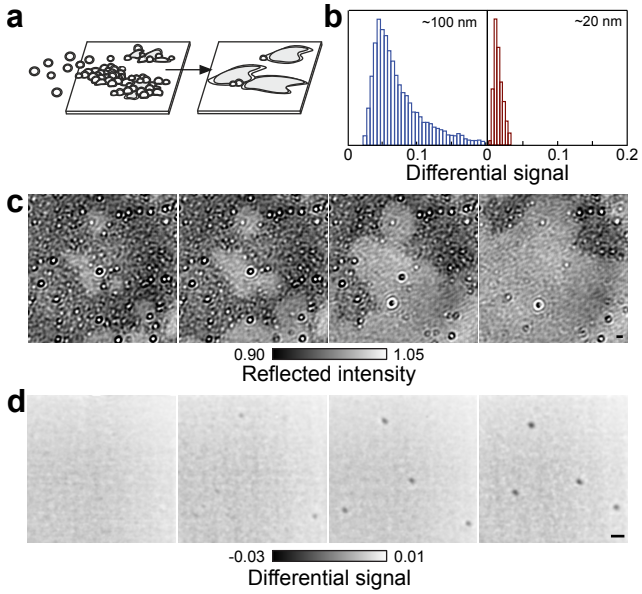


Figure 2.6: Label-free imaging of lipid assemblies. (a) Schematic of the transition from vesicles adsorbing to a glass surface, to a supported lipid bilayer. (b) Histograms of iSCAT contrasts of 100 nm extruded unilamellar vesicles (left) and 20 nm sonicated unilamellar vesicles (right). (c)Sequence of iSCAT images showing the transition from adsorbed sonicated unilamellar vesicles to a supported lipid bilayer on a glass surface. Images are separated by 200 ms intervals. Scale bar: 1 μm. (d)Sequence of iSCAT images separated by 1 s showing the appearance of lipid nanodomains upon cooling of a three-component droplet interface bilayer below the transition temperature. Scale bar: 1 μm. Panels a-c adapted from reference 17. Panel d adapted from reference 75.

nanodomains upon cooling a bilayer near a phase boundary could be monitored directly with iSCAT in the first dynamic observation of such structures (Figure 2.6d).[75] The dependence of the iSCAT signal on domain size and the ability to quantify simultaneously the mobility of the domains enabled characterisation of domains of size down to a 50 nm radius. The same concept could also be applied to more complex cholesterol-containing bilayers, which are more closely representative of cellular membranes.

2.3.3 Virus Particle Dynamics

A virus containing its packaged DNA possesses a different scattering cross section, and therefore different iSCAT contrast, than does an empty viral

capsid.[46,79] As a result, it is possible to quantitatively probe the dynamics of DNA ejection by immobilised bacteriophages upon interaction with the receptor protein LamB.[80] By following the intensity of the iSCAT signal from individual phages as a function of time, the kinetics of material loss can be quantified with higher time resolution than possible with previous single-particle studies, an important consideration for a process that occurs on the sub-10 s timescale,[81] with a measurement uncertainty equivalent to 4.2 kbp per frame. This corresponds to monitoring the DNA content of individual phages to within 10% of the total content. Aside from DNA release, the same approach is also applicable to the direct monitoring of single virus particle assembly.[82] Here, rather than quantifying DNA release, the label-free imaging sensitivity of iSCAT is used to visualise the increase in local protein concentration associated with capsid assembly.

2.4 Label-Free Single-Molecule Imaging

With respect to the possibility of detecting and imaging individual proteins, considering microtubules once again proves informative. iSCAT images of individual microtubules bound to a microscope cover glass (Figure 2.4a) provide a signal-to-background ratio on the order of 10, suggesting a detection limit of approximately 30 tubulin dimers. The fact that the background is constant and can be accurately quantified, however, suggests that the achievable sensitivity of iSCAT is much better than 30 proteins, assuming that this background can be either removed or subtracted, in the spirit of fluorescence detection or the original ion-detection work. This speckle-like background has been persistent in all iSCAT studies and is likely caused by imperfections on and near the surface of the microscope cover glass.

It is therefore unsurprising that the first reports of fluorescence-free single-molecule detection at room temperature, which emerged almost simultaneously, used a combination of sophisticated noise and background suppression methodologies to extract the desired single-molecule signal. The experimentally simplest approaches removed background signatures by immersing the molecule in an index-matched matrix and eliminating laser-based intensity fluctuations with a balanced detection scheme. The result was sensitivity below parts per million in what was effectively the single-molecule version of a simple absorption spectrometer, revealing clear signatures of single absorbers.[83,84] Detection of single molecules was also reported with a photothermal approach[85] similar to the original GNP work[43] that capitalised on the excellent background suppression and high specificity of photothermal microscopy (although it was necessary to use glycerol to achieve a high change in refractive index with temperature). A third approach made use of ground-state depletion to selectively image the absorption of single dye molecules.[86]

These achievements were transformative in that they shattered the notion that room-temperature single-molecule detection was feasible only using fluorescence as a contrast mechanism. All of these approaches, however, relied either on the presence of a strong resonant electric dipole transition (as in single-molecule fluorescence imaging) or on quenchers. As a result, they only slightly broadened the scope of single-molecule imaging, because all continued to require that the molecule of interest possesses a resonant response at the illumination wavelength to generate sufficient imaging contrast. Enabling the full promise of label-free single-molecule detection, especially in the biological context of single proteins, required a different approach.

2.4.1 Nonresonant Single-Protein Detection and Imaging

The other route to visualising single molecules involves quantifying the background precisely and comparing images with and without the molecule of interest. This approach is no different to the operation of essentially any sensor, which compares a readout in the presence and absence of the analyte. For an optimised iSCAT experiment, this requires efficient suppression of noise sources such as sample drift or illumination noise. Under these conditions, it is irrelevant that the single-molecule signal is much smaller than the background, because the background can be removed by subtraction of images.

To illustrate this approach, consider the label-free detection, imaging and tracking of single proteins, illustrated by myosin 5 molecules walking along actin.[20] A raw iSCAT image exhibits the now familiar speckle-like background from the microscope cover-glass substrate as well as faint elongated features that can be attributed to single actin filaments (Figure 2.7a). The assignment to single filaments is robust assuming linear scaling of the iSCAT signal with particle volume: given that individual SV40 virus-like particles of mass 15 MDa produce an iSCAT signal of 4.5%, we would expect single actin filaments, which contain about 75 actin subunits (with a total mass of 3.1 MDa) per diffraction-limited spot, to exhibit an iSCAT signal on the order of 0.9%, in excellent agreement with the experimental observation. On the basis of these considerations, we can also calculate the expected signal (0.15%) from individual motor molecules (502 kDa). Taken together, these findings immediately make clear that individual motors cannot be observed statically because their signal is smaller than that of actin filaments, which themselves are only visible with a signal-to-background ratio of $\sim$3.

To visualise single proteins, therefore, the two approaches described above

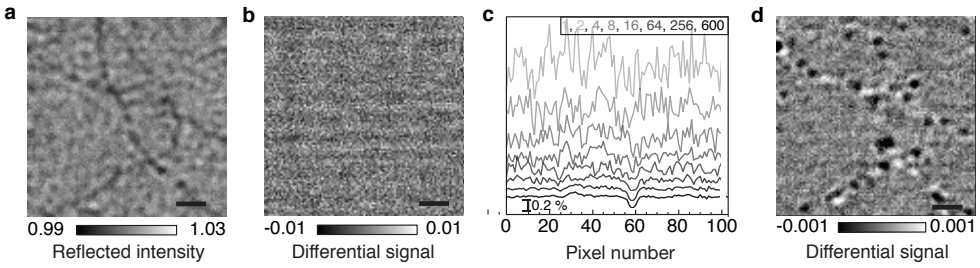


Figure 2.7: Nonresonant label-free imaging of single biomolecules. (a) Raw iSCAT image of actin filaments on a microscope cover glass in the presence of myosin 5a. (b) Differential image obtained by subtracting the temporal median image of a stack from the raw image in panel a. (c) Line cuts across averaged differential images, illustrating the reduction in shot-noiseinduced background fluctuations as a function of the number of frames averaged, enabling the observation of a signal from an individual myosin 5a molecule. (d) Differential image of individual myosin 5a molecules obtained by averaging 170 consecutive differential frames. Scale bars: 1 μm. Figure adapted from reference 20.

are combined. Firstly, the static background is subtracted from each image in the stack of images containing mobile features. This background is estimated by taking the temporal median down the image stack, such that highly mobile features do not appear in this median frame (Figure 2.7b). Secondly, (background-subtracted) images are averaged to reduce shot-noise-induced fluctuations to a level below the signal of individual motors (Figure 2.7c). The result is images revealing mobile, diffraction-limited features colocalised with the filaments and of contrast 0.18±0.06%, as expected for individual motors (Figure 2.7d). These results, in combination with the expected processivities, step sizes and velocities, confirm that iSCAT is capable of detecting and imaging individual proteins. Demonstrating detection of proteins down to 66 kDa, a related study used rapid binding to a coverslip surface (an approach referred to as a 'landing assay' throughout the rest of this thesis), rather than motion across objects attached to it, as a means to identify and subtract background features, and further illustrated that the iSCAT signal magnitude scales roughly linearly with molecular mass.[19]

2.5 Conclusion

Ultrasensitive optical microscopy has undergone dramatic changes over the past three decades, with broad implications for imaging biological structure and dynamics as well as for bioanalytics. The dominance of fluorescence-based approaches, in particular for in vitro studies, has recently been challenged by a variety of extinction-based methods. As always, such a drastic change of contrast mechanism is accompanied by both advantages and disadvantages, which have to be considered carefully when deciding which approach to use to address the question of interest. Nevertheless, there is now clear evidence that iSCAT can provide uniquely detailed information in two areas: (a) SPT with up to microsecond time resolution and subnanometre spatial precision when labels of 20 nm diameter or larger are acceptable, and (b) label-free imaging of nanoscale (dis)assembly with high spatiotemporal precision, as well as being able to directly image objects as small as single protein molecules under aqueous conditions and at room temperature. It is this final capability that we shall primarily consider in the following chapters, with a particular focus on improving the extent to which quantitative information can be extracted from such single molecule measurements.

Chapter 3

Experimental Methods, Data Analysis, Observations and Limitations of Mass Photometry

This chapter will discuss the basics of light scattering, focusing on small particles. We will then describe the iSCAT instrument used for the collection of most of the data in this thesis and the standard experimental procedure used for acquisition of mass photometry data. There will then be a detailed description of the analysis routine we developed for mass photometry in order to go from raw iSCAT images of a glass surface to a contrast distribution of weakly scattering particles binding to that surface, as was used for the data presented in the following two chapters. In addition, we describe a different analysis routine for extracting the contrasts of particles moving laterally across the surface, with potential applications for label-free single particle tracking illustrated with the example of proteins moving on a supported lipid bilayer (SLB). Following this there will be a discussion of considerations of and observations on the acquisition and analysis of data that have appeared to be important for the measurement of high quality distributions. Finally, there will follow a discussion of the current limitations of mass photometry as an analytical method, with a particular focus on mass resolution, precision and sensitivity, together with possible routes to improve on each.

3.0.1 Contributions

The iSCAT movies of dynamin diffusing on SLBs were acquired and kindly provided by Manish Kushwah. Max Hantke developed and implemented in Python the model PSF described as the difference of two smoothed jinc functions and used for PSF fitting in the mobile particle analysis.

3.1 Light scattering

When light passes through an object or medium, the intensity of light detected at the other side of the object/medium is less than the incident intensity. This attenuation is, in general, the result of both scattering of light away from the propagation axis of the incident ray and the absorption of light by objects, with this combined effect known as extinction. The detected intensity of light (at a particular wavelength) passing through such a medium is described by the Beer-Lambert law

$$I = I_0 \exp(-k_e L) \tag{3.1}$$

where I_0 is the incident intensity at that wavelength, L is the thickness of the medium, and $K_e = k_a + k_s$ is the extinction coefficient, which itself is the sum of the scattering and absorption coefficients. Each of these $k_{a/s}$ is related to the sum over all absorbing/scattering objects and their respective absorption/scattering cross sections.

As we have alluded to previously, part of the appeal of iSCAT as a microscopy technique is the universality of scattering, meaning that a signal from any refractive index inhomogeneity can be detected regardless of whether it has a resonant transition to absorb light, and indeed the work presented in the rest of this thesis is exclusively concerned with objects that do not absorb at

the visible wavelengths used. We will therefore consider only scattering from here on. We will also focus primarily on scattering by small particles, since the overarching theme of this work is the detection and quantification of single protein molecules. Light scattering is an effect derived from the polarisability of the scattering object. Charged particles in the object (generally, the electrons) are driven into motion by the oscillating electric field vector of the incident light, and this acceleration of charge causes light to be radiated at the frequency of oscillation.

The intensity and angular distribution of light scattering is governed principally by 3 parameters: the wavelength, λ of the incident radiation; the optical properties of the particle relative to the surrounding medium, governed by the complex refractive index, $m = n + ik$ (although fundamentally coming down to the polarisability of the particle); and the size of the particle, typically expressed as the dimensionless size parameter, x.

$$x = \frac{2\pi r}{\lambda} \tag{3.2}$$

In the limit of small particles ($x \ll 1$, or typically of size $< \lambda/10$), the electrons in the scattering object are all driven into oscillation by the electric field of the incident light essentially in phase with each other, and so the object (typically a molecule) can be considered a point dipole oscillating at the same frequency as the incident light. Such an oscillating dipole will radiate light at that oscillating frequency, resulting overall in a scattering of incident light away from the propagation axis. This is the essence of the small size approximation under which Rayleigh scattering is valid.

The simplest case to consider is that of a single radiating dipole. In the context of scattering, this is the result of polarised light incident upon a small scatterer such that the induced dipole oscillates along the well-defined

polarisation axis. A cut through the emission pattern of such a dipole is shown in Figure 3.1a, with the pattern shown being cylindrically symmetric about the dipole axis (so that in three dimensions the corresponding surface resembles a torus shape). The scattered intensity, I, is described by

$$I \propto I_0 k^4 \alpha^2 \sin^2 \theta \tag{3.3}$$

where I_0 is the incident intensity, k is the wavevector of the incident light, α is the polarisability of the particle (in general a tensor, though here assumed to be isotropic for such small particles) and θ is angle from the dipole axis. For the results presented in this work, given the use of polarised laser light and the imaging capabilities of a microscope giving access to single molecule signatures, it is this case that is actually the most relevant for the rest of this thesis, although, as discussed in the next chapter, this emission pattern is somewhat modified by the presence of a refractive index interface. We will nevertheless continue with our brief overview of light scattering in general, for the purposes of putting this into context.

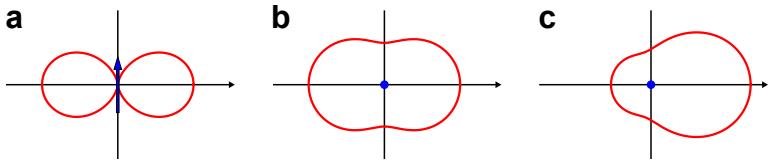


Figure 3.1: Scattering patterns by small particles in an isotropic environment as a function of angle. In all cases the black arrow denotes the propagation of light. (a) Emission pattern of a point dipole (Rayleigh approximation for linearly polarised light). The blue arrow denotes the dipole orientation. No light is scattered along the dipole axis, and the cylindrical symmetry means there is no dependence on azimuthal angle (in the plane perpendicular to that of the dipole). (b) Intensity of Rayleigh scattering of unpolarised light. Since the light is unpolarised, the pattern is cylindrically symmetric about the axis of propagation of light. (c) Mie scattering of unpolarised light by a particle of size parameter $x = 1$. Note the increase in the proportion of forward scattered light. In (b, c) the blue dot marks the position of the scattering object.

The standard result derived by Rayleigh,[87] and that appearing in most

textbooks, e.g. with relevance to atmospheric scattering, is for the case of unpolarised incident light such as sunlight. There, since the light is unpolarised, the orientation of the induced dipole varies at random over all angles in the plane perpendicular to the propagation axis of the incident light, and the the resulting (time-averaged) scattering pattern is essentially an incoherent rotational average of all such dipole emission patterns. This results in a pattern as shown in Figure 3.1b, where now the axis of cylindrical symmetry is that of the propagation of the light, with an intensity, I, described by

$$I \propto I_0 k^4 \alpha^2 (1 + \cos^2 \Theta) \tag{3.4}$$

where here Θ is the angle between the propagation axis of the light (i.e. $\Theta = 0$ corresponds to forward scattering).

There are a few important features to note here, common to both the polarised and unpolarised case. Firstly, and somewhat trivially, the scattered intensity is proportional to the incident intensity. This is perhaps not particularly interesting when considering scattering in isolation, but in the context of single-molecule microscopy and the inevitable comparison with single molecule fluorescence, this is in contrast to the optical saturation to which a fluorescence signal is subject.

Secondly, the dependence on wavelength, expressed here through the wavevector $k = 2\pi/\lambda$. This strong wavelength-dependence, λ^{-4}, means that blue light is scattered much more strongly than red light, with light of $\lambda = 400$ nm scattered almost 10 times as strongly as that with wavelength $\lambda = 700$ nm. To give the commonly referred to example, this is the reason why the sky is blue and sunsets are red - looking overhead during the daytime one sees principally light scattered by molecules and small particles in the atmosphere, which is largely blue because a higher proportion of the incident intensity at

blue wavelengths are scattered compared to longer wavelengths, while when observing a sunset one is looking at small angles from the propagation of the light and so sees mostly the redder components that have been less strongly scattered.

Thirdly, the dependence on the polarisability of the object, arising since the induced dipole moment (which is the immediate source of the scattered radiation) is given by $\mathbf{p} = \alpha \mathbf{E_{inc}}$, where $\mathbf{E_{inc}}$ is the incident electric field vector. A more polarisable object is one in which the induced dipole formed by electrons being displaced by the action of the electric field of the incident light is larger for a given incident light intensity. When observing at a given angle, wavelength of light and illumination intensity, objects of different polarisability will result in different scattering intensity and therefore be, in principle, distinguishable on this basis. This is the essence of the idea that protein molecules of different mass may be distinguished based on their scattering contrast, subject to the condition that, for such biomolecules made of the same few amino acids, protein molecular weight can be used as a rough proxy for polarisability. This will be discussed in more detail in Chapter 5.

As particle size increases, at any given time different parts of the object 'see' the incident light wave at different phases, and so the induced dipoles across the object have phase differences between them. It is no longer sufficient to consider the entire object as a point dipole, therefore, and the resulting far-field scattering pattern is the result of interference between all the 'wavelets' emitted by the induced dipoles at different locations (and therefore different phases) across the object. This problem is, in general, rather complex, with the scattering pattern depending on particle size and shape. For scattering by spherical particles, a set of solutions to Maxwell's equations were provided by Gustav Mie,[88] giving rise to the description of scattering by such intermediate-

sized particles ($x \sim 1$) as Mie scattering. The amount of scattering still increases with particle size, but there are now a couple of key differences. Firstly, the proportion of light that is forward scattered becomes much larger. This is illustrated in Figure 3.1c, which shows the angular distribution of light scattered by a particle of size parameter $x = 1$. This was calculated using the software MiePlot[89] for a wavelength of 525 nm, such that the radius of the particle was taken to be $r = 83.6$ nm (in order for $x = 1$). As particles get larger still, lobes in the angular distribution start to appear.

The second main difference compared to Rayleigh scattering is a much weaker wavelength dependence, such that wavelengths across the visible range are scattered with fairly uniform intensity. Continuing with the atmospheric examples, this is the reason why fog, which typically consists of water droplets on the order of several microns, appears white.

The final scattering regime arises as the objects become larger still, $x \gg 1$, that is, where the wavelength of the light is negligible compared to the size of the object. In this case, the light paths are well-predicted (and relatively simply predicted) using the rules of geometric optics and ray tracing. That is, reflection and refraction of light rays at the interfaces of the object and the surrounding medium are sufficient to explain the behaviour. Since such objects are of a size larger than the field of view of the iSCAT microscopes used in this work, we will not consider this any further.

3.2 iSCAT microscopy

The construction of a general iSCAT microscope capable of, for example, achieving the results surveyed in the previous chapter has been well described in detail previously.[90] Here we will give an overview of the particular setup used for the acquisition of most of the data in this thesis, including a consideration

of the choice of the different components. This is essentially similar to previous descriptions of an iSCAT setup, but with the addition of a partial reflector in the back focal plane (BFP) of the microscope objective (described in detail in Chapter 4), and a few mounting considerations relating to stability that are discussed at the end.

A schematic of the experimental setup is shown in Figure 3.2. Briefly, the collimated output of a laser diode is spatially filtered and passed through a pair of acousto-optic deflectors (AODs). The deflection of the beam by the AODs is imaged by image 4f telecentric lens system into the BFP of the objective. The combination of a polarising beam splitter (PBS) and quarter-wave plate (QWP) separates illumination from detection. Another 4f (this can be the same 4f, if the beam splitter is placed between the AODs and TL1) re-images the BFP of the objective onto a partially reflective mirror consisting of a small-diameter, thin layer of silver deposited onto an anti-reflection coated window. A final lens forms the image on the camera.

The laser used was chosen to be a laser diode sourced from Lasertack, either a 2W 445 nm. Diodes were chosen for their relatively broad emission spectrum (FWHM $\sim$ 1 nm) compared to other, more expensive laser systems (the low price being an additional bonus). The relatively short coherence length ($\sim$ 100 μm) that this implies helps to keep unwanted interferences, arising, for example, from additional back reflections from the lenses inside the objective, relatively low since the optical path differences are beyond the coherence length of the light source. As discussed in the previous section, shorter wavelengths are in general preferable in terms of increasing the amount of light scattered by very small objects, hence the choice of a blue wavelength for illumination.

Generating effectively wide-field illumination by rapid-scanning of a beam that is loosely focused (typically to $\sim$ 1 - 2 μm) at the sample seems to bring

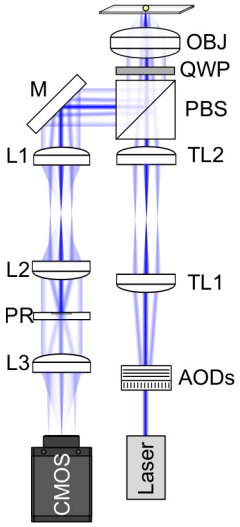


Figure 3.2: Schematic of a typical iSCAT microscope used in this work for mass photometry. Laser used is typically a diode laser. AODs: acousto-optic deflectors. TL1, TL2: 4f telecentric lens system in illumination. L1, L2: 4f telecentric lens system in detection. PBS: polarising beamsplitter. QWP: quarter-waveplate. The combination of PBS and QWP ensures efficient separation between illumination and reflected light. OBJ: high numerical aperture, oil-immersion objective. PR: partial reflector. L3: final imaging lens. CMOS: camera used for detection.

with it the benefit of reducing excessive speckle on the image when compared with conventional wide-field epi-illumination (achieved by focusing a static beam into the back focal plane of the microscope objective). This seems especially true when using such cheap laser diodes as here, which have a tendency to shift wavelength sometimes. This results in a change in the observed speckle pattern that manifests as additional noise in differential images. A reason for this could be the effective loss of spatial coherence on the timescale of the exposure time of the camera, arising from the fact that at any point in time within a single exposure only a part of the image is illuminated by the focused beam, with the resulting image then being an (incoherent) sum over over the exposure time.

We have used high numerical aperture oil-immersion objectives (typically 1.4-1.42) in order to maximise the collection of scattered photons. When measuring what are essentially dipole emitters at the glass-water interface, having an NA at or above 1.4 is particularly helpful. This is because of the

high density of emission radiated in to angles at or above the critical angle, which for water as the measurement medium corresponds to an NA of 1.33, when the emitter is located at or just above the interface. This effect will be discussed in more detail in Chapter 4.

The combination of the PBS and QWP in combination with reflection at the glass-water interface functions as an optical isolator for separating illumination and detection. The illuminating light is linearly polarised such that it is transmitted (or reflected) through the PBS. After passing through the QWP it is circularly polarised, and upon reflection the returning beam is also circularly polarised but with opposite helicity. When this light passes back through the QWP it becomes linearly polarised again but in the perpendicular direction to the incident light. In this way while the incident light is transmitted (reflected) by the PBS the returning light is reflected (transmitted) and so the two paths are separated.

The returning light (reflected and scattered) is re-imaged by a 4f telecentric lens system to form first an intermediate image plane and then an image of the BFP of the microscope objective. The principal purpose of this is to provide direct access to this back focal plane. The placement of additional optics here has been extensively used in the context of single-molecule fluorescence microscopy for point spread function engineering, for example by using a spatial light modulator to introduce programmable phase delays across the back focal plane.[91–93] Here we place a partially reflective mirror to attenuate the light in the centre of the back focal plane relative to that at the outside in order to reduce intensity of reflected light relative to the scattered light and so increase contrast. Further details on and justification for doing this are presented in more detail in the next chapter. Incidentally, placement of an iris diaphragm in the image plane (that is, the plane conjugate to the sample plane, as opposed to

the BFP) also turns out to be helpful in extinguishing extraneous background light (e.g. from back-reflections from optics).

Traditionally one of the main considerations when choosing a camera for iSCAT is the full well capacity of the pixels - that is, how many photoelectrons a pixel can detect before it is saturated. This is alleviated by the use of the partial reflector mentioned above, but it remains true to say that the more photoelectrons can be collected per unit time (and indeed per unit area on the camera chip) the better.

With this in mind, frame rate is also an important consideration not only in determining the achievable time resolution, but also because running faster than necessary and then averaging frames is one way of increasing the amount of light that can be collected. For this reason, CMOS sensors are typically preferred to CCD sensors, since they typically read out faster as each pixel has its own readout architecture, while the pixels on a CCD chip are read out by passing through a single readout register. The downside of this readout method is that each pixel has a different readout noise and gain to all the others.

The readout properties of particular pixels can be quantified by illuminating the camera chip (or the portion of the chip that is being read out) with a light source that is constant in time at various illumination levels from completely dark up to saturation.[94] Acquiring several images at each illumination level enables one to take the mean signal (in analog-to-digital units, ADU) and variance of each pixel as a function of amount of light incident upon the pixel. Taking the standard deviation of the values when no light is incident on the pixel provides the readout noise. At sufficiently high illumination that the shot noise on the detected photons is much greater than the readout noise, a plot of variance against mean signal will be linear, with the slope corresponding to the gain in electrons per ADU (e-/ADU). This was checked for the sensor used

in this work (Sony Pregius IMX174), taking a 256x256 pixel region of the chip (65,536 pixels in total) and calculating the gain and readout noise for each one. Both turned out to be quite tightly distributed: the mean gain was 8.50±0.07 e-/ADU (mean±standard deviation) with only 3 pixels (about 0.0046% of those checked) having a gain above 9 e-/ADU and none below 8. The readout noise of the same pixels, meanwhile, had a mean value of 6.88±0.18 e-, with only 20 pixels (0.03% of those tested) with read noise greater than 10 e- (and all less than 13 e-). Reassuringly, these values are in good agreement with those specified by the manufacturer. Considering the general aim to reach shot-noise-limited performance, fluctuations of 100 e- (RMS) due to shot noise would put the shot noise at least 10 times higher than the fluctuations in pixel value due to read noise for essentially all pixels. This corresponds to a mean value of 10000 detected photoelectrons, or 30% of the full well capacityy of the camera. It seems reasonable to assume, therefore, that the pixel-to-pixel variation in readout has limited impact on the quantitative image data, when the camera is operated as close to saturation as possible as is always the case for an iSCAT experiment (counts typically at or above half the saturation value of the camera).

Another downside of CMOS sensors as compared to CCDs in the past has been a tendency to have substantially worse readout noise and quantum efficiency (QE). Improvements to CMOS technology in recent years has, however, narrowed or even removed this gap. As we have seen above, the readout noise of the sensors used in this work is, while perhaps not sufficient for high-performance single-molecule fluorescence work, perfectly fine for shot-noise-limited detection when operating under high-light situations as with iSCAT. There do exist other sensors, marketed as scientific CMOS (sCMOS), with readout noise reaching below 2 e- that rival the performance of EMCCDs for single-molecule

fluorescence. With respect to QE, this has also improved to reach ∼70% at green wavelengths for the sensor used in this work (although, again, some sCMOS sensors now reach QEs of >95% for fluorescence work). Looking forward, it seems likely that future developments in CMOS sensor technology and data transfer will result in more sensors better able to efficiently collect more photoeletrons per unit area and time.

Aside from these particulars of the components of the setup, an important consideration to bear in mind throughout construction is stability - in terms both of mechanical stability of each component, and of minimising fluctuations along the beam path. Practical implications of this include maintaining a beam height that is a low as possible to the surface on which the setup is constructed, and keeping the optical path length as short as possible. Mounting the entire setup (including the objective and sample mount) on a single aluminium plate of dimensions 600x400x50 mm^3, and then enclosing with walls of aluminium plate 40 mm thick also proved to be helpful in this regard. In general, enclosure of the beam path always helps. This can mean simply enclosing the entirety of the setup if it is sufficiently small, although if the footprint of the setup becomes too large then additional 'sub-enclosures' such as tubing around the beam path might become necessary.

3.3 Standard Experimental Procedure

While there are many different applications of iSCAT involving a variety of different assays (see the previous chapter for an overview), in this thesis we focus almost exclusively on a simple non-specific binding assay referred to as a 'landing assay' and extracting quantitative information from such an experiment as accurately as possible. To set the rest of this chapter in context, here we provide a general overview of this experimental procedure.

We start by cleaning a microscope coverslip (#1.5 thickness), usually by rinsing sequentially with milliQ water and ethanol or isopropanol, followed by drying under a stream of dry nitrogen. These are then assembled into a flow chamber by fixing a smaller coverslip on top using two pieces of double-sided sticky tape to leave a channel between the two pieces of tape. Alternatively silicone gaskets (Culterewell, Grace Bio-labs) can be placed onto the cleaned coverslip to create open-topped wells to hold aqueous sample.

After placing the coverslip on the microscope, we add buffer to the measurement region (the flow channel or well) and place the sample in focus using the image of the roughness of the coverslip surface. The sample (typically a dilute solution of protein molecules) is then added to the measurement region and a series of images continuously acquired over $1 - 2$ minutes. During this time, most protein molecules will bind non-specifically and irreversibly to the glass surface. This binding allows the measurement of the single-molecule contrast after subtraction of the scattering background from the glass surface (the procedure for which is detailed in the next section), and it is this contrast that we are principally interested in since, as we have alluded to already but shall see in more detail later, it turns out to be a reasonable proxy for the molecule's mass.

3.4 Data Analysis Routine

As mentioned previously, the principal step in revealing the scattering signals from weak scatterers such as single proteins is the digital removal of static background scattering. This has typically taken one of two forms, depending on the temporal behaviour of the object of interest: either an image (or average of images) is taken from a given time and subtracted from subsequent frames, or from the stack of frames containing mobile features the median value of each

pixel through time is calculated and that median image used as the background. The first case can be useful for particles that arrive and then do not necessarily move much compared to the size of the particle in the image (and therefore would contribute signal to the median background approach), but is susceptible to sample drift causing additional features to appear in the image over time. The second case is a little less sensitive to drift, since the same frames to be analysed are used to generate the background image, but relies on the particles of interest moving sufficiently far that no particle signal contributes to the median value.

So far we have referred to image subtraction, which has been the principal operation used for background removal in iSCAT experiments previously. Specifically, because the illumination profile needs to be normalised for in order to quantitatively evaluate the contrast across the field of view, each image is divided by an estimate of the illumination profile to give normalised images of the surface which are used from then on. This estimate can be made either through translating the sample parallel to the optical axis using an XY stage, or digitally by taking only the low spatial frequency/coarse components of the image (making the assumption that all the features of interest are fine, and the coarser features are simply due to illumination inhomogeneities). Many XY stages, however, seem prone to making the sample more susceptible to drift or mechanical instability, potentially introducing additional features into the background-subtracted images, and as such most of the setups used in this work have not included an XY stage. Digital estimation of the illumination profile (e.g. by a median filter as described a little later in the context of removing residual differential features) is prone to errors involving the incorporation of sample details into the estimate, especially when the contrast of the glass can reach as high as 40% (peak-to-peak) with the partial reflector described in

Chapter 4. A simple alternative is simply to divide the raw images. In this way, one simultaneously normalises for the illumination profile while also removing static features. We will thus refer to ratiometric rather than differential images from here. If the intensity in the background frames is I_{bg} and that in the image of interest (e.g. with a particle present) is I_{part}, then the contrast can be defined in the same way

$$C = \frac{I_{part}}{I_{bg}} - 1 = \frac{I_{inc}[r^2 + |s|^2 + 2r|s|\cos\phi]}{I_{inc}r^2} - 1 = \frac{2|s|\cos\phi}{r} \tag{3.5}$$

following from Eq.2.1, under the approximation that $r \gg |s|$.

3.4.1 Analysis of Protein Binding Events

Background Removal

Of the two methods of selecting background images described above, we have used a modification of the first approach for the identification of protein binding events, where single molecules arrive at the glass surface and are then immobilised on the surface. The average of N frames is taken and subtracted from the average of the N subsequent frames in order to reveal the differential signal between these two frame batches. As the second frame bin advances through the stack, one frame at a time, the background frame bin is updated such that it is always taken from the N frames immediately previous to the current frames of interest. That is, for each frame i, the N frames i - N to i - 1 are averaged together, and the N frames i to i + (N - 1) averaged together. Each raw frame is divided by the mean pixel value of each frame, in order to normalise for any laser intensity fluctuations from frame to frame. The ratiometric image is then calculated as the second frame bin (i to i + (N - 1)) divided by the first (i - N to i - 1). In this way, the time delay between the background frames and the frames of interest is as small as possible, and the influence of sample drift on the differential frames minimised. The size

of the frame averaging window, N, is chosen typically as a trade-off between the reduction of shot noise with increased averaging and the loss of temporal resolution which, after some time, begins to introduce additional background features into the image - further discussion on the optimal choice of N follows in Section 3.2.2.

The result of this approach is a series of images containing only those features that change between the two frame bins on top of an otherwise shot-noise-limited background. In an ideal case this would be only protein-binding events, but sometimes additional features such as beam pointing fluctuations or changes in the illumination profile as a result of the focused beam being scanned in a slightly different pattern from one frame to the next. While each of these can be almost entirely suppressed through enclosing the beam path in the case of beam pointing noise and through triggering the scanning pattern sent to the AODs from the start of the camera exposure in the case of scanning noise, there can sometimes be some residual signatures in the ratiometric images. Fortunately, these manifest themselves as slow changes in the image background over relatively long distances in the image, and as such can be quite straightforwardly removed by a filter that differentiates between such coarse features and the finer features corresponding to diffraction-limited spots. The filter used here is a median filter, where a window of a given size is moved pixel-by-pixel across the image. For each position, the median pixel value within the window is calculated and assigned to the pixel in the smoothed image corresponding to the centre pixel of the window. The result is a smoothed image containing only those features large enough to contribute to the local median value of the square window used, and the ratiometric image can be divided by this to give a 'flattened' image. The window size here is chosen such that the number of pixels within it is more than twice the number

of pixels containing signal from a diffraction-limited spot (the largest feature we are interested in) - in practice this corresponds to a square of edge length 15 pixels. An example image exhibiting such background fluctuations as a result of poor triggering of the beam scanning by the AODs to the exposure of the camera is shown in Figure 3.3a, with the estimated background features and corrected image shown in Figures 3.3b and 3.3c, respectively. There remains a slight dip in intensity running down the centre of the corrected image, where there is clearly a feature that in one dimension is smaller than the window size used, meaning it does not completely feature in the background estimate. Note that the residual background fluctuations are rarely as severe as shown in this example.

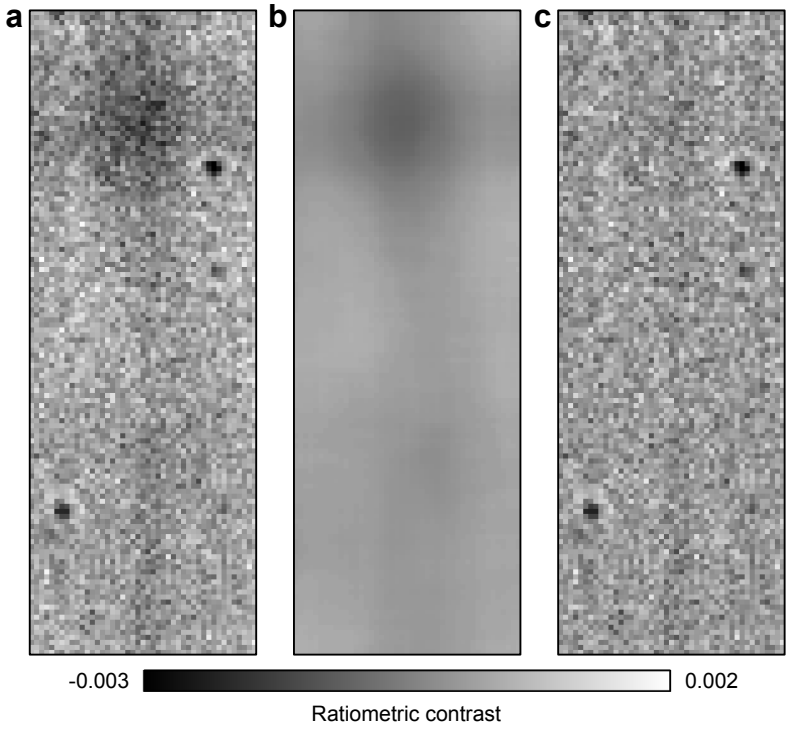


Figure 3.3: Example of median filtering ratiometric images for removal of low spatial frequency features. (a) Ratiometric image showing non-uniform background as a result of poor triggering of the beam scanning pattern to the exposure of the camera. (b) Estimate of the coarse background fluctuations obtained by median filtering (a) with a window size of 15×15 pixels. (c) Resulting corrected image after normalisation of the initial image by the estimated background. Image size = 3.8×10.8 μm^2.

Particle Detection

Having taken care of the large scattering background from the glass surface and residual coarse differential features, attention now turns to the detection of particles in the ratiometric images. This is simplified by the fact that, since all the species of interest are much smaller than the diffraction limit, all binding events appear simply as the point spread function (PSF) of the microscope - i.e. all the same shape, just with different intensity. As such, standard particle detection approaches could be adapted for these images, resulting in a workflow exemplified in Figure 3.4.[95]

Firstly, the convolution of the ratiometric image with the experimentally determined PSF is calculated (Fig 5.2b), to highlight regions of the image that contain similar features to the microscope PSF. Since the point spread function features a central minimum of intensity of FWHM$\sim$3 pixels surrounded by a ring of opposite sign, this kernel can be thought of as similar to smoothed derivative filters such as a Laplacian of Gaussian (LoG) filter. The derivative properties of these filters come from the change of sign across the kernel, which results in the highlighting of features in the image with rapid changes in pixel intensity. Depending on the form of the kernel, this can be used to effectively highlight edges or spots in an image - since here the kernel is radially symmetric, spots are highlighted well. Derivative filters are, however, sensitive to falsely picking up noise as features, a property which is ameliorated by the inclusion of a smoothing component (here essentially matched to the size of the features being looked for by the use of the experimental PSF and therefore a smoothing corresponding to the diffraction limit).[96,97] Since the kernel is negative in the centre, this process inverts the sign of the features, but other than that the contrast is more or less preserved provided the kernel is appropriately normalised.

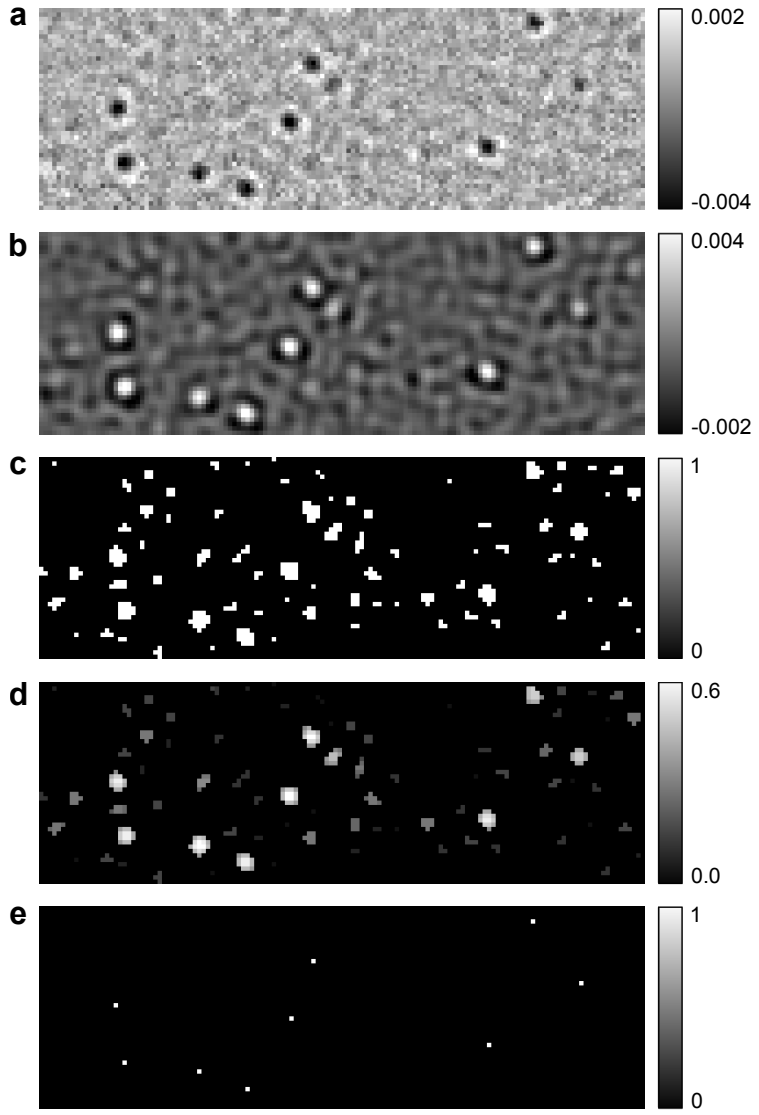


Figure 3.4: Example of the workflow of the particle detection algorithm. (a) Ratiometric image of BSA molecules binding to the glass surface. (b) Result of convolution of the ratiometric image with the experimentally determined PSF (with a kernel size of 7×7 pixels). (c) Binary map of pixels in the convolved image above a contrast value of 0.0008. (d) Particle probability (PP) image calculated from (c) with a window size of 5 pixels. (e) Resulting map of candidate locations using a PP threshold of 0.3 and a local maximum search size of 9 pixels.

The kernel used in this step is extracted from a set of 'landing assays' of a large protein - i.e. one with a high SNR that can therefore be found rather more simply with just a Gaussian smoothing and thresholding approach. In this case, the 396 kDa HSP16.5 24-mer was typically used. Having found all binding events, each event can be extracted from the image stack, overlaid and averaged together to give a measure of the PSF with extremely high SNR. Those events with a near neighbour such that the presence of another particle influences the background of the particle of interest are excluded from this averaging step. The central 7×7 pixel region of this average PSF is taken as the kernel for particle detection, with a scaling factor applied such that image contrast is approximately conserved.

A user-set threshold is applied to this convolved image, resulting in a binary map of pixels with values greater than this threshold (Figure 3.4c; the threshold used in this example is 0.0008, and is fairly typical for the detection of small particles). Here, particles can be thought of as being regions of the image with clusters of pixels exceeding the threshold - i.e. with a value of 1 in this map. From here, a particle probability (PP) image can be calculated as described by Yang et al.[98] Briefly, for each pixel a square window of a given size (here always 5x5 pixels) centred on that pixel is considered. If the centre pixel is 0 in the threshold map, then that pixel is assigned a PP value of 0. If the centre pixel is 1, then a counting procedure is undertaken, whereby the pixels orthogonally adjacent to the centre pixel are considered next, and for each pixel with a value of 1, the 'counter' is incremented by one. From each of these pixels, the next round of counting then begins, again considering those pixels that are orthogonally adjacent to pixels with a value of 1 that have already been considered. This procedure continues until either a 0 or the edge of the window is reached. The PP value then assigned to that pixel is the counter

value divided by the total number of pixels in the window (i.e. 25 here). In this way the PP reflects the proportion of pixels within the window with a value of 1 in the threshold map that form an orthogonally contiguous cluster covering the centre pixel (Figure 3.4d).

A PP threshold can then be set above which pixels are considered as candidate particles for fitting, with a value of 0.3 being typical and used for the example here. Since larger particles will result in more than one pixel above this threshold, and very large particles may even have pixels in the next outer dark ring of the PSF that exceed this threshold, it is important to thin these values so as to only take a single location for each particle (Figure 3.4e). This is done by checking that the value of the corresponding pixel location in the (smoothed) ratiometric image also corresponds to the locally extreme value (i.e. maximum or minimum) within a given window size (here 9x9 pixels) so as to only take the pixel at the centre of the PSF. Checking against the most extreme value rather than the minimum value is needed to reject any positive results from the first dark ring of the PSF, since the window of 9x9 pixels will include parts of the first bright ring (i.e. one ring closer to the centre of the PSF), which is always brighter than first dark ring is dark.

Particle Fitting

We then cut out a region of interest (ROI), typically of 11x11 pixels, centred on each candidate pixel, and fit these ROIs to a model PSF. The size of this window was chosen so as to fully capture the PSF (both the central peak and the first bright ring, the features that are modelled as drescribed below), while not including too many pixels without measurable signal (Figure 3.5a). For the work described here, the PSF was modelled as a difference of two 2D Gaussian functions (DoG function), where the relative widths and amplitudes of the two are fixed by the ratio of the diameter of the partial reflector to the

diameter of the back focal plane of the objective, and by the transmission of the mask. In single molecule fluorescence microscopy, the PSF of a microscope equipped with a high NA objective is commonly approximated by a 2D Gaussian function,[48,49,54] with little loss of accuracy compared to more detailed PSF models such as an Airy disk.[99,100] This Gaussian approximation has also been applied to fitting the signals from weak scatterers in iSCAT images, including 20 nm gold nanoparticles,[15] virus-like particles,[16] and single molecules.[20] Such a Gaussian function therefore seems reasonable as an approximation to the PSF resulting from an imaging system where the Fourier plane (back focal plane of the objective) is bounded by the hard circular aperture of the edge of the objective lens (the low-pass filtering effect of this finite aperture can be thought of as the reason for the diffraction-limited PSF width in the context of Fourier optics). With the introduction of the partial reflector, the back focal plane now looks like a hard low-pass filter arising from the finite size of the objective, plus a high-pass filter arising from the circular stop in the centre of the aperture used to exclude most of the reference field. Given the linearity of Fourier transforms and the Gaussian approximation for the single low-pass aperture in a normal microscope, it therefore seems reasonable to take the difference between a Gaussian PSF resulting simply from the effect of the finite objective aperture and a broader Gaussian resulting from the narrower (in Fourier space) partial reflector. The width of this second Gaussian, σ_2, can be constrained by knowledge of diameters of the partial reflector, d_{pr}, and the objective back aperture, d_{obj}, to give

$$\sigma_2 = \frac{d_{obj}}{d_{pr}}\sigma_1 \tag{3.6}$$

where σ_1 is the width (standard deviation) of the other Gaussian. Similarly, the amplitude of the second Gaussian, A_2, can be related to that of the first,

A_1, through

$$A_2 = \frac{d_{pr}}{d_{obj}}(1-T)A_1 \tag{3.7}$$

where T is the transmission of the partial reflector. In this way, the first bright ring about the dark central minimum, apparent in most single molecule iSCAT images taken with a partial reflector in the back focal plane can, be modelled without the introduction of any additional free parameters in the PSF model, with the specific model used being

$$f(x,y) = A(e^{-[\frac{(x-x_0)^2}{2\sigma_x^2}+\frac{(y-y_0)^2}{2\sigma_y^2}]} - \frac{1-T}{s}e^{-[\frac{(x-x_0)^2}{2(s\sigma_x)^2}+\frac{(y-y_0)^2}{2(s\sigma_y)^2}]} + b \tag{3.8}$$

where $s = \frac{d_{obj}}{d_{pr}} = \frac{8.52}{3.5}$ for the setups used in this work. The peak value of this function, which is the number reported as contrast throughout, is therefore $A(1-\frac{1-T}{s})$. The background offset parameter, b, allows any residual background in the ratiometric images to be accounted for in the fit without influencing the measured contrast, although the stability of the setups and the image processing described above generally render this unnecessary. The standard deviations of the function in x and y are allowed to be independent to account for any residual astigmatism in the iSCAT PSF resulting from the slight misalignment of the setups which is often necessary to reduce spurious back-reflections. This also allows the eccentricity of the particle to be quantified as the ratio of the smaller to the larger of the two fitted standard deviations. Fits are rejected as probably not arising from a 'good' particle if this measure is less than 0.7 or if the fit fails to converge.

Although this PSF model has proved useful, it is clear that it does not fully capture the extended ringing of the PSF (side lobes) that are apparent for larger particles, and indeed are more pronounced for interferometric imaging than for fluorescence microscopy. This mismatch has typically not been a problem for relatively low SNR measurements where these outer lobes are

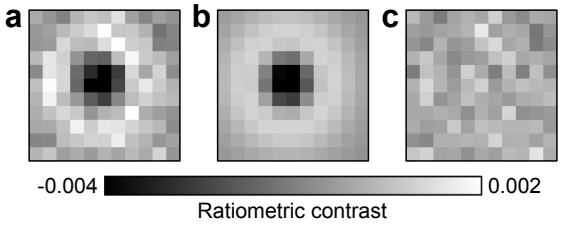


Figure 3.5: Example of fitting the difference-of-Gaussians model PSF to images of single molecule binding events. (a) Representative image of a single BSA monomer binding to the surface. (b) The corresponding fit to the model PSF described in the text. (c) Difference between the data (a) and fit (b), showing no substantial systematic deviation between data and model for this SNR. Image size = 11×11 pixels^2 = 774×774 nm^2.

not so pronounced (Figure 3.5b, c), but could rear its head when trying to measure both very small (<60 kDa) and large (>600 kDa) proteins within the same sample, with the peak contrast of the smaller particles being of a similar intensity to the first dark ring of the larger particles. More accurate PSF models that capture the behaviour of interferometric imaging without a partial reflector have been applied, in particular with the use the square root of an Airy disk.[73] Applying similar arguments as made above for justifying the use of a difference of two Gaussians, a difference of two such jinc functions could result in a greatly improved model of the point spread function of these microscopes.

The process described so far finds and fits every detected particle in each ratiometric frame. However, the sliding ratiometric filter described at the beginning of this section means that each single molecule binding event appears as a particle in several frames, with a different contrast in each frame. For a binding event that occurs within a given frame, when that frame is the last frame of the second frame bin, the ratiometric image will contain a weak contribution from that event. As the sliding filter progresses one frame at a time, the particle is present in increasingly more frames within the second bin, increasing in contrast until the first frame of the second bin coincides (to

the nearest frame) with the frame in which the binding event occurs. As the filter then moves past the binding event, the scattering signal from the particle also appears in some of the frames in the background frame bin, resulting in a reduction in contrast until the centre of the filter is N frames beyond the binding event, at which point the particle simply contributes to the static background and is removed from the image (Figure 3.6a, b). Specifically, we approximate the time-dependence of the ratiometric contrast by

$$C(t) = C_0 \begin{cases} 1 + \frac{t-\tau}{N}, & \text{if } \tau - N < t \leqslant \tau \\ 1 + \frac{\tau-t}{N}, & \text{if } \tau < t \leqslant \tau + N \\ 0, & \text{otherwise} \end{cases} \tag{3.9}$$

where C_0 is the true contrast of the protein, N the frame bin size, and τ the time at which the binding event occurs. The upper term (where $\tau - N < t \leqslant \tau$) is exact, while the second term (where $\tau < t \leqslant \tau + N$) is an approximation in the limit that $C_0 \ll 1$. Note that with the sliding ratiometric filter as described here, unless the binding event occurs precisely between the end of one frame's exposure time and the beginning of the next, no single image will show the full contrast of the protein, as there will always be at least one frame within one of the two bins where the protein is not present for at least part of the exposure of that frame. In order to extract the true contrast, therefore, it is important to fit the temporal profile of the contrast of each particle within the ratiometric movie to Equation 5.4 to find C_0.

These individual results from the fitting of every spot detected in each frame must therefore be classified into groups of data arising from the same particle, based on their spatial and temporal location. Specifically, points that lie within 1 pixel (i.e. 70 nm) of each other and arising from frames within a window size of twice the temporal frame averaging (i.e. $2N$) are classified as one particle. Isolated time points within a group (such as might arise when a small particle gives rise to only a few frames with detectable signal, but a

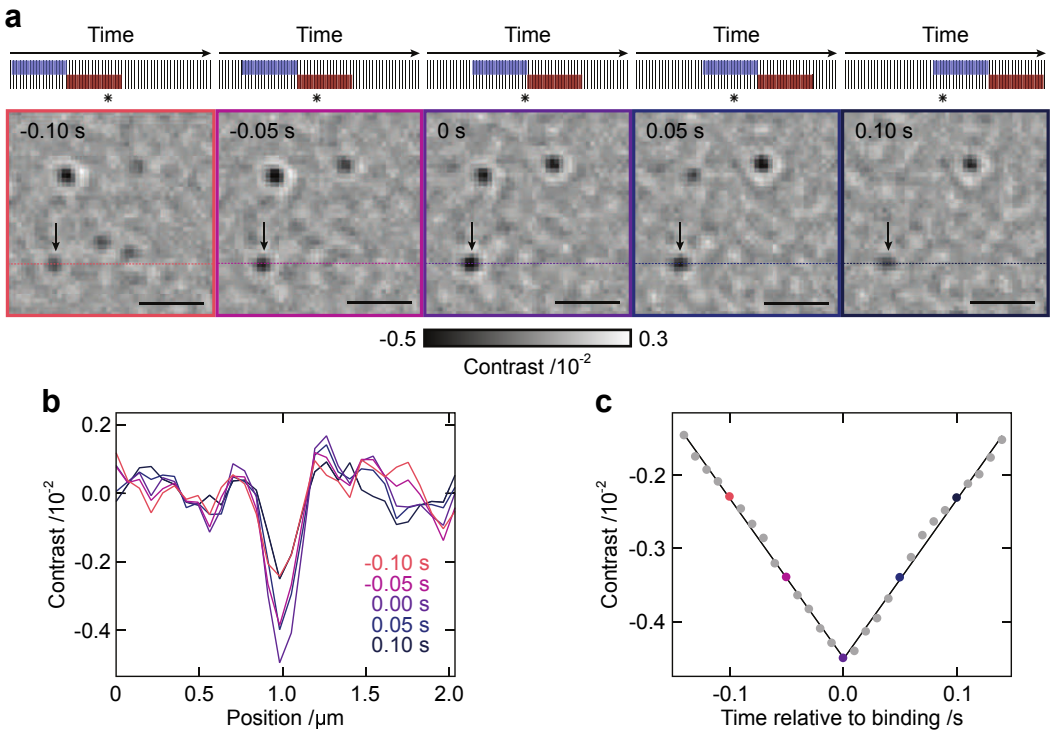


Figure 3.6: Time-dependence of a protein binding signal subject to the sliding background ratiometric processing. (a) Illustration of the image averaging and ratiometric imaging approach. The asterisk marks a landing event. Individual images are averaged into two consecutive blocks (blue and red), which are normalised and divided to provide differential contrast. The mid-point is scanned in time, meaning that the signal from stochastic landing events grows and fades, as indicated by the black arrow. Scale bars: 1 μm. (b) Corresponding cross-sections for the particle highlighted in (a). (c) Corresponding signal magnitudes extracted by a fit to the PSF and fit (black). Adapted from Young et. al.[101] Reprinted with permission from AAAS.

spurious fit disconnected in time but still within the $2N$ window is classified as the same group) are removed based on their separation (in time) from the nearest other data point within the group. Only those groups with at least 5 data points after this procedure are taken, and are fit to Equation 5.4 to give the peak contrast, C_0, and the binding time, τ, (with, in principle, sub-frame precision) for each individual particle (Figure 3.6c). Particles are additionally filtered by rejection if the fit fails to converge or if the determined binding time is at or beyond the first or last data point in the grouped fits (i.e. if one cannot clearly identify both the rising and falling slope), in order to further filter out

spurious events.

3.4.2 Analysis of Mobile Proteins on Supported Lipid Bilayers

We can extend mass photometry to the analysis of protein molecules exhibiting more complex behaviour at the surface than simply non-specific binding. A natural extension would be to membrane-binding proteins diffusing on a supported lipid bilayer (SLB), as it has been previously shown that SLBs can be prepared on glass in a manner that does not introduce excess scattering background to an iSCAT image[17] and viral capsids have been tracked moving on an SLB.[16]

In order to determine not only the particle contrast, but to be able to follow the molecule as it diffuses freely on the upper leaflet of an SLB, we turn to the other approach to generating a background image - namely, taking the median pixel value through a stack of images containing a mobile particle, so that the background contains the detail of static features but not the signatures of sufficiently mobile particles. In order to counteract the effect of long-term sample drift, rather than taking the median over the entire stack of acquired images, for each frame we take only a sub-stack of images centred on that frame and calculate the median image of that sub-stack, updating the background for each image. Each ratiometric image is then a single raw frame divided by the local median calculated from N' frames centred on that raw frame (Figure 3.7b). The choice then is the value of N', or how long the sub-stack should be - it must be sufficiently long that a particle moves by more than twice its size in the image so that it does not contribute to the median image, but if it is too long then the effects of drift become apparent once more. For a particle with a diffusion coefficient of 5 μm^2 s^{-1} (towards the upper end of diffusion coefficients measured for lipids in SLBs, at least on glass, and at the upper end

of what is typically considered measurable by single particle tracking),[102,103] then the typical time taken to move a root-mean-square displacement of 500 nm would be 12.5 ms. Choosing a window size of 50 ms should therefore be a good start (although it can of course be updated and the ratiometric frames recalculated later should this number require amendment).

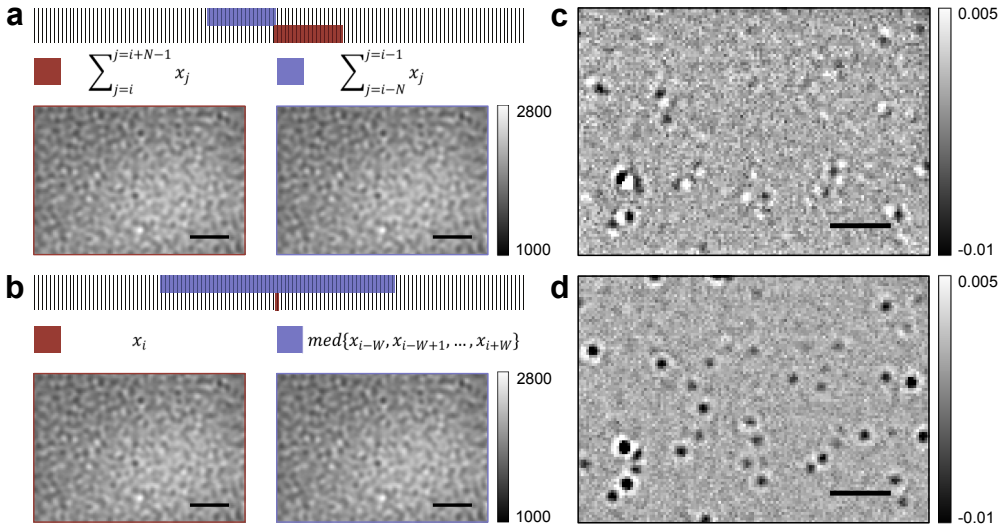


Figure 3.7: Comparison of background estimation from the median of a centred local window to that from the average of a preceding window. (a) Illustration of the image averaging and background division approach. The equations denote the operations performed on the frames highlighted by the corresponding coloured boxes. The images are the resulting averaged frames, exhibiting the familiar features associated with the roughness of a clean glass surface. (b) Illustration and images of the local median background estimation approach designed for the detection of mobile particles. (c, d) The ratiometric images calculated as the 'red' image divided by the 'blue' background image in (a) and (b) respectively. The ratiometric image in (d) is the average of 2 ratiometric frames calculated as per panel (b), in order to have the same time resolution as in (c). Scale bars = 2 μm.

Were one to apply the sliding ratiometric filter described in the previous section to a series of images containing a moving particle, the result would be ratiometric images containing paired bright and dark spots, with the bright contribution arising from the region where the particle was present in the first bin and not the second, and the dark spot from where the particle has moved to (Figure 3.7c). The orientation of the paired features corresponds

to the direction the particle has moved on average between the frame bins, but the intensities of the peaks depend not only to the size of the particle but also on how far it moved between the two frame bins, making a quantitative analysis of the distribution of particle sizes non-trivial. By instead taking the background from the median of a local sub-stack as described above, the particles are revealed more simply as diffraction-limited PSFs centred on the average position occupied during the integration time of that frame (Figure 3.7d). For the ratiometric image shown in Figure 3.7c, the number of frames averaged in each frame bin was 2 (i.e. N=2, to use the notation of the previous section). For that shown in Figure 3.7d, the median over a window size of N'=101 frames was used to estimate the background about each individual frame, and the resulting ratiometric images were then 2-fold averaged to give the same time resolution as the other approach. It is interesting to note, therefore, that for the same time resolution (of 2 frames = 7.6 ms) the SNR of the latter approach appears superior. This is because the background is taken over a substantially longer time window (the median of 101 frames, rather than the average of 2), meaning there is less shot noise on the estimate of the background and therefore less noise in the resulting ratiometric image.

From the resulting sequence of ratiometric frames, particles can be identified and fitted in much the same way as described previously. For the data shown here, the image was convolved with a LoG kernel with σ = 1.5 pixels = 127 nm rather than an experimentally derived PSF, principally for the sake of convenience (the open-source Python library Scipy has a built in LoG filter), and because the performance was not found to differ substantially. A threshold is applied to this filtered image for particle detection, along with the local maximum search as described before to identify only a single pixel per particle. The extracted candidate ROIs were fit to the more complex model

PSF described earlier (developed and implemented in Python by Max Hantke) rather than the DoG function used elsewhere.

These individual fits must then, as before, be linked into trajectories. The difference here is that each particle changes position from frame to frame, and so the linking must allow a particle to move up to a certain distance from one frame to the next. This is a standard problem in single particle tracking, for which there are a number of software packages/algorithms available. Here, we made use of the trajectory linking functions of the Trackpy package.[104,105] Following a similar argument as for the selection of window size for the background estimation, a particle with diffusion coefficient 2 μm^2 s^{-1} would take an average step size of ∼250 nm in the 7.7 ms integration time for this dataset. For the time being, we set a cutoff threshold of 4 pixels = 338 nm in this step as the maximum distance a particle could move between frames before being considered a different trajectory (though of course this threshold could do with some more rigorous optimisation). The images shown in Figure 3.7 are at rather higher particle density than would be ideal for confident linking without risk of confusing one particle with another in this linking step, but this data is sufficient for a demonstration of the principle of this background subtraction approach.

An example particle trajectory is depicted in Figure 3.8. Fits to a series of images (Figure 3.8a) of the membrane-binding protein dynamin diffusing on a supported lipid bilayer are linked into a single trajectory (Figure 3.8b). The contrast of the particle as a function of time appears fairly constant, with the exception of a period of lower contrast at the beginning of the trajectory (Figure 3.8c), possibly associated with the protein not being fully bound to the bilayer during the first 100 ms or so. A histogram of these contrast values shows a roughly normal distribution (Figure 3.8d), with the exception of those

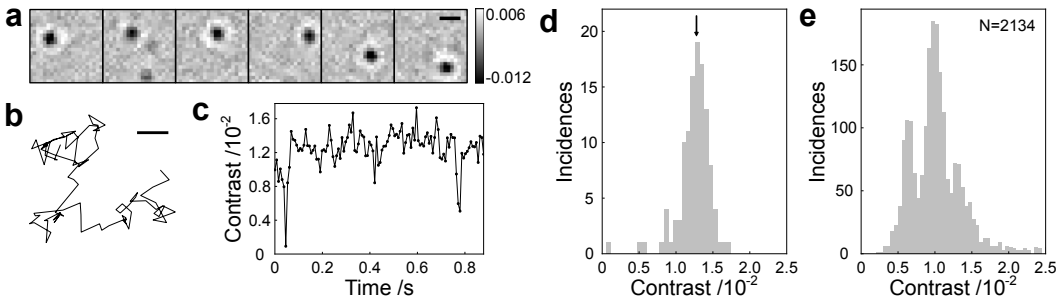


Figure 3.8: Tracking of unlabelled protein molecules diffusing on a supported lipid bilayer. (a) Example ratiometric images of a dynamin oligomer diffusing on a supported lipid bilayer. Images were acquired with an effective frame rate of 131 fps, with the snapshots shown here being 115 ms apart. Scale bar: 500 nm. (b) Corresponding trajectory from fitting the images to a model PSF. Scale bar: 250 nm. The maximum particle displacement allowed between frames for the trajectory linking here was 4 pix (=338 nm). (c) Corresponding trace of the contrast of the particle vs time. (d) Histogram of contrast values from the single particle trajectory. The arrow marks the median contrast value of the particle over the course of the whole trajectory. (e) Histogram of the median contrast values from 2134 trajectories, showing the presence of different species. Trajectories of length <10 frames were rejected when generating this histogram.

early low contrast events, the centre of which can be reliably identified by taking the median value. Inspecting the median contrast value of many such trajectories reveals the presence of multiple oligomeric states of dynamin on the membrane, identifiable by the differences in their characteristic contrast (Figure 3.8e).

The analysis of such iSCAT movies with mobile particles described thus far is arguably somewhat limited in scope, focusing on the mass photometry aspect of the data in keeping with the focus of the rest of this thesis. There is clearly much more information to be extracted from these trajectories, however. The most obvious next step is to extract diffusion coefficients from the XY traces,[11,106–108] while the length of the trajectory also provides the residence time on the bilayer. Correlating these with measured scattering contrast ought to provide information on the diffusion behaviour and affinity towards the lipid bilayer in an oligomerically specific fashion, properties which can be

further probed by varying the lipid composition of the bilayer. Perhaps most excitingly, the ability to not only observe single mobile proteins on a lipid bilayer but also to distinguish different oligomers thereof by their scattering contrast raises the possibility of the label-free observation of membrane protein complex assembly/disassembly at the single subunit level.

3.5 Observations and Considerations

We now return to the more standard landing assays used for mass photometry (e.g. as were used for the acquisition of the data presented in Chapters 3 and 4), with a discussion of various considerations and observations on the execution of the experiments and analysis of the data.

3.5.1 Determination of Optimal Focus Position

One difficulty associated with making reproducibly quantitative measurements of the contrast of scatterers such as protein molecules that cannot be seen above the glass roughness background is how reliably the sample can be put into focus from experiment to experiment. As the image contrast depends on the position along the optical axis at which the sample is positioned during the measurement, the precision on the measured mass between experiments will depend on being able to place the sample reliably in focus. The challenge arises from the fact that the objects of interest can only be visualised once, as they bind to the surface, while the exponential drop in binding rate with time described in the previous chapter means that after addition of sample one would not want to spend additional time putting the sample in focus based on the binding events one can then see as you then risk losing most of the binding events. Rather, it would be preferable to put the sample in focus first based

on some other measure, and then add sample and start recording as soon as possible.

Given the requirement for a clean surface devoid of large scatterers for these experiments, the only feature in the image before addition of sample is the glass roughness itself. While, with practice, one can put this in focus fairly well by eye, given that the roughness appears as an apparently random pattern of diffraction-limited features this procedure will always be rather subjective and prone to user error. Instead, we assume that the features giving rise to the glass background are optically equivalent to the proteins to be measured, in the sense that they are both non-resonant scatterers of a size well below the diffraction limit and lie within the same focal plane (to within a few nm). The focus position at which one gets the maximum contrast for a protein binding event would then also be the position which maximises the glass contrast. This is evaluated by normalising the raw images by an estimate of the illumination profile (by the median filter described in the previous section) in order to account for variations in illumination profile along the optical axis (although this may not be critical, as the illumination beam is typically only focused to $\sim$1 μm FWHM and so changes rather more slowly through the focus than do diffraction-limited features) and then taking the standard deviation of this normalised image as a measure of the total contrast of the glass features over the image. The position at which this metric is maximised can be set as the target focus position (Figure 3.9), and is actively maintained through an independent feedback loop (as described in Chapter 4).

Whether or not the focus position determined in this way is strictly the optimal focus for a mass photometry experiment is dependent on the validity of the assumption that the contrast of both glass features and protein binding events are maximal at the same point, and on how accurately this method

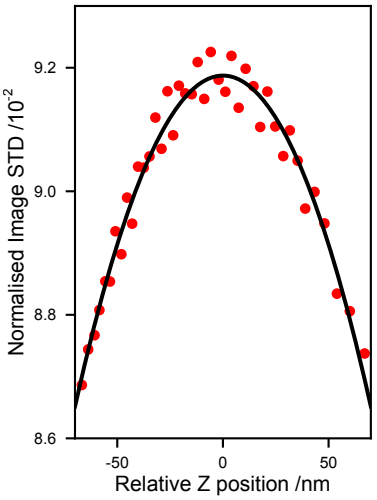


Figure 3.9: Glass contrast vs focus position. Standard deviation of the image of glass roughness in buffer, evaluated after normalisation for illumination profile, as the sample is translated through Z. A fit to a second order polynomial is shown, and the Z position is shown relative to the maximum of the fit.

of calculating the glass contrast reproduces the true contrast of the surface features. It is clear from the images acquired and results generated, however, that this method performs sufficiently well for the measurements described in the previous chapter. Moreover, the most significant feature of focusing in this way is not whether it finds the absolute best focus, but that it enables the focus position determined for each coverslip to be more reproducible from experiment to experiment than if judged by eye. It also, in principle, enables automation of the focus-finding procedure, since calculation of this metric in real time is straightforward. In practice, the data presented in this thesis were all taken with the focus position still determined by hand, using the real-time readout of the normalised image STD, with substantial frame averaging in order to reduce noise and aid identification of the maximum.

3.5.2 Selection of Optimal Averaging Window

It may seem an obvious thing to state, but the ability to accurately detect and quantify PSFs in the ratiometric images depends crucially on the noise in the

ratiometric image, both in terms of the magnitude of the noise (noise level) and its spatial properties (i.e. whether it is white noise as would be expected for shot noise limited images, or whether there are spatial patterns that appear). The principal relevant parameter to consider in the analysis is the choice of the length of the averaging window (N in Section 5.1.1). Increasing the averaging window by averaging more frames increases the number of photons collected per averaged image (effectively increasing the full well capacity of the camera at the expense of time resolution), thereby lowering the shot-noise-induced fluctuations in the ratiometric image, with the fluctuations reducing as $1/\sqrt{N}$.

Figure 3.10a illustrates how the noise level typically evolves with integration time for the setups used in this work. Starting with an iSCAT movie of a clean glass surface immersed in buffer (i.e. with no protein binding events), we calculate ratiometric images for a given integration time, as described above. The noise in each image is evaluated by taking the standard deviation of the pixel values in the ratiometric image. Initially, the measured points follow the shot-noise-limited trend, decreasing with a slope of $-\frac{1}{2}$ on a log-log plot. From about 50 ms, the noise level decreases more slowly than expected if limited purely by shot noise, and after about 200-300 ms begins to rise. This likely occurs as a result of sample drift giving rise to features in the ratiometric image due to the glass surface being in a slightly different place in each frame bin. For a setup with a glass contrast of $\sim$11% RMS as here, a ratiometric signal of $\sim 5 \times 10^{-4}$ (approximately the shot-noise-limited noise floor) is generated by a translation of only 0.2 nm.

Although it is tempting to simply aim for the averaging time that results in the lowest noise level (about 200 ms), this turns out to be counterproductive in terms of the error on the quantification of the contrast of each particle, as illustrated in Figure 3.10b. This shows an example for two proteins, the

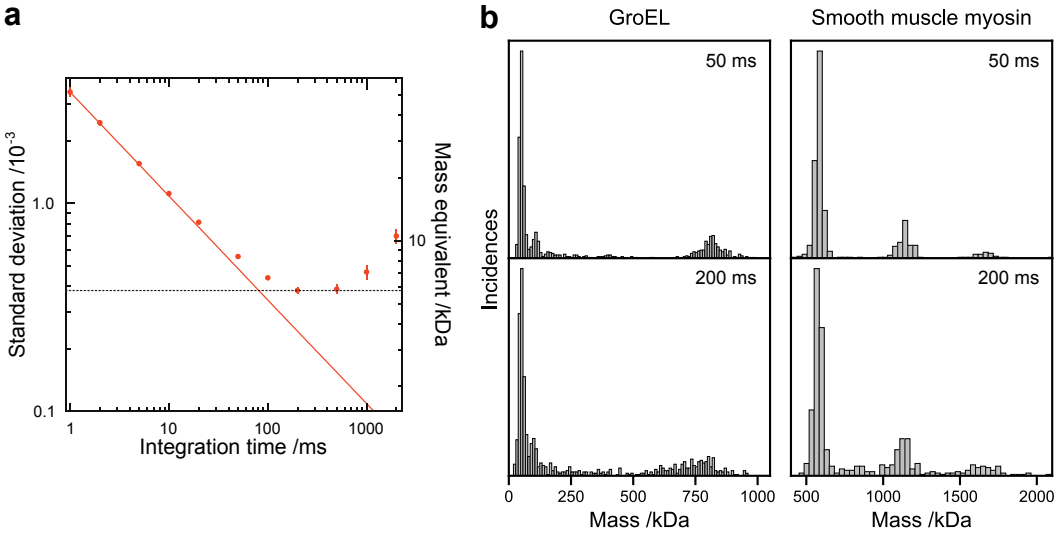


Figure 3.10: Effect of averaging time on measured mass distributions. (a) Standard deviation of pixel values in ratiometric images as a function of integration time calculated from an iSCAT movie of buffer with no protein present. The straight line shows the shot noise limited trend. (b) Example mass histograms for 2 proteins illustrating the effect of choice of integration time.

800 kDa 14-mer GroEL and cross-linked smooth muscle myosin (∼500 kDa), of the results of analysis at 50 ms integration times (i.e. time at which the noise level is lowest while still being close to shot noise limited) compared to 200 ms (where the noise reaches its lowest value, but is definitely not shot noise limited). It is clear that the lesser averaging improves the precision with which the contrast of each individual protein binding event can be quantified, reflected in the histograms by sharper peaks and a reduced baseline density. In the case of GroEL, for example, at 50 ms integration time the high mass particles are quite clearly clustered into a peak centred on 800 kDa, and at low mass at least two peaks are discernible and lie at the expected masses for the monomer and dimer of the subunit. At 200 ms integration time, meanwhile, the high mass peak is significantly broader, to the extent that it isn't really identifiable as a clear peak above the baseline, and the lower mass species are also less well resolved.

There are at least two possible reasons for this effect. One is related to the

loss of time resolution. The longer averaging window effectively spreads the signal from a binding event (which is rapid - shorter than a single frame time) over more frames in the ratiometric movie, leading to a higher particle density in each ratiometric image and thus increasing the chance that the presence of one binding event influences the fitting of another binding event. As an aside, this effect is also what sets the upper limit on the concentration at which a sample can be measured with a given temporal resolution (depending also on the size of the species of interest, both in terms of how long one needs to average for in order to confidently detect the binding events, and in terms of how far away from the particle centre the outer lobes of the PSF remain above the noise level).

A second possible cause could be related to the fitting algorithm itself. Here, the data was fit to a PSF model using a least squares minimisation algorithm. The least squares measure of the difference between data and a model is the maximum likelihood estimator (i.e. attains the best possible level of precision) under Gaussian noise, which is a good approximation for Poisson noise in the limit of large numbers of detected photons. One would therefore expect it to perform best under shot noise limited conditions, while deviation from shot noise corresponds to the introduction of features to the image that cannot be described by the PSF model but also do not resemble Gaussian noise.

3.5.3 Spatial Correlation of Binding Events

In addition to the interferometric contrast and binding time of each single molecule binding event, the imaging aspect of this method means one also observes the spatial location of each binding event with a precision of up to a few nanometres.[19] In combination with a specifically functionalised surface, where the location of binding sites is either already known or can be measured

independently (e.g. through correlative fluorescence imaging), this information could be used to help alleviate the low specificity of the scattering signal.[109] This work does not make use of any surface functionalisation, relying instead upon the non-specific binding of proteins to a clean glass surface - a situation in which the spatial location of the binding events is perhaps of minimal interest. It is a diverting aside, however, to note that this spatial information allows us to probe whether or not the distribution of binding events across the glass surface is indeed random. In principle, the surface properties/charge of a given protein might affect its distribution of binding sites on the glass surface, especially if the glass surface displays a relatively wide range of surface charge sites in solution, as has recently been suggested.[110]

A scatter plot of the locations of binding events for a representative measurement of a small heat shock protein binding to a clean glass surface is shown in Figure 3.11a. Qualitatively, the events look fairly randomly distributed, with perhaps a suggestion of some regions with higher or lower density of points. For the purposes of making an objective and quantitative comparison, however, we compare the distribution of nearest neighbour distances (NNDs) to those expected under a model of complete spatial randomness (CSR). That is, under the assumption that the events are independently and uniformly distributed across the observation area, then the distance from any one point to its N-th nearest neighbour is distributed according to the following probability distribution function

$$P_N(r) = \frac{2}{(N-1)!}\lambda^N r^{2N-1} e^{-\lambda r^2} \tag{3.10}$$

where $\lambda = \rho/\pi$, with ρ being the average density of points over the area inspected.[111]

Figure 3.11a also shows the N-th NNDs for N = 1-5 (the black lines), together with the predicted distribution for the measured particle density under CSR (red lines). There is some discrepancy between the measured data and the CSR model for all N considered, with the measured distribution appearing a little biased towards shorter distances, suggesting a degree of clustering in the locations of the binding events. To simplify the process of quantifying this over several datasets, we condense the information on just the first nearest neighbour into a test statistic, Z, defined as

$$Z = \frac{\langle NND \rangle - \mu}{\sigma_{mu}} \tag{3.11}$$

where $\langle NND \rangle$ is the measured mean NND, μ is the mean NND under the CSR model for the density of particles in the measurement, and σ_{mu} is the standard error on the mean under CSR (that is, the standard deviation of the distribution expected under CSR divided by the square root of the number of particles measured). Z is defined in this way since the central limit theorem dictates that, in the limit of a large number of particles sampled, the difference between a sample mean and the true population mean will be normally distributed about 0 with a standard deviation of $\sigma/\sqrt{N}$. Thus, if the data is CSR-distributed (and the sample size large enough), this test statistic will be normally distributed with a mean of 0 and standard deviation of 1. The values of Z for 16 different datasets (involving 4 different proteins) are given in Figure 3.11b (blue dashed lines), together with a kernel density estimate of the distribution of these values (black line) and the distribution under the null hypothesis (grey line). This also appears to suggest a mean NND that is consistently lower than that expected under CSR for almost all datasets, strongly suggesting that the binding events do indeed cluster into regions with a higher probability of protein binding.

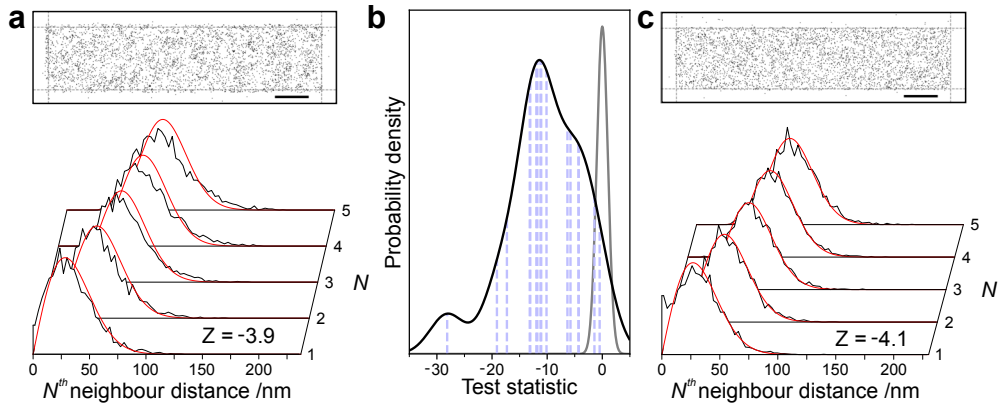


Figure 3.11: Analysis of the spatial distribution of binding events. (a) Top: scatter plot of the locations of the binding events extracted from a single movie of a small heat shock protein binding to a glass surface. The dashed grey lines denote the useable area of the image taken for further consideration. Bottom: N^{th} nearest neighbour distributions (N = 1-5) extracted from these locations (black), together with the prediction under complete spatial randomness for the measured particle density (red). Number inset is the test statistic for the first nearest neighbour distribution as defined in the text. (b) Distribution of such test statistics from 16 independent movies (black), with each value marked as a dashed blue line. The distribution under the null hypothesis is shown in grey. (c) As (a), but with glass cleaned by sonication rather than rinsing, and using a different protein. Apart from a high density of very close events in the first nearest neighbour distribution, the agreement between prediction and experiment is remarkably good. Scale bars: 1 μm.

Complicating the picture somewhat is a more recent dataset measured using glass that had been cleaned by sequential ultrasonication in milliQ, then isopropanol, then milliQ, as opposed to simply rinsing as described in the Methods sections of previous chapters. Note also that this dataset is from a different protein than the previously considered measurements, so the interaction with even the same surface could in principle be different. Although the first NND distribution indicates an increased density of very short distances (reflected in the Z-value of -4.1, which would suggest non-spatially-random binding), the NND distributions for N = 2-5 show remarkable agreement with the predicted distributions assuming CSR (Figure 3.11c), suggesting that the location of binding events in this case might indeed be randomly distributed. Further investigation is needed to determine whether there is

indeed a dependence on the cleaning procedure used, or if this is a reflection of differences in the behaviour for different proteins.

This may seem inconsequential, and indeed so it may prove, but it is possible that this does have some implications for the mass resolution of the technique. For instance, having another binding event close in both space and time to the one being fitted leads to an influence of the PSF of the other particle on the fit (effectively, this is adding noise that is not shot noise) and therefore a loss of precision in the PSF fitting, resulting in broader peaks in the mass distribution. Beyond that, if the degree of randomness or clustering is dependent on the distribution of surface charge on the substrate and/or on the surface properties of the protein, then such an analysis might in principle be used to gain access to additional information on the protein being measured beyond simply its mass.

3.6 Limitations and Future Directions

3.6.1 Mass Resolution

As demonstrated in Figure 5.4c, the peak width increases with increasing mass (i.e. position of the centre of the peak), with a standard deviation typically 10% of the peak position. Although this is sufficient for low-order oligomeric resolution (e.g. the BSA in Figure 5.2, and the Env in Figure 5.5a), it does somewhat limit the scope of this technique, for example in examining large complexes composed of relatively low mass subunits. One might expect that the ultimate limit on the peak width ought to be the shot-noise-induced fluctuations in the ratiometric images, as is achieved in the low mass limit (Section 4.2), and so we consider possible sources of peak broadening beyond this limit.

The contrast of a particle is determined by the change in reflected intensity between the presence and absence of that particle, as a proportion of the

intensity of the reference field (reflected intensity) in the absence of the particle). We have seen in Chapter 3 how we can tune the contrast by altering the strength of the reference field, in that case by selective attenuation in the back focal plane of the microscope objective. Inspection of the raw images (e.g. Figures 4.2, 3.7), however, reveals local, diffraction-limited variations in the reflected intensity, even within regions apparently subject to the same incident intensity. This is not a new observation - indeed, it is this speckle-like background from inhomogeneities in the glass coverslip surface that is the limiting source of background that requires subtraction in order to reveal the signatures of single protein molecules at all. An additional, as yet unconsidered, consequence of this variation could be that it leads to a local modulation of the interferometric contrast.

More specifically, the contrast as defined by Eq.3.5 is dependent on $\frac{1}{r}$, where $r = \sqrt{R}$ is the square root of the proportionality constant between the incident intensity and detected intensity in the absence of a particle (in a simple iSCAT setup with no partial reflector, this is the reflectivity of the surface). As the intensity of the reference field, $R|E_i|^2$, is modulated by local variations in R, therefore, one would expect a dependence of the measured interferometric contrast on the local reflectivity of the glass-water interface (Equation 3.12):

$$C_{meas} = \frac{2|s|}{r}\cos\phi = \frac{C_0}{\sqrt{R}} \tag{3.12}$$

To explore this further, we take a dataset exhibiting multiple well-resolved peaks extending to contrasts of up to 2 %. For each single molecule binding event, we can look up the corresponding pixel value in the raw frame immediately before binding and normalise to the median pixel value in the frame (i.e. neglecting inhomogeneities in illumination profile). A plot of this normalised reflected intensity against the contrast of the corresponding single molecule

binding event reveals some correlation, with the effect apparently increasing for higher mass portions of the distribution (Figure 3.12a, left). Overlaying the predicted $\frac{1}{r}$ trend on these data suggests that this correlation broadly follows the expected dependence, although the width of the distribution perpendicular to these trend lines still increases at higher contrast, suggesting there could still be something else at play (Figure 3.12a, right).

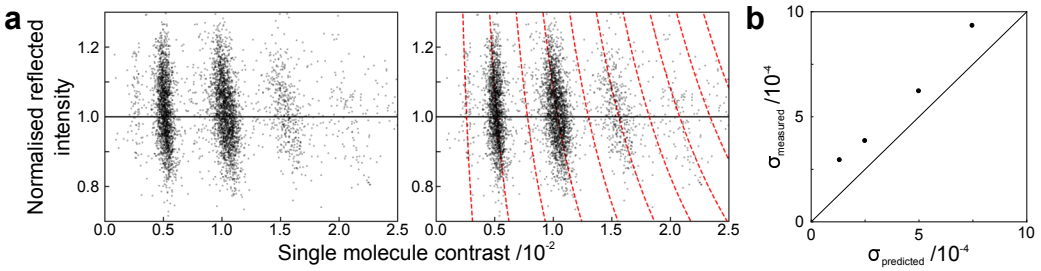


Figure 3.12: Influence of local reflectivity variations on measured protein contrast. (a) Left: scatter plot of measured contrast of single molecule binding events against the normalised intensity of the glass background at the point where the binding event occurs. Some correlation is observed. Right: the same plot with red lines drawn denoting the expected correlation of single molecule contrast with $\frac{1}{r}$ (Eq5.8). (b) Experimentally observed peak width (1 standard deviation), as determined by fitting to a Gaussian mixture model, against the expected width predicted from the variation in the background intensity of the glass roughness.

To be more quantitative about this, we can predict the peak width that one would expect given the width of the distribution of reflected intensities by treating this as an uncertainty on the value of R in Equation 5.8, and using propagation of errors to calculate the expected error on C_{meas}, σ_{pred}, assuming that this is the only source of peak broadening (Eq 5.9).

$$\sigma_{pred} = \frac{C_0 R^{-\frac{3}{2}}}{2}\sigma_R = \frac{C_0 \sigma_R}{2} \tag{3.13}$$

where σ_R is the standard deviation of the normalised reflected intensities of the glass surface, and the second step follows since R is referring to normalised reflected intensities and thus has an average value of 1.

Plotting the measured peak width (standard deviation) against this prediction seems to show that the broadening from local glass contrast can explain some but not all of the measured peak width. This is to be expected at the lower end of the plot, where the predicted broadening from local reflectivity variations falls below the lower limit dictated by shot noise. Some of this discrepancy could be due to incorrect estimation of the local reflectivity due to inhomogeneities in the illumination profile, which here have not been accounted for (only the median intensity over the whole frame was used for normalisation), but could in principle be by dividing the raw images by an appropriate estimate of the illumination profile. It is also possible that there are non-negligible contributions to the detected intensity at the camera from stray backreflections (e.g. from the lenses in the objective) that function as spatially variant incoherent background (incoherent, that is, assuming that the distance between the principal reflection and all these others is greater than the coherence length of the illumination source). If this were the case then it would add yet another contribution to variations in pixel intensity, and would appear in any estimate of the illumination profile, thereby making any correction without first accounting for this contribution unreliable.

Given this contribution to the increase in peak width can be measured and modelled, it should be straightforward to correct for this effect simply by multiplying each measured contrast by the corresponding value of r, subject to being confident of having an accurate measure of that quantity. Further work is needed, however, firstly to determine how well such a correction works after accounting for illumination inhomogeneity and additional background, and then to explore further effects that may contribute to the peak broadening. Such effects may or may not include sample drift (either about the focus, leading directly to contrast variation, or laterally, leading to an increase in

noise in the ratiometric images), an effect which could be improved with more stable stages and/or better active 3D stabilisation of the sample.

Alternatively, it is possible that nanoscopic variations in the dielectric environment for binding events at different locations on the surface might sufficiently alter the scattering emission pattern (e.g. through differences in the amount of near field emission converted into propagating light at the glass interface) so as to change the number of scattered photons collected enough to produce a broadening of the peak. If this is the case it would be rather more difficult to quantify with a diffraction-limited optical microscope.

3.6.2 Precision

As discussed in the previous chapter, the shot-to-shot reproducibility of the mean mass measured for a sample is limited to 1-2% of the molecular weight, sufficient to detect a 1 kDa shift in the mean of a ∼50 kDa protein. This is larger, however, than the variation one would expect just from the statistics of sampling the same distribution repeatedly, which should result in a precision given by $\sigma/\sqrt{N}$, where σ is the standard deviation of the distribution and N is the number of samples. Given the standard deviation of a single peak was typically ∼10% of the mean for the data presented in the previous chapter, and the number of events detected within that peak $\sim 10^3$, the statistical limit on this precision should be on the order of 0.3% of the mean. In fact, an experimental limit of 1% corresponds to the statistical limit for 50-100 particles, meaning that all the particles collected beyond this do not contribute to improving the precision of the measurement.

In order to confirm that this limitation is indeed from shot-to-shot variability, and not an intrinsic limitation of the detection method, we inspect the behaviour of the error on the mean of randomly selected sub-samples from a single

experiment with many particles. Specifically, we take a dataset of alcohol dehydrogenase (ADH, 147 kDa) in which we have detected 2084 under the tetramer (147 kDa) peak. Taking only these particles under that peak, we then sub-sample for a given number of molecules, N, by randomly selecting N particles from the 2084 total and calculating the mean of the sub-sample. That sub-sample is removed from the list, from which another sub-sample of size N is again drawn at random and the mean calculated. This process is repeated until there are fewer than N particles left in the list (which occurs before 50 iterations for $N > 40$ sample size), and the standard deviation of the mean values is calculated. This process is repeated for a range of N from 1 to 200, and for each N the whole process is repeated 50 times in order to generate an estimate of the error on the standard deviation. Figure 3.13 shows the results of this process as a function of N, with the black line denoting the statistical limit (that is, a straight line of slope $-1/2$ on the log-log plot). The error on the mean is given as a relative error, i.e. divided by the mean contrast determined from the whole population. At $N = 1$, the error on the mean corresponds to the standard deviation of the peak - the expected $\sim$7% of the mean. As N is increased, the error on the mean decreases as $1/\sqrt{N}$ even down to 0.5% at N =200. The error on this metric increases at larger N, because there are successively fewer independent samples that can be drawn from the 2084 measured particles, but within these errors the values are consistent with the statistically expected trend. This rules out, therefore, the possibility that the precision is limited by something inherent even within a single measurement, such as from biased sampling of different glass contrasts (given we know, from the previous section, that the local glass contrast influences the measured protein contrast). Rather, there must be another factor that both influences the contrast and varies from one experiment to another; a number of possibilities come to mind.

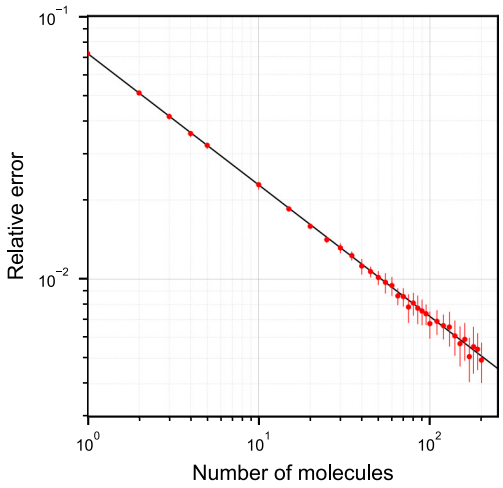


Figure 3.13: Precision on the mean contrast within a single acquisition. Standard error on the mean contrast (as a proportion of the mean contrast) evaluated from random subsampling of N particles from a total of 2084 events under a single peak as a function of N. Error bars represent the standard error from 50 independent subsampling iterations. The black line denotes the statistical limit of $\sigma/\sqrt{N}$

Firstly, since the image contrast depends on where in the focus of the microscope objective the sample is positioned, the reproducibility with which the optimum focus position can be determined before measurement ought to influence the measured contrast. The method to reproducibly find the focus position described in Section 5.2.1 was implemented for this reason, and successfully reduced the occurrence of datasets with means that deviated substantially from other measurements of the same sample, but there is clearly still some uncertainty on the determination of the position of the maximum glass contrast. One might expect, however, that if we are correct in making the assumption that the contrasts of the glass surface and of protein (both being non-resonant scatterers located within a few nanometres along the optical axis) have essentially same Z-dependence, then we are making a measurement around a maximum of protein contrast and therefore at a point where the change in contrast with Z-position is minimised.

Secondly, variations in the thickness of the glass coverslip used could be a

contributing factor. The high NA, oil immersion microscope objectives used here are all corrected to work optimally with a glass coverslip of thickness 170 μm. Although the immersion oil and glass coverslip ought to be index-matched, this is not perfect - the refractive index of the commonly used Olympus Type F low-autofluorescence immersion oil is 1.518 while that of the Schott D263M glass used for the coverslips is 1.5255 (each value reported at room temperature and a wavelength of 546.1 nm). Use of a coverslip of a thickness other than that for which the objective is designed therefore results in the introduction of aberrations into the image and a loss in contrast. The standard #1.5 coverslips used are specified to be between 160 and 190 μm thick, with an ideal thickness of 170 μm. To explore the dependence of the contrast on relatively small differences in thickness, the protein ADH was measured 8 times each on #1.5 thickness coverslips and #1 thickness coverslips (130-160 μm; ideal thickness 150 μm), returning mean measured contrasts of $3.24 \pm 0.07 \times 10^{-3}$ and $3.16 \pm 0.06 \times 10^{-3}$, respectively (these data were taken on a setup with lower contrast than that which provided the data shown in Figure 5.3). The errors given are the standard error on the mean taken over the 8 experiments per coverslip type, and at the degree of precision given are the same whether or not a correction for low sample size (assuming normally distributed data, this correction factor has a numerical value of $\sim$0.965 for $n = 8$) is applied. This corresponds to a drop in contrast of 2.6% due to the different thicknesses of the coverslips, although we cannot be sure, having only measured 8 coverslips, that the mean thickness of the sample of coverslips tested indeed reflected the ideal thicknesses of 150 and 170 μm. This comparison would suggest that variations in coverslip thickness within the 30 μm tolerance range of standard #1.5 coverslips could be sufficient to provide the limiting precision observed, depending on how the thicknesses are distributed within that range. Moving

to high precision coverslips, with a specified thickness of 170±5 μm, however, did not produce a measurable improvement.

Thirdly, it is possible that temperature fluctuations are the limiting factor here. In a similar way to the fact that imperfect index-matching requires the use of a specific coverslip thickness, one might expect that changes in the refractive indices of the oil and the glass induced by temperature changes could also result in conditions deviating from those for which the objective was designed to perform optimally, again lowering contrast through the introduction of slight aberrations. Indeed, we have noticed that upon the objective and sample region warming by ∼5 K the contrast of protein molecules can drop by up to 10%. It is therefore not inconceivable that smaller variations in temperature arising, for example, from differences in whether fresh oil is applied to the objective before each measurement and if so how much and how long before acquiring data, or from changes to the air flow around the objective, could give rise to the smaller fluctuations in contrast that are observed.

It remains unclear, therefore, as to the reason why the contrast measurement from one experiment to the next is limited to a precision of 1-2% of the molecular weight, and more rigorous experiments to test each of the possibilities outlined above (and indeed any others) would be needed to find and address the source of this limitation. This is, however, a question worth pursuing, as maintaining statistically-limited precision up to the N=1000 molecules typically measured per experiment would enable the position of a 100 kDa peak, for example, to be determined with a precision of ∼220 Da, enabling the measurement of binding curves for interactions between proteins and short peptides, and paving the way towards the detection of small molecule binding.

3.6.3 Sensitivity

As illustrated in Figure 5.4b, the nominal noise floor (in the sense of the lowest value that the standard deviation of a ratiometric image reaches as a function of integration time) corresponds to a mass of ∼6 kDa, which would naively suggest that proteins as small as 30 kDa can be confidently detected and quantified (an SNR of 5 can be considered a comfortable limit above which spots can be reliably detected and analysed in noisy images, without delving into more complex machine learning approaches).[95,112] In practice, of course, the smallest protein for which data is shown in this thesis is the 53 kDa streptavidin, although proteins as small as 42 kDa have since been measured.[113] The reason for this discrepancy lies in the characteristics of the noise causing the deviation from shot-noise-limited performance.

A comparison between ratiometric images of bovine serum albumin (BSA, 66 kDa) binding assay and a buffer control are shown in Figure 3.14a, both generated with an integration time of 50 ms. This integration time is sufficiently short to provide high quality histograms (Figure 3.10b) but also does not yield completely shot-noise-limited ratiometric images (Figure 3.10a). Closer inspection of this image (and indeed the area of the BSA image containing no particles) seems to suggest a faint pattern in the background that somewhat resembles very faint particles in terms of the scale of the apparent features. This is revealed in more detail by taking the fast Fourier transform (FFT) of each image (Figure 3.14b). The FFT of the image with particles reveals a characteristic band of spatial frequencies associated with the PSF of the microscope. In FFT of the image of just buffer, one sees not simply the white noise spectrum expected for shot noise, but also a faint increase in intensity covering a similar band of spatial frequencies to those apparent in the image containing BSA molecules. Taking the average of the FFTs of 400

such images with and without BSA molecules reveals this more clearly (Figure 3.14c) - the spatial profile of the limiting noise very closely resembles that of diffraction-limited particles. As such, distinguishing lower SNR particles from the background in such images is likely to be all but impossible using only the spatial information in each image. Specifically, the ratio of the intensity of these bands above the baseline, the one arising from 66 kDa protein molecules, the other from the background present in the buffer, suggests that this background corresponds to a mass-equivalent of around 32 kDa, suggesting this as a lower limit of robust detection on a per image basis, and that somewhere around 42 kDa might indeed be close to the lower limit of detection for the experimental setup as it currently is.

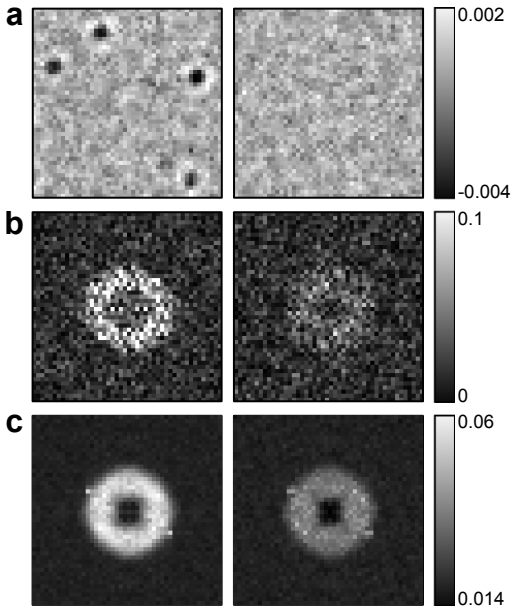


Figure 3.14: Limitations in the detection of small species. (a) Example ratiometric images of BSA binding (left) and a buffer control (right), each at an integration time of 50 ms. (b) The corresponding FFT of these images. (c) Averaged FFTs of 400 such images with (left) and without(right) protein signals.

The brute force approach to getting round this is to increase the incident laser power and use a faster camera. In this way one would achieve a similar shot noise level with shorter integration times, hopefully before the source

of this 'other' noise has reached a similar level to that which it reaches here. This assumes, of course, that this additional noise source exhibits a slower behaviour in time than the binding of a molecule to the glass surface, which seem to occur within one frame. This would be the case if it is indeed sample drift causing these fluctuations, for example. An alternative, provided again that the temporal behaviour of the binding events and the limiting noise are different, might be to devise a time-based filter to apply to the raw images that is more selective for sharp changes in pixel intensity than simply taking the ratio between means of adjacent frame bins, which is all we have done here.

In addition to sample drift (the effect of which might also be somewhat alleviated by further efforts to improve sample stability), it is imaginable that there could be some contribution arising from beam pointing noise in the imaging path (e.g. from air density fluctuations along the optical path, the effect of which could be reduced by flooding the beam path with helium, for example),[114] or even that the observed features are indeed real features of the sample (such as nanoscopic contaminants, or short-lived variations in the ordering of water around the charged glass surface).

Chapter 4

Numerical Aperture Filtering in Interferometric Scattering Microscopy

This chapter has been adapted from the following publication: D. Cole, G. Young, A. Weigel, A. Sebesta and P. Kukura, Label-Free Single-Molecule Imaging with Numerical-Aperture-Shaped Interferometric Scattering Microscopy, *ACS Photonics*, 4(2), 211-216 (2017),[115] doi: https://pubs.acs.org/doi/10.1021/acsphotonics.6b00912. Further permissions related to the material excerpted should be directed to the ACS.

4.0.1 Contributions

The construction of optical setups, and the acquisition and analysis of data was performed by Daniel Cole and myself, with equal contribution. Olya Tkachenko and Justin Benesch provided the sample of HSP16.5, and Joanna Andrecka provided the microtubules acquired the mictrotubule images shown in Figure 4.5.

4.1 Introduction

As discussed in Chapter 2, the key challenge in the optical detection of single molecules without fluorescence lies in the ability to distinguish the weak

extinction or scattering signals from background signatures that overpower them. In the context of molecules on a microscope cover glass surface, this relies, as we have seen, on the ability to precisely measure the background scattering from the static glass surface while the signal of interest exhibits dynamic behaviour such as binding to or moving across the surface. Digital subtraction (or division) of the background features can then reveal images containing only those dynamic features and the Poisson-distributed noise associated with counting discrete events (photons) incident on the camera pixels. Provided that this shot-noise-limited performance can be maintained, for example by minimising mechanical perturbations and changes in the illumination pattern, the detection of smaller and smaller signals then becomes simply a question of suppressing shot noise by making use of higher incident light intensities.

It is informative at this point to consider why the first all-optical, non-resonant detection of single protein molecules was achieved using a microscope operated in reflection rather than transmission.[19,20] We have already established that the ideal, shot-noise-limited SNR for weak extinction signals is independent of the intensity of the reference field for a given incident power and integration time, since both the interferometric contrast and shot noise scale with the square root of the reference intensity. There should thus, in principle, be no difference in SNR between an experiment performed in transmission or reflection. In practice, however, the lower extinction contrast in transmission requires suppression of additional noise sources to the ppm level,[83,84] which is experimentally extremely challenging given, for example, that commercial laser sources typically exhibit intensity fluctuations on the order of 0.1% (RMS) of the mean.[84,116] Additionally, for a given incident light intensity, a transmission measurement requires collection of 200x more light than a reflection measurement (for the glass-water interface under consideration here).

Even for iSCAT-based measurements, the detection of single molecule signals in biologically compatible environments is a challenge. The reflectivity of the glass-water interface combined with the extinction cross sections of single proteins results in iSCAT contrasts on the order of 0.4%/MDa of molecular mass. The shot-noise-induced background fluctuations as a percentage of the detected signal for a shot-noise-limited experiment is given by $\sqrt{N}/N$, where N is the number of detected photoelectrons per pixel. The detection of signals of 0.1% contrast (approximately equivalent to a 250 kDa protein) with an SNR of 10 therefore requires the collection of 10^8 photoelectrons even for a perfectly executed experiment. This poses a problem, since most commercially available digital cameras have full well capacities on the order of 10^5 photoelectrons, thus requiring significant temporal and spatial averaging in order to detect the necessary number of photons. Thus, while simply increasing the incident laser power can in principle continuously lower the sensitivity of iSCAT detection, in practice the limited readout speed of the camera (for a given number of pixels) and the inevitable contribution of background noise sources such as sample drift when averaging for more than 0.1-1 s places experimental limitations on the amount of light that can be used.

An attractive approach to facilitate label-free single-molecule imaging would thus be to increase the contrast of weak scatterers by reducing the intensity of the reference field still further. In this way, for a given incident power, a given signal could be detected at the same SNR with the collection of fewer photons, thus requiring much less averaging. More significantly, the incident laser power can then be increased, thus improving the shot-noise-limited SNR, provided either that the reference field can be sufficiently attenuated or that a combination of reference field attenuation and conventional averaging to increase the number of detected photons is used.

The question is then how to achieve this reduction in the strength of the reference field. One approach could be to appropriately coat the glass substrate in order to reduce the reflectivity of the interface, although residual reflections from within the microscope objective may limit the scope of this approach. Anti-reflection coatings on a thin coverslip could also be costly to produce, and would alter the surface chemistry such that assays that require surface functionalisation (for which techniques on a glass surface are well-developed) would require substantially more work to develop.

Alternatively, one could take advantage of the different directionalities of the illumination (reflected) and scattered light to spatially discriminate between the two in the back focal plane of the microscope objective (Figure 4.1). As has been previously shown, a point source near a refractive index interface emits a substantial proportion of the radiated photons into the higher index material at angles around the critical angle of the interface (and thus associated with high numerical aperture of collection).[117–119] The reason for this is that a portion of the near-field emission ('forbidden light' that cannot propagate in the low index medium) is able to propagate in the higher index material due to the shorter wavefront spacing, and so can be detected by far-field optics. Wide-field illumination at the sample plane, meanwhile, corresponds to low spatial frequencies in the back focal plane, corresponding to low numerical apertures and usually achieved in optical microscopes by focusing an incident beam into the back focal plane of the imaging objective. The use of a small mirror near the back focal plane of the imaging objective (for illumination through the same objective),[120] or a stop in the same position combined with illumination from above,[121] results in efficient dark-field imaging, with the latter study demonstrating suppression of the illumination light by more than 7 orders of magnitude with little loss in the detection efficiency of scattered

light for point-like scatterers.

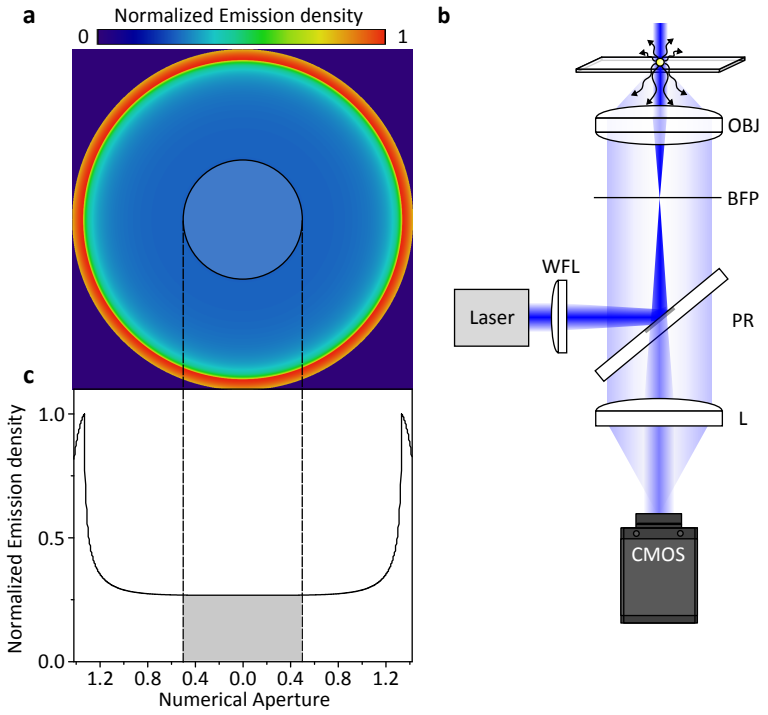


Figure 4.1: Concept and realisation of numerical aperture-filtered interferometric scattering microscopy. (a) Emission pattern of a nanoscopic scatterer at a glass-water interface emerging from the back aperture of a high-numerical-aperture (1.42) objective for circularly-polarised illumination.[117] The semitransparent circle indicates the region occupied by a partial reflector shown in the schematic experimental setup in (b). Here, a single-mode fiber-coupled diode laser is loosely focused with a wide-field lens (WFL) into the back focal plane (BFP) of an oil immersion objective (OBJ). The partial reflector (PR) couples illumination light in and out of the inverted microscope and attenuates the reflected light before being imaged onto the camera (CMOS) by another lens (L). (c) Emission density as a function of numerical aperture, with the gray area indicating the region attenuated by the partial reflector.

If, rather than being wholly reflective or absorptive, the mirror consists of a thin metallic layer coated onto a glass window, a fraction of the illumination light reflected by the glass/water interface will pass through the reflective layer and reach the camera together with any scattered light collected by the objective, which transmits through the window largely unaffected. In this way, one returns from dark-field imaging to the interferometric regime once more, with the effect of this partial reflector being to reduce the background

light intensity reaching the detector and thereby increase the interferometric contrast.[122,123] The degree of attenuation can be tailored to the incident light intensity and camera properties by simply changing the thickness of the metallic layer. The reduction in scattered light detection caused by this experimental arrangement, however, amounts to only 11.3% when using an oil immersion objective with an 8.52 mm diameter back aperture in combination with a 3.5 mm diameter partially reflective mirror (Figure 4.1c). It is interesting to note here the similarity between this concept and that of phase contrast microscopy,[31] mentioned in Chapter 2, which uses an annular mask to attenuate and introduce a specific phase delay to the (undiffracted, transmitted) reference field relative to the light that has been scattered by the sample, increasing the contrast of transparent specimens in transmitted light microscopy, and the associated implications for future work to select the phase delay introduced by the partial reflector to give optimal contrast while the sample is in focus.

4.2 Results and Discussion

4.2.1 Increased Scattering Contrast

To illustrate the effect of numerical aperture filtering on iSCAT imaging, we begin by comparing images of a cleaned microscope cover glass surface with water on top acquired with a simple iSCAT microscope[19] (Figure 4.2a,b) with the setup shown in Figure 4.1b using a partial reflector (Figure 4.2c,d), which transmits approximately 1% of the returning reflection from the cover glass. For standard iSCAT imaging, the image of a loosely focused beam (4 μm full width at half-maximum) reflecting off the surface of the cover glass appears largely featureless. Scattering contrast caused by cover glass roughness on the order of 2−4% of the total detected light intensity becomes visible only after division by a median image removing illumination inhomogeneities.[90] Use

of the spatial mask, on the other hand, enhances the scattering contrast by approximately a factor of 10 (Figure 4.2d), making it already visible in the raw camera image (Figure 4.2c). The Fourier transform properties of the lens are also illustrated by comparing Figures 4.2b and 4.2d, as the latter appears as a high-pass filtered version of the former, with the filtering performed by the spatial mask in the Fourier plane.

This increased scattering contrast has two significant consequences for the detection of single molecules. Firstly, the visibility of the surface roughness of the glass substrate in only a single raw iSCAT image simplifies the task of determining the optimal focus position for label-free iSCAT, which is best performed in the absence of any strong scatterers on an ideally defect-free surface. This is particularly important since the iSCAT signal has a strong focus dependence arising from the Gouy phase contributions to the phase difference between the reflected and scattered fields,[44,124] much stronger than a simple consideration of confocal depth would imply.

Secondly, it enables the use of cameras without the requirement for high full well capacities, achieving similar shot-noise-limited sensitivities without having to resort to large magnifications and temporal averaging, or improving the sensitivity by allowing the incident light intensity to be increased while still being able to collect the returning light without saturating the camera. A related benefit arises from the improved collection efficiencies of common CMOS sensors as compared to high full well sensors. Because cameras with high full well capacities are typically designed to work under high light conditions, they tend not to be designed for optimised light collection efficiency - the quantum efficiencies and fill factors (the fraction of the area of a pixel that is light sensitive) are typically relatively low. For an iSCAT experiment, however, although the background light is high, the number of photons scattered by a

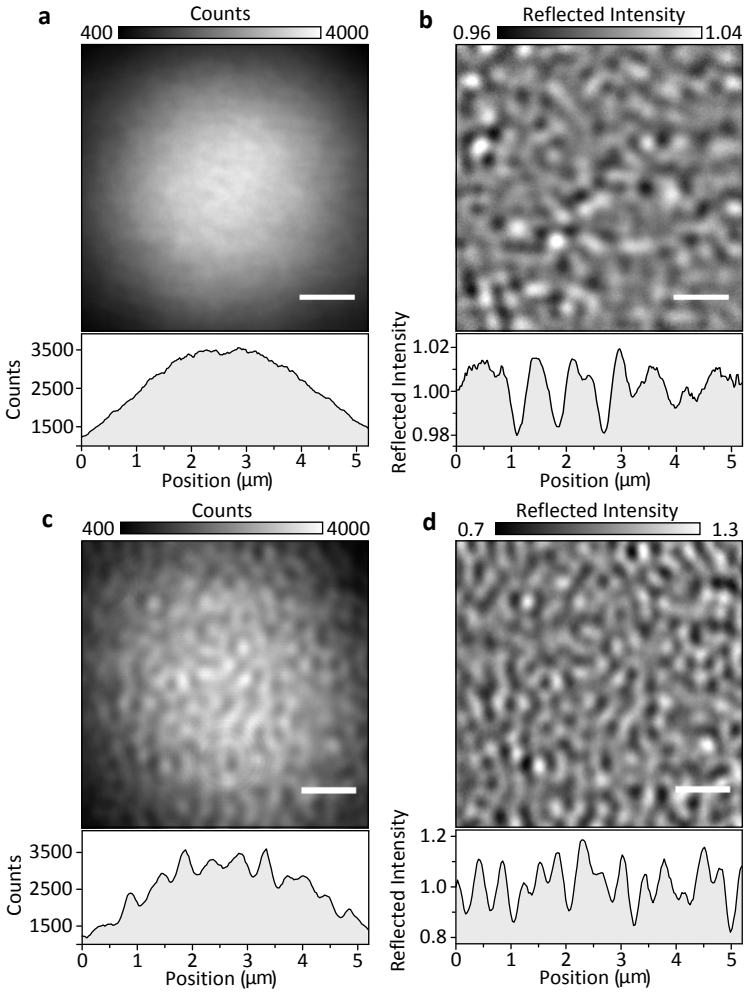


Figure 4.2: Effect of a partial reflector on iSCAT contrast. (a) Raw reflection image of a microscope cover glass covered by water using a combination of a polarising beam splitter and quarter wave plate to separate incident from reflected and scattered light. (b) The same image as in (a) after division by a median image produced while laterally translating the sample. (c, d) Equivalent images taken with the setup shown in Figure 4.1 and detailed in the Methods Section. To generate comparable images, we used a 100-fold longer exposure time for (c) compared to (a), while (a) represents the average of 100 consecutive images. In this way, the total number of incident and detected photons is identical for (a) and (c). Scale bars: 1 μm.

single molecule remains small, and so any gains in light collection efficiency result in improvements in sensitivity. To take a specific example, comparing the sensor used in this work (Sony IMX174) with the sensor typically used for previous label-free iSCAT experiments (PhotonFocus MV-D1024E-160), the combined effect of higher quantum efficiency (QE), fill factor and duty cycle results in a substantial increase in the proportion of light incident on the sensor within a 1 ms frame time that is collected. Neglecting the exact difference in fill factor (which is not specified for the Sony sensor, but is only 35% for the Photonfocus), the ∼2-fold improvement in QE and nearly 2-fold improvement in duty cycle result in a ∼4-fold improvement in light collection efficiency within a single frame.

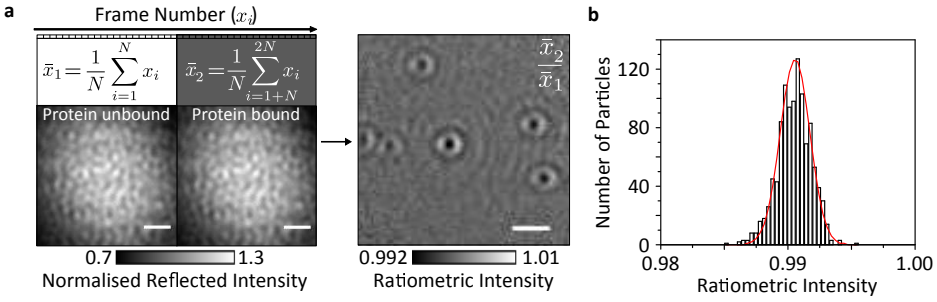


Figure 4.3: Ratiometric iSCAT imaging for detection of weak scatterers. (a) Concept of iSCAT ratiometric imaging dividing averages of consecutively recorded images, and resulting ratiometric image using N=100 revealing the binding of HSP16.5 to a bare cover glass surface. Scale bars: 1 μm. (b) Histogram of signal contrasts for 1083 events.

4.2.2 Single-molecule Sensitivity

We demonstrated the capabilities of this approach with a simple single-molecule binding assay. Images of the cover glass surface are recorded while molecules of HSP16.5 bind non-specifically to it. This is a small heat shock protein from *Methanocaldococcus janaschii* which forms a stable 24-mer with a total molecular mass of 396 kDa.[125] Raw iSCAT images separated in time are shown in Figure 4.3a, with the ratiometric image revealing the features of single

molecule binding events that occur within the averaging window of the two frames (see Section 5.1 for clarification on the use of ratiometric as opposed to differential imaging). Application of the automated analysis routine described in Chapter 5 results in a contrast histogram with an average contrast of $0.94 \pm 0.12\%$ (Figure 4.3b), almost 10 times higher than the expected contrast in the absence of the partial reflector. The error is within a factor of 2 of the expected shot-noise induced fluctuations of 0.06% in the ratiometric image, given the average counts on the camera and level of spatial and temporal averaging applied. This discrepancy may be due in part to variations in measured protein contrast as a result of local variations in reflectivity of the glass (as discussed in the Chapter 5), and in part due to the appearance of background features caused by sample drift, laser noise, and extended Airy rings of other molecular binding events.

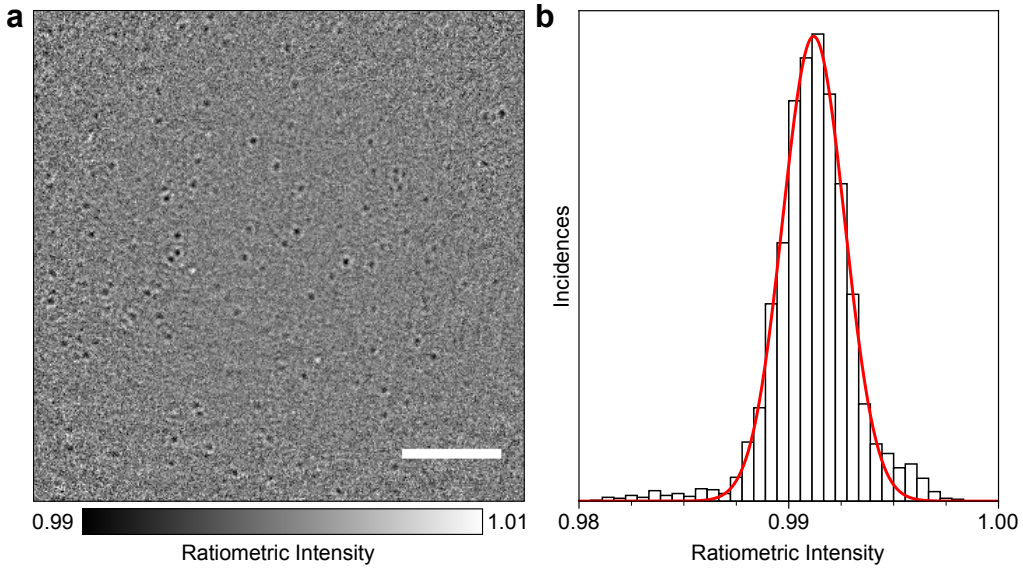


Figure 4.4: Large field-of-view single protein detection. (a) Ratiometric iSCAT image of single HSP16.5 proteins binding to microscope coverglass using the experimental setup shown in Figure 4.1 with N = 10 over a field of view of approximately 20×20 μm. Scale bar: 5μm. (b) Corresponding histogram of signal contrasts together with Gaussian fit (red line) collected from 4080 events.

In the configuration currently described, one controls the illuminated field

of view with how tightly the illumination beam is focused into the back focal plane of the microscope objective. Focusing tighter, either by expanding the beam first or by using a shorter focal length wide-field lens, results in a larger illuminated spot at the sample. This allowed us to observe many more binding events per unit time at the expense of SNR, since the input power density is lower. At a power density roughly 20 times lower than that used in Figure 4.3, the 396 kDa HSP16.5 is still readily visible over a field-of-view of 20×20 μm (Figure 4.4a). While the corresponding histogram of ratiometric contrasts (Figure 4.4b), extracted from events occurring within the central 15×15 μm, is broader than that shown in Figure 4.3b (with average contrast of $0.88 \pm 0.15\%$) and exhibits more baseline counts outwith the main Gaussian peak, the rapid collection of high statistics may be of use under circumstances where only the detection of relatively large complexes is required.

4.2.3 Effect on Larger Scatterers

It is worth reinforcing at this point that the main benefit of this approach is for weakly scattering point-like scatterers, with signals comparable to or weaker than the glass background and which otherwise require detection of large numbers of photoelectrons. We have observed, for example, that the ratio of imaging background from glass roughness to the scattering contrast of GNPs bound to the glass surface is higher than observed in previous implementations of iSCAT, likely due to the exclusion of some low-frequency components of the field scattered by GNPs. Additionally, the extended Airy rings observed for the single protein binding events in Figure 4.3 are even more prominent for more strongly scattering objects. These mostly arise due to the coherent widefield illumination, though are likely exacerbated by diffraction off the hard edge introduced into the Fourier plane by the presence of the partial

reflector. Although these fringes can be used to infer 3D information about the particle using methods similar to those used with magnetic tweezers,[70,126] for the accurate quantification of the contrast and position of multiple particles in the same image they are unhelpful.

A further illustration of the effect of the partial reflector on image formation can be seen by examining structures that are not simply point scatterers. Figure 4.5 shows a background-subtracted image of a microtubule recorded on the setup shown in Figure 4.1. Although only about 25 nm in diameter, microtubules extend well beyond the diffration limit in one dimension, and thus will not necessarily scatter preferentially into angles associated exclusively with high numerical apertures. These lower spatial frequency components will be cut by the partial reflector in the Fourier plane, possibly the cause of the particularly extended fringe pattern normal to the axis of the microtubule. Nevertheless, a substantial contrast enhancement relative to conventional iSCAT detection is still observed, albeit less than for point-like scatteres such as single protein molecules. How much of this is due to the attenuation of lower frequency components of the signal, and how much is the result of the scattered field becoming intense enough with respect to the reference field that the approximation $r \gg |s|$ (see Equation 2.3) is no longer valid and the pure scattering term in Eq. 2.1 cannot be neglected, is unclear, however.

For such strong scatterers as 20 nm GNPs or microtubules, however, this modification is somewhat redundant anyway, since a conventional iSCAT setup is more than adequate for highly precise and high speed tracking of these objects.[15,18] It is only really for the highly sensitive detection and accurate quantification of single molecules that the improvements described in this chapter are required.

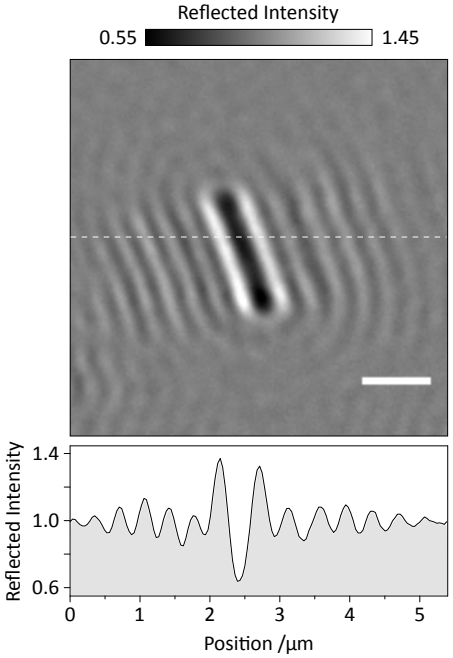


Figure 4.5: Normalised iSCAT image of a single microtubule bound non-specifically to microscope cover glass showing extended Airy rings due to wide-field illumination with coherent light. The cover glass roughness has been subtracted for clarity. Scale bar: 1 μm.

4.2.4 NA Filtering in Combination with Beam-scanning Illumination

Many of the shortcomings of this simplest of implementations can be addressed by combining the concept of numerical aperture filtering with the beam-scanning elements of the illumination approach used in previous incarnations of iSCAT (Figure 4.6a).[16,90] Achieving wide-field illumination by rapid scanning of comparatively tightly focused beam (FWHM $\sim$1 μm) reduces the prominence of the Airy rings about each point spread function by effectively reducing the spatial coherence of the illumination, since at any instant in time within the exposure of the camera only a small spot at the sample plane is illuminated. The very rapid scanning (of a 1 μm beam) achievable using acousto-optic deflectors maintains the advantages of wide-field illumination over a slow confocal scan in terms of reducing the effect of laser intensity noise

on the image, since each point in the image will be illuminated multiple times within the exposure time of the camera.

Placing the partial reflector in an image plane of the back focal plane of the objective allows direct access to that plane, which is usually located within the objective barrel, thereby optimising the attenuation of the scanned illumination beam. Additionally, having a beam that is focused at the sample plane and diverges as it propagates through the solution above, rather than a beam that is approximately collimated through the sample solution, reduces the additional background contribution from any light scattered by large species diffusing in solution above the focal plane.

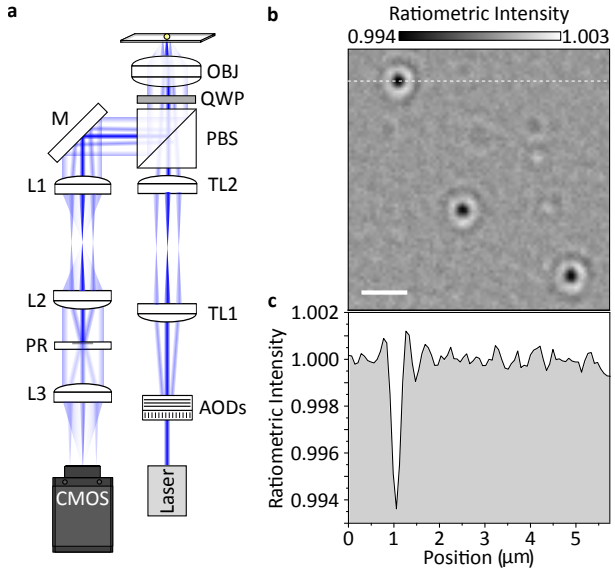


Figure 4.6: Numerical-aperture filtered iSCAT using rapid beam scanning. (a) Experimental setup based on acousto-optic (AOD) scanning of a collimated beam using a telecentric imaging setup (TL1/2). The combination of a $\lambda/4$ waveplate (QWP) and polarizing beam splitter (PBS) separates incident from scattered and reflected light. Two lenses (L1/2) create an image of the back focal plane of the microscope objective (OBJ) where the partial reflector (PR) attenuates the back-reflected beam while leaving scattered light effectively unchanged. A final lens (L3) forms an image on the CMOS camera. (b) Resulting ratiometric image using N = 150 revealing the binding of HSP16.5 to a bare cover glass surface. The weak bright features are caused by proteins unbinding from the surface. scale bar: 1 μm. (c) Image cross section from the dashed white line shown in (b).

The result of this approach is images of unlabelled proteins with extremely

high SNR (Figure 4.6b). The interference contrast is decreased slightly compared to wide-field illumination due to a modest increase in background light originating from additional reflections from inside the objective. In the case of wide-field, non-scanned illumination these can be (indeed, have to be) misaligned away from the image without compromising the PSF unacceptably. In the case of a scanned collimated beam entering the objective, however, the scanning of the angles of incidence of the illumination beam on the objective lens elements results in these back reflections forming a uniform background that does not interfere with the image formation but rather just gives a small, constant offset to all the pixel values in the image. Although undesirable per se, this slight reduction in contrast is more than offset by the suppression of additional noise sources as described above, enabling the measurement to remain shot-noise-limited to a lower level of sensitivity. In addition, the use of a collimated rather than focused beam in the objective enables the use of higher incident powers before risking damage to the objective itself, again allowing the shot noise limit to be pushed lower still.

4.3 Conclusions

The simple approach to contrast-enhanced iSCAT presented here allows facile implementation of label-free single-molecule detection on almost any inverted light microscope equipped with a digital camera and a high numerical aperture oil immersion objective lens. Coupling illumination light in and out of the imaging path can be easily miniaturised,[127] paving the way for widespread adoption not only on custom-built but also on commercial microscopes. The reduction of light intensity reaching the imaging camera enables use of essentially any digital camera, without requirement for high full well capacity or low read noise.

Even in this simple implementation without the use of beam scanning, fields of view up to at least 20×20 μm are achievable, without the interference of spurious reflections with the image. Despite the loss in shot-noise-limited SNR, such a configuration could be advantageous from a statistical point of view if all that is required is reliable detection of large complexes, for example for binding studies on a functionalised surface,[109] measuring interactions and residence times with binding partners immobilised on the surface in a single molecule analogue of surface plasmon resonance based biosensing.[128]

In addition to these simplifications, we have demonstrated that the partial reflector can be readily incorporated into a more standard iSCAT experimental arrangement. The principal advantage here is that this enables the use of higher incident powers without suffering from camera saturation or having to resort to inefficient and expensive cameras. Since the ultimate limits for iSCAT detection and imaging are defined by shot-noise-induced background fluctuations, higher incident powers automatically translate into higher detection sensitivity and precision. Although excessive increases in incident power can lead to phototoxicity and heating, these are, within reason, of little consequence for single-molecule binding assays where once the molecule is adsorbed to the surface and its interferometric contrast recorded it is no longer of interest and simply contributes to the background signal that is removed digitally. This, together with increased temporal averaging as enabled by more stable experimental setups[129] should lead to improved detection sensitivities and precision down to a few kDa s^{-1} without the need for the development of completely new camera technologies, thereby paving the way towards single-molecule mass spectrometry in solution and robust label-free single-molecule detection and imaging using iSCAT.

4.4 Methods

The setups with non-scanned illumination, as depicted in Figure 4.1 and used to acquire the data for Figures 4.2-4.5, were similar to that reported previously[19] apart from the fact that illumination light is separated from reflected and scattered light by the partially reflective mirror rather than by a beamsplitter. Briefly, the collimated output of a 2W 445 nm laser diode (Lasertack) is spatially filtered with a pinhole and loosely focused into the back focal plane of an oil immersion objective (Olympus, 1.42 NA, 60x). The beam is coupled into and out of the imaging path using the partial reflector described above, placed 2 cm from the entrance pupil of the objective. The partial reflector consists of a thin (∼80 nm) circular layer of silver of 3.5 mm diameter evaporated onto a 3 mm thick antireflection-coated glass window (Thorlabs). A 600 mm lens images the scattered and reflected light onto a CMOS camera (Point Grey, now FLIR, GS3-U3-23S6M-C) at 200× magnification, giving an effective pixel size of 29.3 nm/pixel. Although this configuration results in an elliptical mask when viewed along the optical axis of the imaging path, we found that this produced only a small effect on the PSF quality, as can be seen from a comparison of Figures 4.3a and 4.6b. Given that the PSF in such a non-scanned setup is anyway compromised by the slight misalignment of the incoming beam in order to avoid back-reflections from the various optical elements in the objective lens returning along the same path as the image, this difference was considered negligible.

The setup with scanned illumination, as depicted in Figure 4.6, was similar to that described in detail previously[90] except for the introduction of the partial reflector in an intermediate image of the back focal plane of the objective, and the use of the CMOS camera identified above. Briefly, the output of the laser diode identified above was spatially filtered and directed into a pair of

acousto-optic deflectors (AODs, AA Optoelectronic). The deflection of the beam by the AODs is imaged with a 4f telecentric lens system into the back focal plane of the objective. The combination of a polarising beam splitter and quarter-wave plate separates illumination from detection light. Another 4f telecentric lens system re-images the back focal plane of the objective onto the partial reflector. A final lens (f=750 mm) forms an image on the camera at 250× magnification, giving an effective pixel size of 23.4 nm/pixel. Using a 3.5 mm diameter partial reflector together with a 2 mm diameter collimated illumination beam provided a good compromise between confocal sectioning and background attenuation.

In both setups, we actively stabilised the focus position during measurement with an active feedback loop. A large collimated red beam (638 nm) overfilled the back aperture of the imaging objective, with those parts of the beam entering at high numerical apertures being totally internally reflected at the glass-water interface. This results in a bright ring of light returning, with the diameter of the ring depending on the objective-coverslip distance. This beam is imaged onto a camera, and the ring radius extracted and used as a measure of changes in focus position which are then corrected with a piezo attached to the sample stage.

For the landing assays, microscope cover glass (No 1.5, 24×50 mm^2 and No 1.5, 24×24 mm^2) was cleaned by rinsing sequentially with milliQ water, isopropanol, then milliQ again, before drying under a clean stream of nitrogen. Cleaned coverslips were assembled into flow chambers as described previously,[49] with double-sided sticky tape acting as a spacer between one larger and one smaller coverslip. The flow chamber was filled with 10 μl of buffer, and the sample placed in focus as determined from the features of glass roughness. The contents of the chamber were then exchanged with a dilute solution of protein,

and images were recorded as protein molecules bound non-specifically to the glass surface, with the experimental parameters for each data set given below. In all cases, the HSP16.5 monomer concentration was 240 nM.

The experimental parameters for the acquisition of the data shown in Figure 4.3 were as follows: incident power density: 45 kW/cm^2; exposure time: 1.4 ms; frame rate: 700 Hz; 2×2 pixel binning.

The experimental parameters for the acquisition of the wide field-of-view data shown in Figure 4.4 were as follows: incident power density: 2.3 kW/cm^2; exposure time: 19.9 ms; frame rate: 50 Hz; 2×2 pixel binning.

The experimental parameters for the acquisition of the beam-scanned data shown in Figure 4.6 were as follows: incident power density: 150 kW/cm^2; exposure time: 1.9 ms; frame rate: 500 Hz; 3×3 pixel binning.

Chapter 5

Mass Photometry

This chapter has been adapted from the following publication: G. Young, N. Hundt, D. Cole, A. Fineberg, J. Andrecka, A. Tyler, A. Olerinyova, A. Ansari, E. G. Marklund, M. P. Collier, S. A. Chandler, O. Tkachenko, J. Allen, M. Crispin, N. Billington, Y. Takagi, J. R. Sellers, C. Eichmann, P. Selenko, L. Frey, R. Riek, M. R. Galpin, W. B. Struwe, J. L. P. Benesch and P. Kukura, Quantitative mass imaging of single biological macro-molecules, *Science*, 360(6387), 423-427 (2018).[101] Reprinted with permission from AAAS.

5.0.1 Contributions

The setups used to acquire the data presented in this chapter were constructed by myself and Daniel Cole. The 'landing assay' data were variously taken by me, Nikolas Hundt (streptavidin/biotin binding experiments, Env/BanLec titration), Daniel Cole (the BSA data shown in Fig 5.2) and Anna Olerinyova (the Env/BanLec titration). The analysis of these data was carried out by me, including the writing of the software used. The α-synuclein data presented in Section 5.2.5 was acquired by Joanna Andrecka, and analysed by me and Joanna Andrecka. The calculation from sequence mass of protein refractive indices and specific volumes was done by Erik Marklund, and the thermodynamic modelling of the Env/BanLec equilibria was done by Martin Galpin. Smooth muscle

myosin was provided both in the native conformation and fixed in a cross-linked conformation by Neil Billington, Yasuharu Takagi and James Sellers, including negative-stain EM used to check the conformations. Additional samples were provided by, variously, Yasuharu Takagi and James Sellers (non-muscle myosin 2B), Lukas Frey and Roland Riek (lipid nanodiscs), Weston Struwe (Env and BanLec), and Cedric Eichmann and Philipp Selenko (α-synuclein).

5.1 Introduction

Biomolecular interactions and assemblies are central to a wide range of physiological and pathological processes spanning length scales from small complexes[130] to the mesoscale.[131,132] Despite considerable developments in techniques capable of providing high-resolution structural information,[133] such techniques are typically static, involve averaging over many molecules in the sample and therefore do not fully capture the diversity of structures and interactions. Such techniques as X-ray crystallography or cryo electron microscopy (cryo-EM) also place restrictions on the sample under study. The former requires the protein of interest to crystallise, while the latter typically requires samples of high purity and homogeneity (and, indeed, sample preparation is often a major bottleneck for structure determination by cryo-EM). Native mass spectrometry can provide very high resolution mass spectra for intact macromolecular complexes, but operates in the gas phase, has quite stringent requirements on the buffer conditions that can be used, and typically requires considerable time and care to find the conditions under which the complex is successfully transferred from the solution into the gas phase and intact to the detector.[134]

Solution-based ensemble methods enable dynamic studies under more native-like (and easy to prepare) conditions, but lack the resolution or separation required to distinguish different species.[135–138] Single-molecule methods offer a

means to circumvent heterogeneity in both structure and dynamics, and progress has been made in terms of characterising interactions[109] and mechanisms.[139,140] So far, however, no single-molecule approach has been capable of quantifying and following the diversity of interactions of biomolecules with the required spatiotemporal accuracy and resolution. Additionally, most single-molecule approaches make use of single molecule fluorescence, with the accompanying requirement to label the sample under interrogation.

Light scattering has the appeal of operating under native-like conditions and having universal applicability (unlike fluorescence-based approaches, which require the use of fluorescent labels). We have now established that, in an imaging configuration such as iSCAT, not only is the detection of single molecules by interferometry possible, but so too is the precise quantification of the extinction contrast measured in this way. As we saw in Chapter 2, for weak scatterers the interferometric contrast scales linearly with the scattering amplitude, which in turn is proportional to the particle volume and a function of the refactive index of the particle.[30] Considering that proteins are essentially nanoparticles made from the same 20 amino acids that do not exhibit enormous variation in refractive index[141] and specific volume,[142] and what differences there are are likely to be averaged out over the sequence of many amino acids in a chain, one might expect that the refractive indices and specific volumes of different proteins to all be approximately the same. In that case, the refractive index contribution to the scattering amplitude would be effectively constant, and the volume term approximately proportional to the mass.

To be more precise about this, a calculation based on additive contributions of the individual amino acids in a protein sequence to the specific volume and refractive index, carried out for $>10^5$ protein sequences from six species, resulted in roughly normal distributions of both refractive index and specific

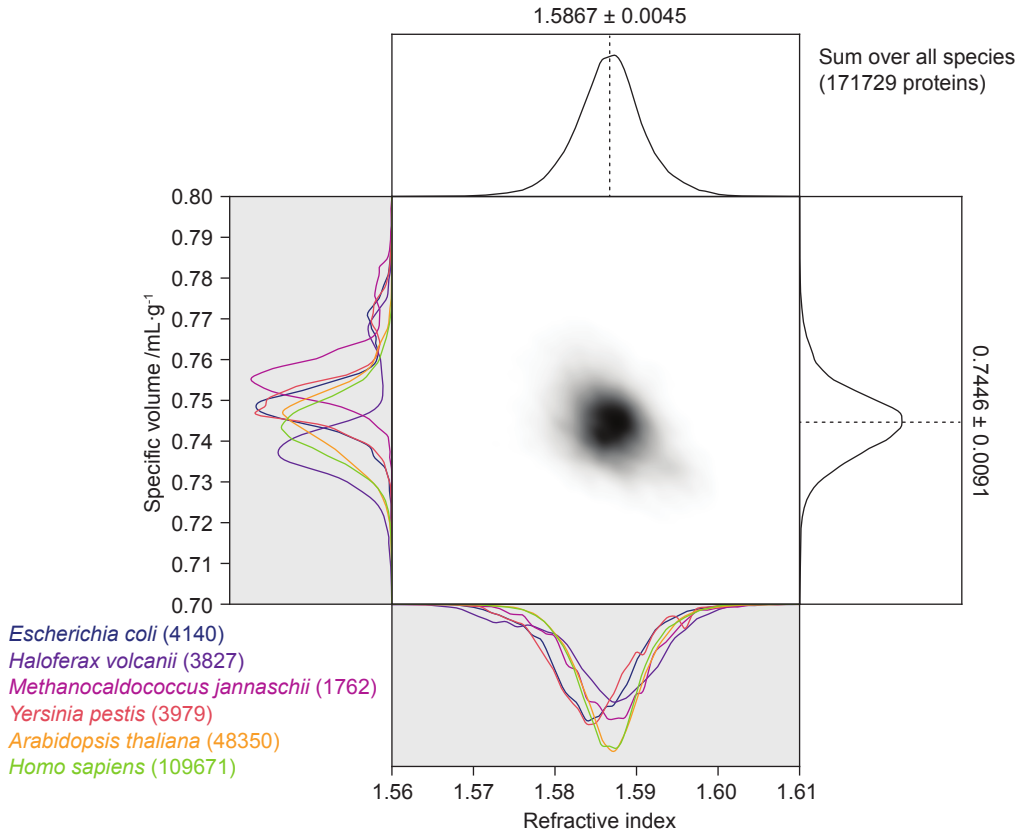


Figure 5.1: One-dimensional distributions of refractive index (top, bottom) and specific volume (left, right) for all proteins in six genomes, as calculated from the amino acid sequences, and the two-dimensional distribution of both quantities (middle). The top, right, and middle panels show the combined data from all genomes. The left and bottom panels show the respective distributions for the separate genomes, renormalised to have identical areas.

volume with standard deviations of 0.3% and 1.2% of the mean (Figure 5.1), respectively, raising the prospect of mass accuracy on the order of a few-percent when using interferometric contrast as an absolute measure of molecular mass.

This predicted linear relationship has been observed to hold at least coarsely at the single-molecule level,[19,143] and so in combination with the recently described improvements to the experimental approach and data analysis could in principle be used to achieve accurate mass measurement.

5.2 Results and Discussion

5.2.1 Validation and Characterisation

As a first demonstration of current capabilities, we recorded images of bovine serum albumin molecules (BSA, 66 kDa) as they diffused from solution to bind nonspecifically to a cleaned microscope coverslip, achieving SNRs ∼10 for the lowest contrast species. Using the automated data analysis routine described previously (Chapter 3), we extracted the scattering contrast for each individual binding event, as shown in Figure 5.2. These data revealed clearly separated signatures of different oligomeric states of BSA, with relative abundances for monomer to tetramer of 88.63, 9.94, 1.18 and 0.25% of the detected particles. The ability to separate these species by mass and to detect and quantify rare species such as BSA tetramers already begins to suggest that this approach to mass measurement is capable of characterising solution distributions of oligomeric species and molecular complexes at high dynamic range.

The approximately equal contrast spacing between the identified peaks in the BSA histogram appears to confirm the expected linear scaling between mass and interferometric contrast. Repeating these measurements for eight different proteins, spanning 53 to 803 kDa in molecular weight, further validates the linear relationship (Figure 5.3a). For each peak in the measured contrast distributions, a Gaussian fit was used to determine the peak position, and multiple repeats for each protein were measured. The mean and standard deviation of these peak centres are what are shown in Figure 5.3a as the measured contrast for a given protein and the error on that measure. A linear fit to these data points calibrates the particular setup's relationship between contrast and molecular mass, and the deviation between effective measured mass and sequence mass for these 8 proteins was <5 kDa in all cases, with an average absolute error of 1.9% of the sequence mass.

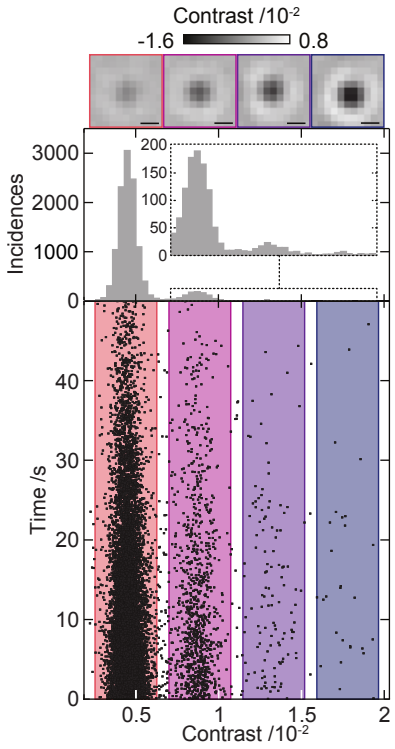


Figure 5.2: Scatter plot of n=12,209 single-molecule binding events and their scattering contrasts for BSA (bottom) and corresponding histogram . The reduction in landing rate results from a drop in BSA concentration with time (see Section 4.2.4 for further discussion). Above: representative images of single molecule binding events with contrasts typical of monomeric, dimeric, trimeric and tetrameric BSA (left to right).

There was no detectable correlation between the deviation from the linear fit and the molecular shape as quantified by the shape factor,[144] for the six species for which the shape factor could be calculated (Figure 5.4a). We further explored the possible influence of shape on molecular contrast by examining the extended and folded conformations of smooth-muscle myosin (530.6 kDa, yellow in Figure 5.3a). These conformations are adopted under different salt concentrations, which affects the interferometric contrast slightly since the refractive index of the buffer (aqueous medium) changes with salt concentration. To ensure that we measured the two different conformations, the folded conformation was cross-linked with glutaraldehyde, and then diluted in the same buffer as was used for the extended conformation immediately

before measurement. An effective mass difference of 51±22 kDa was measured between the two, which is not more than the mass increase possible through the addition of glutaraldehyde molecules used to cross-link the myosin. Although still somewhat ambiguous, there doesn't seem to be any strong dependence of interferometric contrast on molecular shape. This could be due to the small size of the molecules with respect to the wavelength of light, although it is also worth bearing in mind that strictly each molecule is measured after adsorption to a glass surface - exactly what happens to the structure of this protein after binding to the glass surface unclear, but it is not unreasonable to assume that there could well be some conformational changes.[145]

Indeed, although there appears to be little specific detail on the conformation of proteins upon adsorption to a glass surface from solution, a few general points are worthy of consideration. Adsorption of protein molecules to the glass-water interface seems to be generally thermodynamically favourable due to a lowering of the surface energy, although this interaction may be a complicated balance of electrostatic interactions with the surface, hydrophobic effects, and gains in conformational entropy if the protein can unfold (wholly or partially) upon adsorption to the surface. Exactly what happens to a particular type of protein would seem to be balance between the energetic stability of the folded structure and this gain in conformational entropy from unfolding. As such, one can perhaps refer loosely to 'hard' and 'soft' proteins.[145] 'Hard' proteins are those with high internal (structural) stability, which are likely to remain intact on the surface, and how well they adsorb be governed primarily by electrostatic considerations (e.g. highly negatively charged 'hard' proteins may not adsorb well to the typically negatively charged glass surface). 'Soft' proteins, however, are those with a lower degree of internal stability, and as such a lower penalty to unfolding. The adsorption in these cases is therefore likely to be observed

for all such proteins, driven by the gain in conformational entropy and less dependent on electrostatics.

With respect to what effect any such changes in conformation and/or folding upon surface adsorption might have on the scattering contrast, it seems likely, given the localised nature of the electrons across a polypeptide chain and the wavelength of light used, that differences in structure up to a size of $40 - 50$nm ($\sim \lambda/10$) would have little effect since the scattering is still essentially point-dipole-like. If a protein dramatically unfolds upon adsorption to the glass surface, for example, then its contour length along the surface may exceed 100 nm. This might have a number of effects upon the associated scattering contrast. Firstly, it is likely that at least along one dimension in the sample plane the extent of the scatterer will exceed the $\sim \lambda/10$ size taken as the limit corresponding to Rayleigh scattering, with the possibility of an associated change in scattering pattern. This effect is unlikely to be large, however, given this extension will be perpendicular to the optical axis, and thus the induced local oscillators at each end of the unfolded chain are still likely to have the same phase. More simply, the fact the the scattering contrast is spread over a lengthscale that begins to approach the optical resolution of the microscope could result in a slight 'smearing out' of contrast, giving a slightly broader signal and thereby readucing the contrast (per unit mass) as measured by the apparent PSF peak height. Finally, complete unfolding, and exposure of residues normally buried within the the folded structure of a protein, could result in a change in density and therefore polarisability (also, for example, of the associated electric double layer of ions in solution) that might lead to a different contrast per unit mass. It is conceivable, therefore, that some (subtle) deviation from the simple linear relationship between scattering contrast and mass could be due to extreme conformational changes of some

proteins upon adsorption, or indeed that the width of the measured distributions could be increased by a high degree of conformational heterogeneity on the glass surface, although it is difficult at this stage to assign any particular observations to these effects. It might be interesting in the future to measure an intrinsically disordered protein (or proteins with varying proportions of intrinsically disordered regions) in order to further probe these questions.

Another important parameter is the precision with which the peak centres of the measured distributions can be determined - specifically, the reproducibility of the contrast from experiment to experiment. Using the repeats of the measurements taken to calibrate the system (Figure 5.3a), this value is 1.8±0.5% (standard deviation across repeated measurements) of the sequence mass. From a purely statistical point of view, if the same distribution is indeed randomly sampled each time a measurement is taken, one would expect this to be given by $\sigma/\sqrt{N}$, in accordance with the central limit theorem, where σ is the standard deviation of the measured distribution and N is the number of particles detected. The measured values correspond to this limit for $N \approx 30$, far fewer than the actual detected number of particles per peak (typically 500-1000). This suggests that there is some systematic deviation from experiment to experiment meaning that the measured mean contrast really does vary by around 2% RMS, most probably due to errors in determining the optimal focus position at which to take a measurement.

Nevertheless, an error of 2% on a 50 kDa protein (the smallest protein measured for the calibration) suggests a precision of 1 kDa as the smallest detectable change in mass, raising the possibility of distinguishing distributions measured with and without a small-molecule bound. In order to probe this limit, we examined the biotin-streptavidin system (Figure 5.3b), which exhibits one of the strongest known non-covalent interactions with a dissociation constant

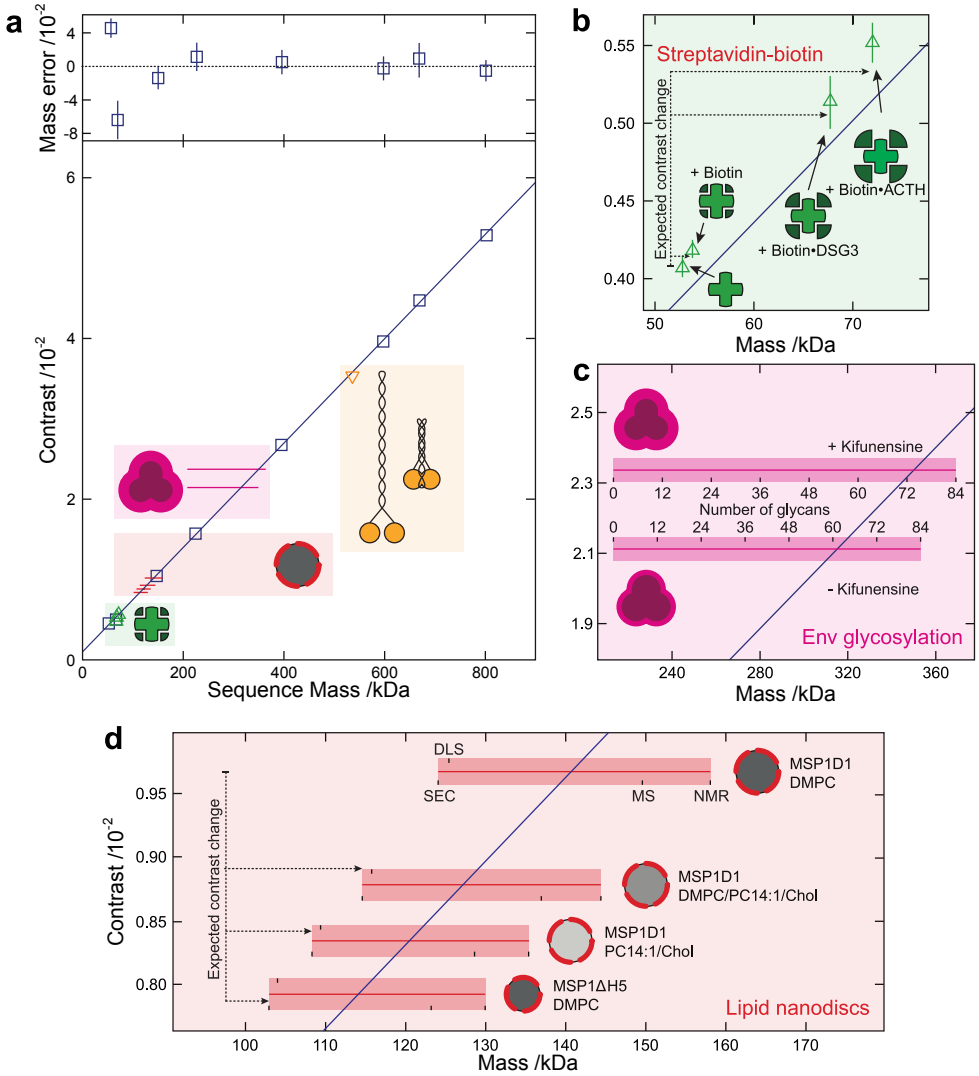


Figure 5.3: Characterisation of mass accuracy, precision, and dependence on molecular shape and identity. (a) Contrast versus molecular mass, including proteins used for mass calibration (black), characterisation of shape dependence (yellow), protein-ligand binding (green), lipid nanodiscs (red), and glycosylation (blue). Mass error (upper panel) is given as a percentage of the sequence mass relative to the given linear fit. (b) Nanodisc mass measurement for different lipid compositions and protein belts. Masses obtained by alternative methodologies for MSP1D1/DMPC are marked and extrapolated to the other compositions. The horizontal bars indicate the expected mass range as a function of characterisation technique, with the thin bars indicating the contrast measured and the thick bars representing the measurement uncertainty. For each sample, the upper text denotes the membrane scaffold protein, and the lower text indicates the lipids composition. (c) Contrast for Env expressed in the presence or absence of kifunensine and associated mass ranges expected for different glycosylation levels. (d) Detection of ligand binding in the biotin-streptavidin system. In (b, c, d) the line denotes the calibration obtained from (a). Errors are given as standard error of the mean (SEM) from repeated measurements.

on the order of 100 fM,[146] and involves the binding of up to 4 biotin molecules per streptavidin. We measured masses for streptavidin in the absence (55.7±1.1 kDa) and presence (57.4±0.9 kDa) of an excess of biotin, finding a difference of 1.7±1.4 kDa, in agreement with the expected 0.98 kDa for complete occupancy of the four binding sites. Upon addition of two different biotinylated peptides (of masses 3705.9 Da and 4767.4 Da), we found increases of 16.1±2.8 and 22.0±2.2 kDa (compared with the expected 14.8 and 19.1 kDa).

The final parameter to be characterised from these data is the mass resolution of the system, which dictates the ability to separate species of different mass by their scattering contrast. From the calibration data above, Gaussian fits to the peaks arising from single species gives not only the position but also the peak width, which we take as a measure of the mass resolution. The full width at half maximum (FWHM) exhibited a mass-dependence, increasing from 19 kDa for streptavidin (52.8 kDa) to >100 kDa for thyroglobulin (669 kDa) (Figure 5.4b). The lower end of this range corresponds to the limit expected from the photon shot noise, as calculated taking an average number of photoelectrons per pixel per frame of typically 16,000 (corresponding to half the full well capacity), accounting for the 3x3 pixel binning and 50-fold frame averaging used, to reach a value of $\sigma = 5.3 \times 10^{-4} \approx 8$ kDa for the standard deviation of the noise in the ratiometric frames (and mass-equivalent as determined from the slope of the calibration in Figure 5.3a), or FWHM∼19 kDa. The exact cause of the peak broadening with increasing mass is unclear at this stage, and will be discussed in more detail in the next chapter. These numbers nevertheless demonstrate the utility of this technique for mass measurement of proteins with homooligomeric resolution (provided the monomer is sufficiently large to be detectable).

The noise floor of this approach, as defined by the standard deviation

of background images recorded in the absence of biomolecules, decreases as expected for a shot-noise-limited process for image averaging up to several tens of ms, after which it begins to deviate with a minimum reached near 300 ms that corresponds to a mass of ∼6 kDa (Figure 5.4b). Although the noise continues to decrease after leaving the shot noise trend, it was found that best results in terms of peak width (as detailed above) were achieved while the background was still shot-noise-limited at around 50 ms integration time (that is, 50 frames of 1 ms averaged), at which point the background noise fluctuations correspond to ∼8 kDa, matching the lower limit on the mass resolution.

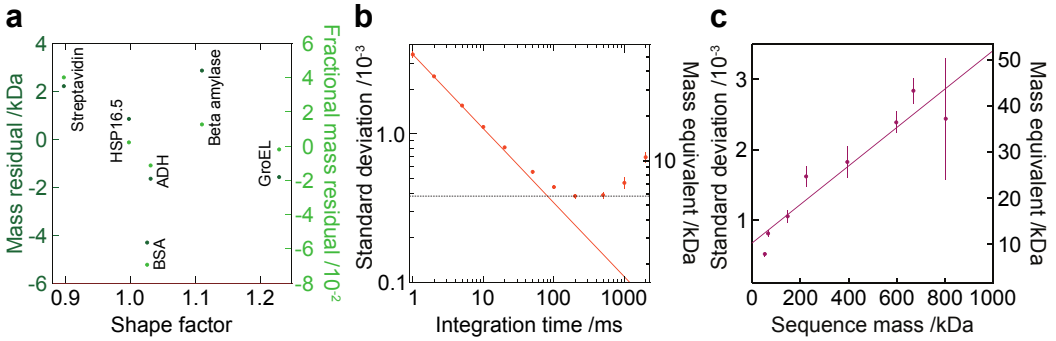


Figure 5.4: Shape-dependence, noise and resolution characterisation. (a) Absolute and fractional mass residuals as a function of molecular shape factor. (b) Standard deviation of ratiometric images as a function of integration time, for acquisition at 1000 frames/s. The dashed line indicates the nominal noise floor, and the solid line expectation based on shot noise. (c) Standard deviation of contrast histograms obtained for the 8 calibration proteins from Figure 5.3a, including a linear fit as a guide to the eye.

5.2.2 Beyond Amino Acids

Moving beyond species composed solely of amino acids, it would be interesting to probe the extent to which this approach is applicable to mixed species such as those involving proteins in complex with lipids, or glycosylated proteins. The ability to measure such species would broaden the utility of mass photometry as a bioanalytical technique, since the function of many proteins is mediated not

only through protein-protein interactions but with other classes of biomolecules or by post-translational modifications. Membrane proteins, for example, would be an area of particular interest, as they form over 50% of drug targets (as of 2006)[147] but have proven difficult to study by many conventional techniques, due to the fact that their structure and function is only maintained in a lipid bilayer (or appropriate mimetic). Glycosylation is a fairly common post-translational modification in which carbohydrate moieties are added to the protein, often providing regulatory or stabilising functions.

Earlier, we justified the link between scattering contrast and mass using the refractive indices and specific volumes of the different amino acids averaged over the length of a polypeptide chain. Although this clearly is not valid for species not composed of amino acids, the scattering signal is ultimately governed by the polarisibility of the molecule. Since these other biomolecules are still mostly made of covalently linked carbon and other atoms from the first row of the p-block elements, one might imagine the polarisibility of the electrons in the molecule to be broadly similar across proteins, carbohydrates and lipids, at least within the error of this measurement. Thus, although we do not have rigourous justification for assuming the conversion from contrast to mass will be the same for these other classes of biomolecules as for proteins, it seems reasonable to make a crude approximation of similarity for now.

Lipid nanodiscs have been developed over recent years as a method for studying membrane proteins in an environment that is both native-like (that is, in the presence of a planar lipid bilayer) and also compatible with standard aqueous solution-based techniques.[148] Consisting of a patch of a planar lipid bilayer (on the order of 10 nm in diameter) encircled by a pair of amphiphilic membrane scaffold proteins (MSPs), they were adapted from biological lipoprotein particles by engineering different versions of apolipoprotein A-1 to favour

the formation of discoidal particles, and have been demonstrated to have substantial flexibility in terms of lipid content and size of the disk as controlled by the length of the MSP.[149,150] This flexibility makes them ideal test systems for determining the applicability of mass photometry to mixed protein-lipid systems.

For simplicity, we only considered lipid nanodiscs without any membrane proteins embedded. We first measured the well-studied disc consisting of the MSP1D1 belt protein and DMPC (1,2-dimyristoyl-*sn*-glycero-3-phosphcholine), obtaining a mass of 141.0±1.6 kDa (Figure 5.3d), in good agreement with the range of masses spanning 124 to 158 kDa reported from other methods (including size exclusion chromatography, dynamic light scattering, native mass spectrometry, and NMR measurements of the rotational correlation time).[150,151] Replacing MSP1D1 with the smaller MSP1ΔH5 reduces the nanodisc diameter and therefore lipid content by ∼20%, after accounting for the thickness of the belt protein.[152] Given the masses of MSP1D1 and MSP1ΔH5 are 47 and 42 kDa respectively, we can predict a mass for the MSP1ΔH5 nanodisc of 113.6 kDa (based on the mass measured by this technique), again in good agreement with the measured value of 114.1±1.9 kDa.

Rather than changing the length of the belt protein, the introduction of partially unsaturated lipids (in this case, 1,2-dimyristoleoyl-*sn*-glycero-3-phosphocholine, PC14:1) and cholesterol to the MSP1D1 nanodisc reduces the mass by changing how tightly the lipids in the bilayer can pack. From the lipid composition, masses, and protein:lipid assembly ratios used, an MSP1D1 nanodisc with 40% DMPC, 50% PC14:1 and 10% cholesterol is predicted to have a mass of 129.4 kDa, while one consisting of 90% PC14:1 and 10% cholesterol is predicted to be 121.9 kDa. Once again, the masses measured through the scattering contrast (127.3 and 120.6 kDa, respectively) are in

agreement with these expectations. Further details of these calculations of the predicted masses are given in the Methods section at the end of this chapter.

We also tested the applicability of this method to solvent-exposed glycans, selecting the HIV envelope glycoprotein complex (Env), which is a trimer of gp41-gp120 heterodimers, as a test system. Env is extensively *N*-glycosylated, with carbohydrates contributing almost half its mass.[153] For an Env trimer mimic expressed in the presence of kifunensine, a mannosidase inhibitor that leads predominantly to unprocessed $Man_9GlcNAc_2$ glycans (Man, mannose; GlcNAc, N-acetylglucosamine), we recorded a mass of 350.0±5.7 kDa. Making the crude approximation that glycans and amino acids have similar polarisabilities, this corresponds to a glycan occupancy of 74±3 out of 84 possible sites (Figure 5.3c), consistent with recent observations of high occupancy for gp120 expressed with kifunensine.[154] For Env expressed without kifunensine, we recorded a lower mass of 315.3±10.5 kDa. The mass difference can be attributed only in part to the lower average mass of the processed glycans, and yields a total *N*-glycan occupancy of 61±6. Although the exact value for occupancy are beholden to our calibration (in particular, how valid that is for glycans as well as proteins), the presence of unoccupied sites is consistent with their observation in proteomics data.[155]

5.2.3 Quantifying Protein-Protein Interactions

Having established the capabilities of iSCAT-based mass photometry, we sought to test it on more complex systems that are difficult to assess quantitatively with existing techniques as a consequence of heterogeneity and multistep assembly mechanisms. The biotin-streptavidin system described above exhibits nearly covalent binding, raising the question of whether weaker equilibria, as are often encountered for protein-protein interactions, can be quantified in this way.

We therefore investigated the interaction of Env with the antiviral lectin BanLec, which neutralises HIV by binding to surface *N*-glycans through a mechanism that has proven difficult to measure by conventional biochemical approaches.[156,157] We were able to monitor the interactions and short-lived complexes before aggregation that arose as BanLec was titrated into a solution of Env (Figure 5.5). The addition of BanLec resulted in a reduction in the amount of single Env units detected coupled to the appearance of dimers and higher-order assemblies. One can immediately see from these distributions that BanLec binding results in cross-linking of multiple Env units, rather than the lectins simply coating individual Env units. Notably, the positions of the resolved peaks enabled us to quantify the number of BanLecs bound per dimer (one to two), trimer (two to three) and tetramer (three to four), demonstrating bivalent binding. Although the highest BanLec concentration shown here is 40 nM, measurements were taken at up to 100 nM, though these proved intractable to the data analysis approach used because, rather than observing diffraction-limited spots binding to the glass surface, we observed very large (>1μm) aggregates diffusing relatively slowly through the solution and giving rise to a large amount of background scattering in the movies. While this prevents quantitative analysis and extraction of mass distributions through this approach, it nevertheless provides qualitative evidence that at such concentrations essentially all Env monomers have gone into large aggregates bound together by BanLec.

The mass resolution here enabled us to follow the evolution of specific oligomeric populations as a function of BanLec concentration (Figure 5.5b). Describing this with a simple model (depicted in Figure 5.5b, and described in detail in the Methods section), enabled us to extract the underlying association constants ($K_{BanLec} = 0.12$ nM^{-1}; $K_{Env} = 8$ nM^{-1}; $K'_{BanLec} = 0.4$ nM^{-1}; all as

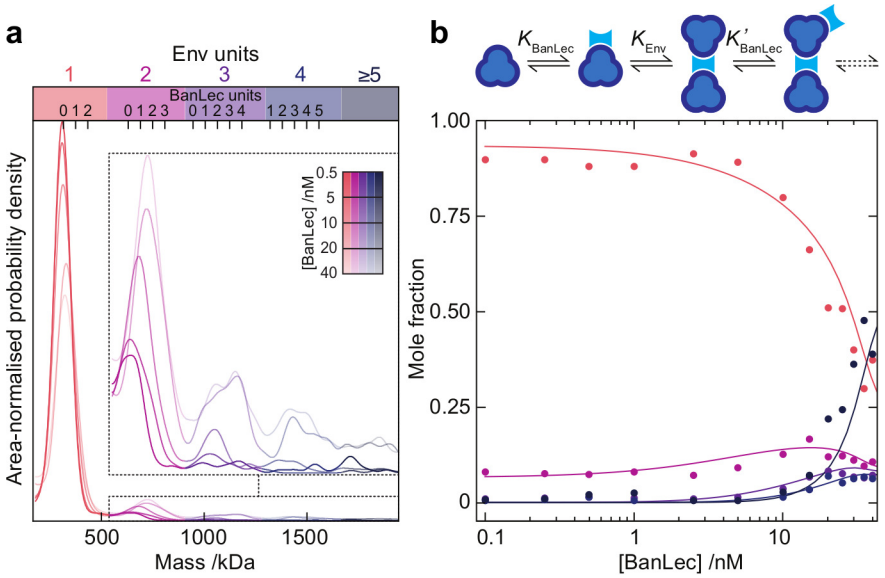


Figure 5.5: Single-molecule mass analysis of heterogeneous protein assembly. (A) Mass distributions for Env in the presence of 0.5 to 40 nM BanLec monomer, alongside expected positions for multiples of bound BanLec tetramers. Inset, a zoomed-in view of the region for larger species. (B) Oligomeric fractions colored according to (A) versus BanLec concentration, including predictions (curves) using the model shown.

defined in Figure 5.5b), in agreement with recent bulk studies ($K_{BanLec} = 0.19$ nM^{-1}) which also found signatures of a secondary binding event (2.85 nM^{-1}).[158] The key result here is that the binding of Env to BanLec that is already bound to Env (K_{Env}) is much stronger than that to free BanLec (K_{BanLec} or K'_{BanLec}), clearly indicating coorperativity between the two binding sites of the lectin.

5.2.4 Surface vs Solution Distributions

One remaining question hovers around this approach to determining biomolecular mass distributions in solution, and concerns the role played by the glass surface. In the landing assays performed here, we detect individual molecules binding to the cover glass surface, rather than directly in solution. As a result, variations in surface affinities and/or collision rates could in principle lead to a deviation of the surface-measured distribution from the true solution distribution. We can, however, extract binding rates directly from our experi-

mental data. Here, we have employed standard flow cells[49] that exhibit large surface-to-volume ratios. As a result, binding to the surface reduces the analyte concentration throughout the experiment, as can be seen in Figure 5.2. We remark that this decay in binding frequency cannot be attributed to surface saturation because: (a) we can add more sample to a flow chamber a few times and still observe binding, (b) for a $4 \times 9\mu\text{m}^2$ field of view, a tightly packed monolayer of 5 nm diameter particles would contain $\sim 1.8 \times 10^6$ particles, while we typically measure 10^3 binding events in an experiment, and (c) the lack of unbinding (e.g. from the data set in which 12,209 binding events of BSA were collected for Figure 5.2, only 372 unbinding events were observed) implies that we deplete the concentration in solution with time. The measured drop in binding frequency is well described by an exponential decay, consistent with a simple first-order process of protein molecules in solution binding irreversibly to the glass surface with a a given rate constant (Figure 5.6a), not an unreasonable model for most proteins on a glass surface.[145] Fitting of these binding time distributions to a single exponential model thus provides representative decay constants for a given species from multiple movies (Figure 5.6b). Because we have sufficient mass resolution to distinguish different oligomeric states, we can characterise the decay in binding rate for each oligomeric state (Figure 5.6c), measuring a rate constant that is a function of the probability that a collision with the surface results in an adsorption event and the collision rate, which in turn is proportional to the diffusion coefficient.

The values of these rate constants for different oligomers and different species studied here exhibit variations of less than $\pm 25\%$ from the mean decay for all oligomeric species per protein (Figure 5.6c). For BSA, Env, smooth-muscle myosin and GroEL we observe a decrease in decay rate with molecular weight. For systems where we observe decay of a native, globular oligomeric

structure into smaller subunits (alcohol dehydrogenase, β-amylase) the pattern is inverted. Most importantly, however, the decay rates are highly reproducible with narrow standard deviations, demonstrating that they can be characterised with high accuracy on a an oligomer-to-oligomer basis. Overall, we found good correlation between the absolute rate constant and the (molecular weight)$^{-1/3}$, i.e. the scaling of the diffusion coefficient with mass assuming spherical objects, suggesting that the surface affinity for different oligomeric states, and indeed to quite some extent different proteins, does not vary significantly (Figure 5.6d).

To probe the effect of differences in diffusion and surface attachment on oligomeric distributions and the resulting thermodynamic parameters, we can apply a correction to the counted number of each oligomer depending on the measured binding rate constant. Assuming that any change in the equilibrium as a result of this dilution is slow compared to the timescale of the experiment, and thus the dominant process occurring in solution is the irreversible sticking of molecules to the coverslip surface, then to accurately count the proportion of each oligomer present in solution one would have to integrate over the exponential decay in binding events from the addition of sample (time, $t = 0$) until all binding has ceased. Experimentally, meanwhile, we effectively integrate from some time, $t_0 \approx 15s$ after addition of sample up to a later time, t_f, when the acquired movie ends. We can relate these two via

$$N_i = M_i \frac{e^{k_i t_0}}{1 - e^{-k_i(t_f - t_0)}} \tag{5.1}$$

where N_i is the number of particles of oligomer i counted over the full integral, M_i is the number measured experimentally, and k_i is the binding rate constant for oligomer i.

As shown for BSA (Figure 5.6e) corrections produce small but noticeable corrections to the mass distributions. While one might naively assume that

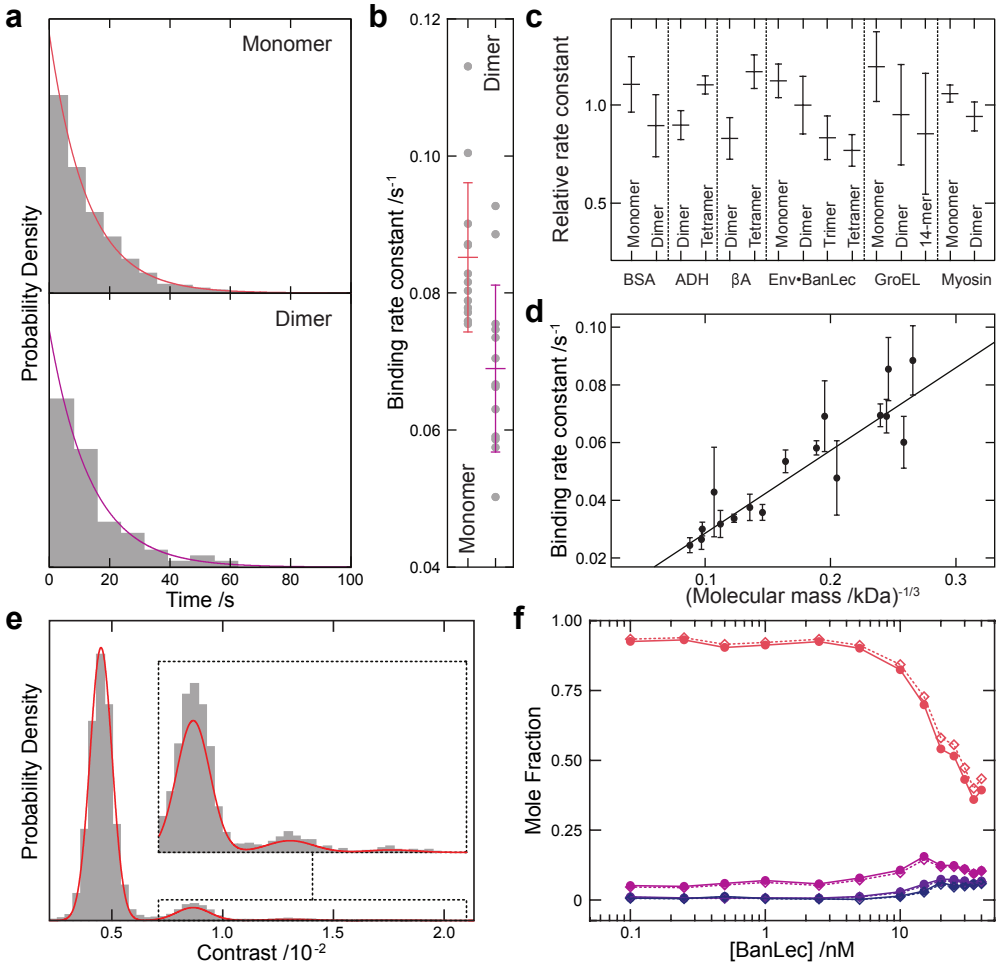


Figure 5.6: Solution vs surface mass distributions. (a) Changes in binding time distributions for BSA monomers and dimers from the same data as shown in Figure 5.2 and corresponding exponential fits. (b) Resulting binding rate constants for 11 different movies. (c) Binding constants for a variety of proteins exhibiting more than one oligomeric state studied in this work, normalised to the average binding constant for each protein. (d) Plot of binding constant vs (molecular weight)$^{-1/3}$, except for those exhibiting inverted behavior but including protein samples exhibiting only a single oligomeric state as well as those in C, together with a linear fit describing the behavior expected from diffusion scaling. (e) BSA mass distribution before (solid bars) and after (red line) scaling for mass-dependent diffusion. (e) Env-BanLec oligomeric evolution before (solid) and after (dashed) correction for surface effects.

the correction should lead to an increase in the dimer fraction because of compensation for diffusion, we find the opposite to be true. This is caused by the fact that we have to take into account the delay (t_0) between addition of sample and observation of binding events, which is usually on the order of 15 s. During this time, a higher proportion of the smaller oligomers are lost to the surface, which leads to the observed correction factor. We observe similar effects for our Env-BanLec experiments (Figure 5.6f), where the correction causes changes in the mole fractions that are within the error associated with our ability to model the experimental data.

Of course, this is subject to the assumption that system does not significantly respond to the drop in concentration over the $\sim$ 1 minute of measurement time (or over the $\sim$30 s $1/e$ time, estimating from the binding rate constants for the larger complexes in Figure 5.6d). The data itself does provide some level of a check here, though, for if there were another process (e.g. loss of subunits from a higher-order oligomer) then this ought to be reflected in the decay of binding rate over time, which might exhibit a double-exponential profile, for example. Depending on how rapid the change in the oligomeric distribution of such a system is, one might then have to attempt to minimise the time between sample addition and the start of measurement and take only those events occurring within the first portion of the acquired movie.

This also has implications for how the experiments are carried out. Provided the above assumption holds, the oligomeric distributions can be corrected only if the time between the addition of sample and start of acquisition is known (although testing different values of t_0 from 5 to 30 s did not produce wild variation in the adjusted distributions), and so it is important to record this time interval while taking a measurement. Since there is also some error in the definition of time zero in this case (as it takes a certain amount of time

to manually load the sample into the flow chamber), improvements to (or automation of) the sample delivery method should further improve the ability to quantify this time delay.

5.2.5 Imaging Mass Photometry

A particular advantage of an imaging-based approach is its ability to time-resolve mass changes in a position- and local concentration-sensitive manner. This enables us to examine surface-catalysed nucleation events that may eventually lead to amyloid formation.[159] Previous studies using fluorescence labelling found aggregates of ∼0.6 μm in diameter within a minute of addition of the amyloidogenic protein α-synuclein at 10 μm to an appropriately charged bilayer.[160]

Upon adding α-synuclein to a planar, negatively-charged DOPC (1,2-dioleoyl-*sn*-glycero-3-phosphocholine)/DOPS (1,2-dioleoyl-*sn*-glycero-3-phospho-L-serine) (3:1) supported lipid bilayer (SLB) at physiological pH, we observed the appearance and growth of nanoscopic objects within seconds, even at low micromolar concentrations (Figure 5.7a). The dark spots in the images are assigned to be the aggregates, while the additional features in the background arise from sample drift. It is worth noting that the ratiometric imaging approach used here is different than for the landing assays described earlier - in order to monitor the cumulative addition of material to the aggregates the background is generated by taking the average of a few frames before the addition of protein to the bilayer, and all subsequent images divided by this background (as opposed to updating the background to always be from the immediately preceding frames, thereby only looking at instantaneous additions), making the later images more susceptible to sample drift.

The combination of the low molecular mass of α-synuclein (14 kDa), which

is below the detection limit even under ideal experimental conditions as used in the 'landing assays', and perturbation to the images caused by the addition of sample (delivered by the fusion of a droplet of protein solution to a droplet of buffer above the SLB) meant that we could not determine the sizes of the initial nucleating species. We could, however, monitor, the nanoscale formation of associated structures in the range of hundreds of kilodaltons (Figure 5.7b), although not with single-subunit sensitivity, again owing to the small size of α-synuclein monomers. The growth of these clusters was rather uniform across the field of view, with the contrast of the spots increasing relatively rapidly at first and then slowing down. This could be an effect of growth upwards from the membrane rather than, or in addition to, the actual rate of growth decreasing, because after a few tens of seconds it was apparent from the images that there were larger, apparently tubular, structures having grown up from the membrane fluctuating in solution (while still being attached at one end). Given the interferometric nature of the technique, the contrast is very sensitive to the optical path difference between the principal reflection from the glass surface and the light scattered by the objects, and so protein adding even a short distance above the bilayer surface may well result in substantially lower contrast than the same amount of protein adding at the surface. Consequently, we quantified only the initial stages of the growth of these aggregates, fitting a straight line to the region where the contrast increase over time appeared linear, and converting the rate of increasing contrast to a rate of mass addition to give an initial growth rate for each aggregate. Repeating this for various concentrations of α-synuclein, the initial rates followed expectations for a first-order process (Figure 5.7c).

Although in principle the presence of the SLB results in a different refractive index environment for scatterers close to the surface, and possibly therefore a

different contrast-to-mass conversion as compared to the 'landing assays' on bare glass, we did not notice a substantial difference in terms of the contrast (or, indeed, reflected intensity) of the glass background. We therefore assumed a similar calibration for species on the bilayer as for those binding directly to the glass when converting rates of increasing contrast to rates of mass addition. One could be more accurate here by calibrating for the bilayer environment, for example by addition of membrane binding proteins of known molecular weight to the bilayer, and extracting the contrast as a function of molecular weight, as was done for proteins on glass.

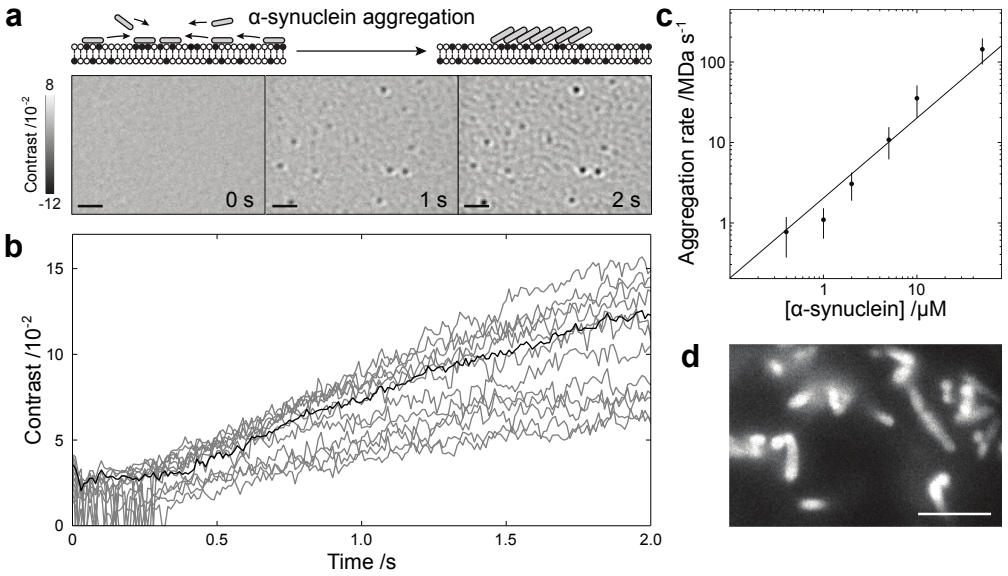


Figure 5.7: Imaging of α-synuclein aggregation on a supported lipid bilayer. (a) Schematic and iSCAT images of α-synuclein (1 μM) aggregation on a negatively charged bilayer. Scale bar: 1 μm. (b) Individual (grey) and average (black) growth trajectories for 12 particles from (a). (c) Initial growth rate vs α-synuclein concentration, shown with the best fit assuming first-order kinetics. Error bars denote SEM from different particles. (d) Fluorescence image after thioflavin-T staining of a bilayer-catalysed aggregation assay at 10 μM after overnight incubation. Scale bar: 5 μm.

A couple of control experiments are necessary to check how likely it is that these observations are related to the early stages of amyloid assembly. We repeated the assay on DOPC-only bilayers with neutral charge, and did not

observe anything happening upon α-synuclein addition. Further, we incubated our assay overnight[159] before testing for the presence of amyloid with thioflavin T, a dye which shows enhanced fluorescence upon binding to structures rich in beta sheets such as amyloids.[161,162] Fluorescence images of our assay after addition of ThT clearly showed the presence of ThT-positive aggregates (Figure 5.7d).

In addition to the growth of these large aggregates, we also observed the presence, after addition of α-synuclein, of much smaller mobile species, also on the bilayer but diffusing rapidly across it. The signal magnitude of these objects corresponded approximately to that of 400 kDa of protein, although further work is needed to characterise them in detail, as simply from a scattering image it is not even clear what they are formed of.

5.3 Conclusions

In this chapter we have demonstrated that precise measurement of the interferometric scattering contrast of individual biomolecules on a light microscope provides a route to accurate measurement of biomolecular mass distributions in solution with physiologically relevant buffer conditions (e.g. pH, salt concentration, etc.), an approach we have termed mass photometry. The mass accuracy, as determined by the deviation from a linear correlation between sequence mass and measured mass for the calibration proteins was <5 kDa and exhibited no clear correlation with molecular shape. The resolution, defined by the FWHM of the peak, reached values as low as 19 kDa at the lower end of the mass range explored here, though increasing with increasing mass for reasons as yet unexplored.

The reproducibility of the peak position from experiment to experiment was limited to $\sim$2% of the mass, sufficient to detect the difference between a

population of streptavidin with 4 biotins bound as opposed to without. These results, at the lower limit of what is currently measurable in terms of mass shifts, demonstrate that strong binding of kDa-sized ligands is in principle detectable. Given the SNR on such a small shift (i.e. SNR $\approx$ 1 for a l kDa shift on a 50 kDa protein), however, detailed measurements of interaction strengths in terms of measuring dissociation constants for such small ligands may be beyond the current capabilities of iSCAT-based mass photometry. Nevertheless, there is already some scope for solution-based studies involving mass additions in the few-kDa range, such as ubiquitination.[163]

We probed the question of whether measuring adsorption of molecules to a glass surface (rather than strictly in solution) influences the measured mass distributions by analysing the binding rates of different proteins, and different oligomers of the same protein, to this surface. The observation of exponential decays in binding rates together with a simple model invoking irreversible binding to the coverslip led us to the conclusion that differences in non-specific binding rates to microscope cover-glass only weakly influences the oligomeric distributions measured by mass photometry, suggesting that our measurements are indeed representative of solution distributions. While it is conceivable that molecules with very different surface properties may exhibit behaviour that deviates further from the trend based on diffusion coefficient, the surface-measured distributions can be corrected through direct measurement of the binding rate constant of each species to the glass surface. In this way, the glass surface can in most cases be thought of as simply acting as a detector for species in solution.

The ability to measure water-soluble assemblies of lipids and proteins was also demonstrated through the use of lipid nanodiscs. Although these measurements strictly only confirmed the scaling of the iSCAT signal with

lipid content relative to the reference nanodisc (with MSP1D1 belt protein and only DMPC lipid) rather than demonstrating absolute mass measurement of lipid content to the same accuracy as the protein standards, these results are still promising for the applicability of mass photometry to measure membrane protein interactions. That there is a broad range of masses determined by other techniques for the same sample is indicative of the fact that well-defined mass standards of lipid assemblies are difficult to come by anyway, and the general agreement of the masses measured assuming the same calibration line as for proteins with these other measurements is encouraging. Importantly, with such systems measurement of an accurate absolute mass for the number of lipids is not necessarily the most enticing prospect, but rather the fact that it is possible to measure a well-defined mass for these systems opens up the possibility of measuring nanodiscs with membrane proteins incorporated,[148] and thus the prospect of interaction studies with binding partners. Given the relevance of membrane proteins as drug targets, this is an exciting avenue for future exploration.

Along similar lines, the results of the Env-BanLec system show the ability of mass photometry to probe the detailed mechanism and thermodynamics of relatively complex interactions involving species covering a broad mass range and the capacity to bind multiple units. These results are directly relevant to the characterisation and optimisation of antiretrovirals, given that multivalency and aggregation have been proposed to be linked to neutralisation potency.[158] We anticipate similar quantitative insights to be achievable for other therapeutic target proteins and protein-protein interactions in general.

In pursuit of broadening the applicability of this technique further, combining mass photometry with established surface modifications[164] may be a vital area of exploration. Passivation decreases surface binding probabilities and

therefore should provide access to much higher analyte concentrations (greater than micromolar), and surface activation will reduce measurement times at lower concentrations (unless the surface binding rate is already diffusion-limited). Specific functionalisation and immobilisation of individual subunits of binding partners could allow for the determination of on and off rates, in addition to equilibrium constants, and enable targeted detection in the presence of other analytes.[19,109] Further, integration with existing microfluidic solutions for in situ diffusional separation of complex mixtures or mixing of different solutions could broaden the scope of the systems to which mass photometry may be applied to more complex mixtures that might otherwise give rise to excessive scattering background or to rapidly interacting particles.[165,166]

5.4 Methods

The optical setup used for these measurements was as shown in Figure 3.2, and described both in Chapter 3 and in the Methods section of the Chapter 4. The one difference unspecified there is that all elements were mounted onto a $400\times600\times50$ mm^3 aluminium plate and enclosed with 40 mm thick aluminium plate in order to minimise the effect of external perturbations. The entire block was additionally rested on four wheelbarrow inner tubes for vibration isolation.

A few additional considerations assisted the stability of the sample relative to the microscope. Firstly, rather than the usual 3D stage for mounting and positioning the sample, we used a 1D stage that only allowed motion along the optical axis. Since for these experiments it is not crucial to be able to search for particular features (any clean patch of glass surface will act as the sensor surface to which proteins can bind), the additional two degrees of freedom were unnecessary and simply another source of sample drift. Secondly, magnets were used to fix the coverslip in place on the sample holder, reducing the effect of

the slow relaxation/flow of the viscous immersion oil that can also give rise to sample drift. Finally, the area around the sample mount was enclosed with a polystyrene box to exclude air currents that perturbed the sample position.

Landing assays were performed using flow chambers prepared as described in the previous chapter. The flow chamber was loaded with buffer, and the surface of the coverslip brought into focus. The contents of the flow chamber were then exchanged with the sample solution, typically at concentrations of around 10 nM of the species of interest. Unless otherwise stated, the buffer used was 20 mM Tris-HCl, 100 mM NaCl, pH 7.4. For systems with specific buffer requirements, the system was recalibrated using that buffer since the salt concentration affects the refractive index of the solution and therefore the scattering contrast.

For the landing assays, the camera was run close to the highest achievable frame rate for the given field of view, typically 1 kHz at 4×9 μm^2. Images were pixel-binned 3×3 and time-averaged 10-fold prior to saving, giving a final pixel size of 70.2 nm and effective frame rate of 100 Hz, substantially reducing the file size of the saved data, and therefore also the time required for analysis. Average power density at the sample varied somewhat between the different experiments, between 280 and 860 kW/cm^2.

Single molecule binding events in the acquired movies were identified and quantified using the same analysis routine as in the previous chapter, an approach which is described in detail in the next chapter. The resulting contrast distributions were fit to a Gaussian function (or the sum of multiple Gaussians, if more than one peak was discernible) using MEMLET.[167] This returned centre positions for the peak, which was taken as the contrast determined for that species in that movie, and widths of the distribution as reported in the discussion of mass resolution. Each movie was analysed separately, and the

values for measured contrast are reported as the mean±standard deviation of these numbers across multiple independent movies recorded for each sample.

The calibration proteins streptavidin, BSA, alcohol dehydrogenase, β-amylase, thyroglobulin and GroEL were purchased from Sigma-Aldrich. Non-muscle myosin 2B was provided by Yasuharu Takagi and James Sellers, purified as described previously except for the addition of a halo-tag.[168] All calibrants were measured at concentrations 5-10 nM. For the streptavidin-biotin binding experiments, D-biotin was purchased from Sigma-Aldrich. Two synthetic N-terminally biotinylated peptides based on the sequences of desmoglein-3 (DSG3, biotin-EWVKFAKPCREGEDNSKRNPIAKITSDYQA) and adrenocorticotropic hormone (ACTH, biotin-SYSMEHFRWGKPVGKKRRPVKVYPNG AEDESAEAFPLEF) were purchased from Cambridge Research Biochemicals.

Smooth-muscle myosin was also provided by Yasuharu Takagi and James Sellers, purified as described previously.[169] The folded conformation (10S) was induced by incubation at 200 nM in ATP-containing buffer (10 mM MOPS, 150 mM NaCl, 1 mM $MgCl_2$, 0.1 mM EGTA, O.1 mM ATP, pH 7.0). Glutaraldehyde was added to a concentration of 0.1% (v/v) and incubated for 1 min. The reaction was stopped by addition of Tris-HCl (pH 8.0) to a final concentration of 100 mM. For the mass photometry experiments, both native (6S) and cross-linked (10S) conformations were diluted in in buffer containing 10 mM MOPS, 500 mM NaCl, 1 mM $MgCl_2$, 0.1 mM EGTA, pH 7.0 to a concentration of 5 nM and kept on ice until use.

Lipid nanodiscs were provided by Lukas Frey and Roland Riek, purified as described previously.[170] For comparison with expected masses for each sample, we took literature values (Table 4.1)[150,151] for the mass of the MSP1D1 nanodisc with DMPC lipid, which we took as a reference, as measured by a variety of techniques to provide a range of expected masses. For each of these, including

our own, we calculated an expected mass for the MSP1ΔH5 nanodisc with DMPC. This was done by subtracting the mass of the protein component and scaling the resulting mass of lipid by the reduction in area of the bilayer patch calculated from the square of the reduction in diameter of the nanodisc as measured by size exclusion chromatography (SEC), dynamic light scattering (DLS) and electron microscopy (EM).[150] The expected mass of the nanodisc follows by addition of the MSP1ΔH5 protein mass (Tables 4.2 and 4.1)

Compositions and protein:lipid assembly ratios for the MSP1D1 nanodiscs with varying lipid composition are given in Table 4.3. As above, we calculated a range of expected masses from the various reported measurements of the reference nanodisc. We scaled the measured lipid mass according to the expected changes due to different total number of lipid molecules pre nanodisc (from the protein:lipid assembly ratio) and different average mass per lipid molecule. Again, addition of the mass of protein leads to the expected masses of the nanodiscs (Tables 4.4 and 4.5).

Env SOSIP (BG505) and BanLec were provided by Weston Struwe, prepared as described previously either in the presence or absence of kifunensine.[171] All measurements on Env were carried out in phosphate buffered saline (PBS). For the kifunensine-treated and wildtype Env alone, the concentration at measurement was 5 nM.

For the interaction studies between Env and BanLec, Env was diluted to 20 nM and BanLec to twice the working concentration. The protein dilutions were kept on ice until use. Env was mixed 1:1 with either PBS (as a control) or BanLec (resulting in a measurement concentration of 10 nM of Env) and incubated at 5 min at room temperature before measurement as described above. The kernel density estimates shown in Fig 4.5a were generated using a Gaussian kernel with bandwidth of 30 kDa. The number of each observed

Env cluster was determined by counting the events within resolvable contrast intervals, i.e. monomers, dimers, trimers, tetramers and above.

Thermodynamic modelling of the Env/BanLec interaction was carried out by Martin Galpin. Briefly, the system was modelled as

$$\mathrm{A} \overset{\mathrm{K}_d}{\rightleftharpoons} \mathrm{B}$$
$$\mathrm{A} + \mathrm{B} \overset{\mathrm{K_{Banlec}}}{\rightleftharpoons} \mathrm{AB}$$
$$\mathrm{A}_n\mathrm{B}_n + \mathrm{A} \overset{\mathrm{K_{Env}}}{\rightleftharpoons} \mathrm{A}_{n+1}\mathrm{B}_n$$
$$\mathrm{A}_{n+1}\mathrm{B}_n + \mathrm{B} \overset{\mathrm{K'_{Banlec}}}{\rightleftharpoons} \mathrm{A}_{n+1}\mathrm{B}_{n+1}$$

where A represents Env and B Banlec. From these equilibria, the concentration of each oligomer can be expressed in terms of a combination of equilibrium constants and powers of $[A]$ and $[B]$. Using the fact that the total number of each monomer is conserved, i.e.

$$[A]_0 = [A] + 2[A_2] + [AB] + \sum_{i=m}^{\infty} \sum_{n=m-1}^{m} m[A_m B_n] \tag{5.2}$$

$$[B]_0 = [B] + [AB] + \sum_{i=m}^{\infty} \sum_{n=m-1}^{m} n[A_m B_m] \tag{5.3}$$

where $[A]_0$ and $[B]_0$ are the initial concentrations, we thus obtained two simultaneous equations to solve (numerically) for $[A]$ and $[B]$ in terms of the equilibrium constants and the initial concentrations. Once $[A]$ and $[B]$ are known, the concentrations of all other species follow from the equilibrium conditions.

For the imaging of the α-synuclein aggregation assay, a reduced power density of 45 kW/cm^2 at the sample was used. The camera was run at a frame rate of 100 Hz with no additional time averaging before saving, and a field of view of 12×12 μm^2. 3×3 pixel-binning to a final effective pixel size of 70.3 nm/pixel was applied as usual.

α-synuclein aggregation assays were performed by Joanna Andrecka. CultureWell silicone gaskets (Grace Bio-Labs) were cut and placed onto a freshly cleaned coverslip providing four independent 3050 μl sample chambers on the same substrate. Stock solutions of 1,2-dioleoyl-sn-glycero-3-phosphocholine (DOPC) and 1,2-dioleoyl-sn-glycero-3-phospho-L-serine (DOPS) in chloroform were purchased from Avanti Polar Lipids (Alabaster, AL). The DOPC:DOPS (3:1) mixture was dried to a film, kept under vacuum for at least 1 h and brought to a concentration of 1 mg ml-1 in bilayer buffer (10 mM HEPES, pH 6.8, 200 mM NaCl, 2 mM CaCl2). Using a mini-extruder (Avanti Polar Lipids), the suspension was then forced 21 times through a single membrane with a pore size of 100 nm. SLBs were formed by vesicle fusion inside the chamber on cleaned coverslips that have been passed through a blue flame. After 510 mins incubation, excess vesicles were removed from the chamber by rinsing with 10 mM sodium phosphate buffer, pH 7.0. α-synuclein was provided as a lyophilised powder by Cedric Eichmann and Philipp Selenko, and dissolved in 20 mM sodium phosphate, pH 7.0 to a final concentration of 1-1.5 mM.

Before addition to the SLBs the protein was diluted in sodium phosphate buffer, 10 μl of α-synuclein solution was added to a sample volume of 30 μl, yielding the final reported concentrations, and images recorded for 20 s. As described in the main text, images were divided by a background image from before addition of protein to the bilayer. After identification of each growing aggregate, a model PSF was fit to an 11×11 pixel region centred on the aggregate over time. The contrast was plotted as a function of time, and the initial growth rate was determined by a linear fit for 0.1-1 s of data after addition of α-synuclein, with higher concentrations deviating from linearity more rapidly than lower concentrations.

MSP1D1 mass	Technique	MSP1D1 lipid mass	Exp. MSP1ΔH5 lipid mass			Exp. MSP1ΔH5 nanodisc mass		
			SEC	DLS	EM	SEC	DLS	EM
141.0	MP	93.9	74.6	72.9	67.4	116.6	114.9	109.4
124.0	SEC	76.9	61.1	59.7	55.2	103.1	101.7	97.2
126.0	DLS	78.9	62.7	61.2	56.6	104.7	103.2	98.6
149.5	Native MS	102.4	81.4	79.5	73.5	123.4	121.5	115.5
158.0	NMR	110.9	88.1	86.1	79.6	130.1	128.1	121.6

Table 4.1 Reduction in total mass of nanodisc calculated for a range of measured masses of the MSP1D1 DMPC nanodisc. All values are given in kDa. SEC, DLS and NMR data are from reference 150, and native MS from reference 151

Technique	MSP1D1		MSP1ΔH5		Ratio of lipid areas: MSP1ΔH5/MSP1D1
	D /nm	R_{lo} /nm	D /nm	R_{lo} /nm	
SEC	10.2	4.6	9.2	4.1	0.79
DLS	9.4	4.2	8.4	3.7	0.78
EM	9.5	4.25	8.2	3.6	0.72

Table 4.2 Size comparison for lipid nanodiscs. Reduction in area of lipid bilayer patch in nanodisc with reduction in size of scaffold protein, calculated from reduciton in hydrodynamic diameter as measured by SEC, DL or EM.[150] D = diameter, R_{lo} = radius of lipid-only content assuming the belt protein contributes 0,5 nm to the radius

Composition	Lipid	Percentage	Mass /Da	Average lipid mass /Da	Protein:lipid assembly ratio	Relative mass of lipid content
a*	DMPC	100	677.9	677.9	1:80	1
b	DMPC PC14:1 Cholesterol	40 50 10	677.9 673.9 386.7	646.8	1:73.5	0.877
c	PC14:1 Cholesterol	90 10	673.9 386.7	645.2	1:67	0.797

Table 4.3 Lipid compositions of MSP1D1 nanodiscs, and calculation of relative lipid mass

Mass of MSP1D1	Lipid mass in DMPC nanodisc	Expected lipid mass	Expected nanodisc mass
141.0	93.9	82.3	129.4
124.0	76.9	67.4	114.5
126.0	78.9	69.2	116.3
149.5	102.4	89.8	136.9
158.0	110.9	97.2	144.3

Table 4.4 Composition b predicted masses. All values are given in kDa.

Mass of MSP1D1	Lipid mass in DMPC nanodisc	Expected lipid mass	Expected nanodisc mass
141.0	93.9	74.9	121.9
124.0	76.9	61.3	108.4
126.0	78.9	62.9	110.0
149.5	102.4	81.6	128.7
158.0	110.9	88.4	135.5

Table 4.5 Composition c predicted masses. All values are given in kDa.

Chapter 6

Summary and Outlook

The principal technical development described in this work was the use of numerical aperture filtering with a partially reflective mask in an iSCAT microscope in order to facilitate more sensitive label-free imaging of single molecules. The advantage of this approach is that it circumvents the limitations on sensitivity imposed by detector saturation. For a well-executed iSCAT experiment, the sensitivity is fundamentally limited by the shot noise arising from the detection of photons, and thus collecting more light leads to an improved SNR. In practice, one cannot simply increase the power density, however, as the camera will saturate due to the limited full well capacity, and there is a limit to how fast even a high speed camera will read out a certain number of pixels (meaning one cannot simply run faster or magnify more and then average pixels). Numerical aperture filtering thus not only allows the use of substantially cheaper and more efficient cameras without compromising sensitivity, but also enables dramatic increases in power density compared to previous iSCAT experiments at similar exposure times and thereby improves the acheivable sensitivity.

We have combined this development with an optimised data analysis routine and the realisation that the scattering contrast of protein molecules is roughly proportional to their mass, in order to develop a novel application for iSCAT

that we have termed mass photometry. With this approach, a very simple 'landing assay', in which images are continuously acquired as molecules bind to a clean glass surface, enables the measurement of mass distributions of protein samples under solution conditions and with the use of very little sample. Characterisation in this way achieves roughly 2% mass accuracy, and coincidentally ∼2% precision also, with a mass resolution that can reach as low as 20 kDa FWHM at low mass, but increases with higher mass. We have also shown that mass photometry is in principle applicable to complexes involving other biomolecules including lipids and glycans, although exact quantification of these species remains subject to further investigation, principally reliant on finding well-defined mass standards.

Subsequent to characterising the capabilities of mass photometry, we have illustrated them with an investigation into the BanLec-induced aggregation of Env, a system which has eluded characterisation by other, more established, techniques. We were able to measure mass distributions of this highly heterogeneous system as a function of increasing BanLec concentration, and extract equilibrium constants for the different steps in the aggregation process through appropriate modelling of the observed oligomeric fractions.

We have detailed the image processing and analysis routine used to extract such contrast (and so, indirectly, mass) distributions from the movies of the glass surface, as well as describing a modified routine applicable to assays in which the species of interest move across the surface over time (exemplified with diffusion on a SLB). We have highlighted some points for consideration when acquiring and analysing mass photometry experiments in order to achieve results at the current limits of resolution and repeatability - these included a method to improve the reliability of determining the focus position, and a comparison of the effects of different integration times.

We concluded with a discussion of what currently seem to be the key limitations for mass photometry, namely the possible factors limiting the resolution, precision and sensitivity. Pushing the boundaries of these areas will require further effort to understand these limiting factors, but improvements to any and/or all of them could dramatically broaden the scope of the biochemical investigations possible with this technique.

One option is to take the 'brute force' approach to improving sensitivity and low-mass resolution - find ways of using more power. This is the approach that has thus far been fulfilled by numerical aperture filtering with a partially reflective mask. The reflectivity of this mask cannot be indefinitely increased without running into other troubles such as those arising from very high background contrast of the glass surface and from spurious background from other optical components, and so alternative strategies will be necessary. This general route might be ultimately limited, however, by photo-induced sample damage (even in the absence of a strong absorption). It is possible that this risk could be alleviated somewhat by the use of a different illumination scheme that does not involve a focused beam at the sample, as in the original implementation described in Chapter 3.

An understanding of the extent to which high mass resolution is indeed limited by variations in the amplitude of the reference field will inform future efforts to improve peak width at high mass through software correction. If successful in correcting for this effect, a constant peak width of 20 kDa FWHM would enable oligomerically resolved studies on highly polydisperse small heat shock proteins, for example, or investigations into the assembly of large complexes composed of relatively small subunits. Similarly, effort should be given to determining and removing those factors which limit the shot-to-shot repeatability (precision) of the molecular contrast, in order to truly realise

the possibility of measuring small-molecule binding using mass photometry. Alternatively, it might be possible to get around this limit through the use of an inert standard internal to each measurement as a reference to account for these contrast fluctuations.

In addition to such progress in understanding the fundamental limitations of mass photometry, further exciting experiments may already be possible with the current optical hardware and software through the integration of existing sample delivery and glass functionalisation protocols. More sophisticated fluid handling methods will allow higher throughput and thus more rapid acquisition of very large datasets, and perhaps access to lower concentration regimes. Possible combination with in situ mixing and/or microfluidic techniques may allow kinetic studies of more rapid interactions, for example. Functionalisation of the coverslip surface could provide additional specificity to this otherwise fairly non-specific method, similar to the way in which it has been used for single molecule pull-down assays with fluorescence detection. A similar protocol might enable the monitoring of binding and unbinding events to individual binding partners immobilised on the surface, and thus the direct extraction of on and off rates, in a single-molecule analogue of a typical surface plasmon resonance based binding experiment. We stress at this point that we are just at the very beginning of exploring what it is possible to measure with this technique.

In this work we have simply established the principle of mass photometry and, hopefully, given a flavour of possible applications. While such developments as discussed above will doubtless broaden the appeal of the technique, there is already plenty of scope for exploring the applications that can be achieved with the current capabilities. We have already demonstrated, for example, that mass photometry can be used to measure equilibrium constants for a system

such as the Env/BanLec interaction, and so extending it more generally to quantitative measurements of the energetics of more simple protein-protein interactions would be one avenue worth pursuing. It also seems worthwhile exploring the extent to which one can characterise the behaviour of membrane binding proteins through combination with supported lipid bilayer assays, an application which we have only briefly touched on here. There are doubtless many more specific measurements and applications that will emerge as/if the use of mass photometry becomes more widespread and integrated with other more standard biochemical characterisation techniques.

References

[1] W. E. Moerner and L. Kador, Optical detection and spectroscopy of single molecules in a solid, *Phys Rev Lett*, 1989, **62**, 2535–2538.

[2] M. Orrit and J. Bernard, Single pentacene molecules detected by fluorescence excitation in a p-terphenyl crystal, *Phys Rev Lett*, 1990, **65**, 2716–2719.

[3] K. C. Neuman and S. M. Block, Optical trapping, *Review of Scientific Instruments*, 2004, **75**, 2787–2809.

[4] C. Gosse and V. Croquette, Magnetic tweezers: Micromanipulation and force measurement at the molecular level, *Biophysical Journal*, 2002, **82**, 3314–3329.

[5] T. Uchihashi, N. Kodera and T. Ando, Guide to video recording of structure dynamics and dynamic processes of proteins by high-speed atomic force microscopy, *Nature Protocols*, 2012, **7**, 1193–1206.

[6] R. Y. Tsien, The green fluorescent protein, *Annual Review of Biochemistry*, 1998, **67**, 509–544.

[7] R. M. Dickson, A. B. Cubitt, R. Y. Tsien and W. E. Moerner, On/off blinking and switching behaviour of single molecules of green fluorescent protein, *Nature*, 1997, **388**, 355–358.

[8] S. W. Hell and J. Wichmann, Breaking the diffraction resolution limit by stimulated emission: stimulated-emission-depletion fluorescence microscopy, *Optics Letters*, 1994, **19**, 780.

[9] E. Betzig, G. H. Patterson, R. Sougrat, O. W. Lindwasser, S. Olenych, J. S. Bonifacino, M. W. Davidson, J. Lippincott-Schwartz and H. F. Hess, Imaging intracellular fluorescent proteins at nanometer resolution, *Science*, 2006, **313**, 1642–1645.

[10] M. J. Rust, M. Bates and X. Zhuang, Sub-diffraction-limit imaging by stochastic optical reconstruction microscopy (STORM), *Nature Methods*, 2006, **3**, 793–796.

[11] T. Fujiwara, K. Ritchie, H. Murakoshi, K. Jacobson and A. Kusumi, Phospholipids undergo hop diffusion in compartmentalized cell membrane, *J Cell Biol*, 2002, **157**, 1071–1081.

[12] A. Kusumi, C. Nakada, K. Ritchie, K. Murase, K. Suzuki, H. Murakoshi, R. S. Kasai, J. Kondo and T. Fujiwara, Paradigm shift of the plasma membrane concept from the two-dimensional continuum fluid to the partitioned fluid: High-speed single-molecule tracking of membrane molecules, *Annual Review of Biophysics and Biomolecular Structure*, 2005, **34**, 351–378.

[13] H. Ueno, S. Nishikawa, R. Iino, K. V. Tabata, S. Sakakihara, T. Yanagida and H. Noji, Simple dark-field microscopy with nanometer spatial precision and microsecond temporal resolution, *Biophysical Journal*, 2010, **98**, 2014–2023.

[14] Y. H. Lin, W. L. Chang and C. L. Hsieh, Shot-noise limited localization of single 20 nm gold particles with nanometer spatial precision within microseconds, *Opt Express*, 2014, **22**, 9159–9170.

[15] J. Andrecka, J. Ortega Arroyo, Y. Takagi, G. de Wit, A. Fineberg, L. MacKinnon, G. Young, J. R. Sellers and P. Kukura, Structural dynamics of myosin 5 during processive motion revealed by interferometric scattering microscopy, *Elife*, 2015, **4**, year.

[16] P. Kukura, H. Ewers, C. Muller, A. Renn, A. Helenius and V. Sandoghdar, High-speed nanoscopic tracking of the position and orientation of a single virus, *Nat Methods*, 2009, **6**, 923–927.

[17] J. Andrecka, K. M. Spillane, J. Ortega-Arroyo and P. Kukura, Direct observation and control of supported lipid bilayer formation with interferometric scattering microscopy, *ACS Nano*, 2013, **7**, 10662–10670.

[18] J. Andrecka, J. Ortega-Arroyo, R. Cross and P. Kukura, Label-Free Imaging of Microtubules with Subnanometer Precision using Interferometric Scattering Microscopy, *Biophysical Journal*, 2016, **110**, 131a.

[19] M. Piliarik and V. Sandoghdar, Direct optical sensing of single unlabelled proteins and super-resolution imaging of their binding sites, *Nat Commun*, 2014, **5**, 4495.

[20] J. Ortega Arroyo, J. Andrecka, K. M. Spillane, N. Billington, Y. Takagi, J. R. Sellers and P. Kukura, Label-free, all-optical detection, imaging, and tracking of a single protein, *Nano Lett*, 2014, **14**, 2065–2070.

[21] G. Young and P. Kukura, Interferometric Scattering Microscopy, *Annual Review of Physical Chemistry*, 2019, **70**, 301–322.

[22] R. Hooke, *Micrographia, or, Some physiological descriptions of minute bodies made by magnifying glasses : with observations and inquiries thereupon*, Printed by J. Martyn and J. Allestry, London, 1665, pp. 246 pages, 38 unnumbered leaves of plates (some folded).

[23] Y. Jiang, Z. Chen, Y. Han, P. Deb, H. Gao, S. Xie, P. Purohit, M. W. Tate, J. Park, S. M. Gruner, V. Elser and D. A. Muller, Electron ptychography of 2D materials to deep sub-angstrom resolution, *Nature*, 2018, **559**, 343–349.

[24] W. Neuhauser, M. Hohenstatt, P. E. Toschek and H. Dehmelt, Localized visible Ba+ mono-ion oscillator, *Physical Review A*, 1980, **22**, 1137.

[25] M. E. Kandel, K. W. Teng, P. R. Selvin and G. Popescu, Label-Free Imaging of Single Microtubule Dynamics Using Spatial Light Interference Microscopy, *ACS Nano*, 2017, **11**, 647–655.

[26] L. A. Amos and W. B. Amos, The bending of sliding microtubules imaged by confocal light microscopy and negative stain electron microscopy, *J Cell Sci Suppl*, 1991, **14**, 95–101.

[27] H. Siedentopf and R. Zsigmondy, Uber sichtbarmachung und größenbestimmung ultramikoskopischer teilchen, mit besonderer anwendung auf goldrubingläser, *Annalen der Physik*, 1902, **315**, 1–39.

[28] A. Straube, How to measure microtubule dynamics?, *Methods Mol Biol*, 2011, **777**, 1–14.

[29] E. W. Streed, A. Jechow, B. G. Norton and D. Kielpinski, Absorption imaging of a single atom, *Nat Commun*, 2012, **3**, 933.

[30] C. F. Bohren and D. R. Huffman, *Absorption and scattering of light by small particles*, Wiley, New York, 1983.

[31] F. Zernike, Das Phasenkontrastverfahren bei der mikroskopischen Beobachtung, Z, *Tech. Phys*, 1935, **16**, 454.

[32] G. Nomarski, Microinterferometre dlfferentielie a ondes polarisees, *J. Phys. Radium*, 1955, **16**, 9.

[33] R. D. Allen and G. B. David, The Zeiss-Nomarski differential interference equipment for transmitted-light microscopy, *Zeitschrift fur wissenschaftliche Mikroskopie und mikroskopische Technik*, 1969, **69**, 193–221.

[34] Y. Cotte, F. Toy, P. Jourdain, N. Pavillon, D. Boss, P. Magistretti, P. Marquet and C. Depeursinge, Marker-free phase nanoscopy, *Nature Photonics*, 2013, **7**, 113–117.

[35] T. Kim, R. J. Zhou, M. Mir, S. D. Babacan, P. S. Carney, L. L. Goddard and G. Popescu, White-light diffraction tomography of unlabelled live cells, *Nature Photonics*, 2014, **8**, 256–263.

[36] J. Ortega-Arroyo and P. Kukura, Interferometric scattering microscopy (iSCAT): new frontiers in ultrafast and ultrasensitive optical microscopy, *Phys Chem Chem Phys*, 2012, **14**, 15625–15636.

[37] A. S. Curtis, The Mechanism of Adhesion of Cells to Glass. A Study by Interference Reflection Microscopy, *J Cell Biol*, 1964, **20**, 199–215.

[38] J. S. Ploem, *Reflection-contrast microscopy as a tool for investigation of the attachment of living cells to a glass surface*, Blackwell, Oxford, 1975.

[39] D. Gingell and I. Todd, Interference reflection microscopy. A quantitative theory for image interpretation and its application to cell-substratum separation measurement, *Biophys J*, 1979, **26**, 507–526.

[40] L. Limozin and K. Sengupta, Quantitative reflection interference contrast microscopy (RICM) in soft matter and cell adhesion, *Chemphyschem*, 2009, **10**, 2752–2768.

[41] J. Rädler and E. Sackmann, Imaging optical thicknesses and separation distances of phospholipid vesicles at solid surfaces, *Journal de Physique II*, 1993, **3**, 727–748.

[42] J. Rädler, H. Strey and E. Sackmann, Phenomenology and kinetics of lipid bilayer spreading on hydrophilic surfaces, *Langmuir*, 1995, **11**, 4539–4548.

[43] D. Boyer, P. Tamarat, A. Maali, B. Lounis and M. Orrit, Photothermal imaging of nanometer-sized metal particles among scatterers, *Science*, 2002, **297**, 1160–1163.

[44] K. Lindfors, T. Kalkbrenner, P. Stoller and V. Sandoghdar, Detection and spectroscopy of gold nanoparticles using supercontinuum white light confocal microscopy, *Phys Rev Lett*, 2004, **93**, 37401.

[45] V. Jacobsen, P. Stoller, C. Brunner, V. Vogel and V. Sandoghdar, Interferometric optical detection and tracking of very small gold nanoparticles at a water-glass interface, *Opt Express*, 2006, **14**, 405–414.

[46] H. Ewers, V. Jacobsen, E. Klotzsch, A. E. Smith, A. Helenius and V. Sandoghdar, Label-free optical detection and tracking of single virions bound to their receptors in supported membrane bilayers, *Nano Lett*, 2007, **7**, 2263–2266.

[47] H. Shen, L. J. Tauzin, R. Baiyasi, W. Wang, N. Moringo, B. Shuang and C. F. Landes, Single Particle Tracking: From Theory to Biophysical Applications, *Chem Rev*, 2017, **117**, 7331–7376.

[48] R. E. Thompson, D. R. Larson and W. W. Webb, Precise nanometer localization analysis for individual fluorescent probes, *Biophys J*, 2002, **82**, 2775–2783.

[49] A. Yildiz, J. N. Forkey, S. A. McKinney, T. Ha, Y. E. Goldman and P. R. Selvin, Myosin V walks hand-over-hand: single fluorophore imaging with 1.5-nm localization, *Science*, 2003, **300**, 2061–2065.

[50] B. P. English, V. Hauryliuk, A. Sanamrad, S. Tankov, N. H. Dekker and J. Elf, Single-molecule investigations of the stringent response machinery in living bacterial cells, *Proc Natl Acad Sci U S A*, 2011, **108**, E365–73.

[51] S. Uphoff, R. Reyes-Lamothe, F. Garza de Leon, D. J. Sherratt and A. N. Kapanidis, Single-molecule DNA repair in live bacteria, *Proc Natl Acad Sci U S A*, 2013, **110**, 8063–8068.

[52] F. Balzarotti, Y. Eilers, K. C. Gwosch, A. H. Gynna, V. Westphal, F. D. Stefani, J. Elf and S. W. Hell, Nanometer resolution imaging and tracking of fluorescent molecules with minimal photon fluxes, *Science*, 2017, **355**, 606–612.

[53] T. Kues, R. Peters and U. Kubitscheck, Visualization and tracking of single protein molecules in the cell nucleus, *Biophys J*, 2001, **80**, 2954–2967.

[54] U. Kubitscheck, O. Kuckmann, T. Kues and R. Peters, Imaging and tracking of single GFP molecules in solution, *Biophys J*, 2000, **78**, 2170–2179.

[55] G. Seisenberger, M. U. Ried, T. Endress, H. Buning, M. Hallek and C. Brauchle, Real-time single-molecule imaging of the infection pathway of an adeno-associated virus, *Science*, 2001, **294**, 1929–1932.

[56] A. Yildiz and P. R. Selvin, Fluorescence imaging with one nanometer accuracy: application to molecular motors, *Acc Chem Res*, 2005, **38**, 574–582.

[57] P. Pierobon, S. Achouri, S. Courty, A. R. Dunn, J. A. Spudich, M. Dahan and G. Cappello, Velocity, processivity, and individual steps of single myosin V molecules in live cells, *Biophys J*, 2009, **96**, 4268–4275.

[58] K. M. Trybus, Myosin V from head to tail, *Cellular and Molecular Life Sciences*, 2008, **65**, 1378–1389.

[59] D. M. Warshaw, G. G. Kennedy, S. S. Work, E. B. Krementsova, S. Beck and K. M. Trybus, Differential labeling of myosin V heads with quantum dots allows direct visualization of hand-over-hand processivity, *Biophys J*, 2005, **88**, L30–2.

[60] T. Sakamoto, M. R. Webb, E. Forgacs, H. D. White and J. R. Sellers, Direct observation of the mechanochemical coupling in myosin Va during processive movement, *Nature*, 2008, **455**, 128–132.

[61] A. R. Dunn and J. A. Spudich, Dynamics of the unbound head during myosin V processive translocation, *Nat Struct Mol Biol*, 2007, **14**, 246–248.

[62] K. J. Mickolajczyk, N. C. Deffenbaugh, J. O. Arroyo, J. Andrecka, P. Kukura and W. O. Hancock, Kinetics of nucleotide-dependent structural transitions in the kinesin-1 hydrolysis cycle, *Proc Natl Acad Sci U S A*, 2015, **112**, E7186–93.

[63] J. Andrecka, Y. Takagi, K. J. Mickolajczyk, L. G. Lippert, J. R. Sellers, W. O. Hancock, Y. E. Goldman and P. Kukura, Interferometric Scattering Microscopy for the Study of Molecular Motors, *Methods Enzymol*, 2016, **581**, 517–539.

[64] K. M. Spillane, J. Ortega-Arroyo, G. de Wit, C. Eggeling, H. Ewers, M. I. Wallace and P. Kukura, High-speed single-particle tracking of GM1 in model membranes reveals anomalous diffusion due to interleaflet coupling and molecular pinning, *Nano Lett*, 2014, **14**, 5390–5397.

[65] S. Spindler, J. Ehrig, K. Konig, T. Nowak, M. Piliarik, H. E. Stein, R. W. Taylor, E. Garanger, S. Lecommandoux, I. D. Alves and V. Sandoghdar, Visualization of lipids and proteins at high spatial and temporal resolution via interferometric scattering (iSCAT) microscopy, *Journal of Physics D-Applied Physics*, 2016, **49**, year.

[66] H. M. Wu, Y. H. Lin, T. C. Yen and C. L. Hsieh, Nanoscopic substructures of raft-mimetic liquid-ordered membrane domains revealed by high-speed single-particle tracking, *Sci Rep*, 2016, **6**, 20542.

[67] H. Isojima, R. Iino, Y. Niitani, H. Noji and M. Tomishige, Direct observation of intermediate states during the stepping motion of kinesin-1, *Nat Chem Biol*, 2016, **12**, 290–297.

[68] G. de Wit, D. Albrecht, H. Ewers and P. Kukura, Revealing Compartmentalized Diffusion in Living Cells with Interferometric Scattering Microscopy, *Biophys J*, 2018, **114**, 2945–2950.

[69] K. Xu, G. Zhong and X. Zhuang, Actin, spectrin, and associated proteins form a periodic cytoskeletal structure in axons, *Science*, 2013, **339**, 452–456.

[70] R. W. Taylor, R. G. Mahmoodabadi, V. Rauschenberger, A. Giessl, A. Schambony and V. Sandoghdar, Interferometric scattering microscopy reveals microsecond nanoscopic protein motion on a live cell membrane, *Nature Photonics*, 2019, **13**, 480–487.

[71] Y. F. Huang, G. Y. Zhuo, C. Y. Chou, C. H. Lin and C. L. Hsieh, Label-free, ultrahigh-speed, 3D observation of bidirectional and correlated intracellular cargo transport by coherent brightfield microscopy, *Nanoscale*, 2017, **9**, 6567–6574.

[72] Y. F. Huang, G. Y. Zhuo, C. Y. Chou, C. H. Lin, W. Chang and C. L. Hsieh, Coherent Brightfield Microscopy Provides the Spatiotemporal Resolution To Study Early Stage Viral Infection in Live Cells, *ACS Nano*, 2017, **11**, 2575–2585.

[73] C.-Y. Cheng and C.-L. Hsieh, Background Estimation and Correction for High-Precision Localization Microscopy, *ACS Photonics*, 2017, **4**, 1730–1739.

[74] H. P. Erickson, Size and Shape of Protein Molecules at the Nanometer Level Determined by Sedimentation, Gel Filtration, and Electron Microscopy, *Biological Procedures Online*, 2009, **11**, 32–51.

[75] G. de Wit, J. S. Danial, P. Kukura and M. I. Wallace, Dynamic label-free imaging of lipid nanodomains, *Proc Natl Acad Sci U S A*, 2015, **112**, 12299–12303.

[76] S. L. Veatch and S. L. Keller, Seeing spots: complex phase behavior in simple membranes, *Biochim Biophys Acta*, 2005, **1746**, 172–185.

[77] C. Dietrich, L. A. Bagatolli, Z. N. Volovyk, N. L. Thompson, M. Levi, K. Jacobson and E. Gratton, Lipid rafts reconstituted in model membranes, *Biophys J*, 2001, **80**, 1417–1428.

[78] T. Baumgart, A. T. Hammond, P. Sengupta, S. T. Hess, D. A. Holowka, B. A. Baird and W. W. Webb, Large-scale fluid/fluid phase separation of proteins and lipids in giant plasma membrane vesicles, *Proc Natl Acad Sci U S A*, 2007, **104**, 3165–3170.

[79] M. de Frutos, L. Letellier and E. Raspaud, DNA ejection from bacteriophage T5: analysis of the kinetics and energetics, *Biophys J*, 2005, **88**, 1364–1370.

[80] A. M. Goldfain, R. F. Garmann, Y. Jin, Y. Lahini and V. N. Manoharan, Dynamic Measurements of the Position, Orientation, and DNA Content of Individual Unlabeled Bacteriophages, *J Phys Chem B*, 2016, **120**, 6130–6138.

[81] P. Grayson, L. Han, T. Winther and R. Phillips, Real-time observations of single bacteriophage lambda DNA ejections in vitro, *Proc Natl Acad Sci U S A*, 2007, **104**, 14652–14657.

[82] R. F. Garmann, A. M. Goldfain and V. N. Manoharan, Measurements of the self-assembly kinetics of individual viral capsids around their RNA genome, *Proceedings of the National Academy of Sciences of the United States of America*, 2019, **116**, 22485–22490.

[83] M. Celebrano, P. Kukura, A. Renn and V. Sandoghdar, Single-molecule imaging by optical absorption, *Nature Photonics*, 2011, **5**, 95.

[84] P. Kukura, M. Celebrano, A. Renn and V. Sandoghdar, Single-Molecule Sensitivity in Optical Absorption at Room Temperature, *Journal of Physical Chemistry Letters*, 2010, **1**, 3323–3327.

[85] A. Gaiduk, M. Yorulmaz, P. V. Ruijgrok and M. Orrit, Room-temperature detection of a single molecule's absorption by photothermal contrast, *Science*, 2010, **330**, 353–356.

[86] S. Chong, W. Min and X. S. Xie, Ground-state depletion microscopy: detection sensitivity of single-molecule optical absorption at room temperature, *The Journal of Physical Chemistry Letters*, 2010, **1**, 3316–3322.

[87] L. Rayleigh, XXXIV. On the transmission of light through an atmosphere containing small particles in suspension, and on the origin of the blue of the sky , *The London, Edinburgh, and Dublin Philosophical Magazine and Journal of Science*, 1899, **47**, 375–384.

[88] G. Mie, Beiträge zur Optik trüber Medien, speziell kolloidaler Metallösungen, *Annalen der Physik*, 1908, **330**, 377–445.

[89] P. Laven, Simulation of rainbows, coronas, and glories by use of Mie theory, *Applied Optics*, 2003, **42**, 436.

[90] J. Ortega Arroyo, D. Cole and P. Kukura, Interferometric scattering microscopy and its combination with single-molecule fluorescence imaging, *Nature Protocols*, 2016, **11**, 617–633.

[91] S. R. P. Pavani, M. A. Thompson, J. S. Biteen, S. J. Lord, N. Liu, R. J. Twieg, R. Piestun and W. E. Moerner, Three-dimensional, single-molecule fluorescence imaging beyond the diffraction limit by using a double-helix point spread function, *Proceedings of the National Academy of Sciences of the United States of America*, 2009, **106**, 2995–2999.

[92] Y. Shechtman, L. E. Weiss, A. S. Backer, S. J. Sahl and W. E. Moerner, Precise Three-Dimensional Scan-Free Multiple-Particle Tracking over Large Axial Ranges with Tetrapod Point Spread Functions, *Nano Letters*, 2015, **15**, 4194–4199.

[93] Y. Shechtman, L. E. Weiss, A. S. Backer, M. Y. Lee and W. E. Moerner, Multicolour localization microscopy by point-spread-function engineering, *Nature Photonics*, 2016, **10**, 590–594.

[94] R. Diekmann, K. Till, M. Müller, M. Simonis, M. Schüttpelz and T. Huser, Characterization of an industry-grade CMOS camera well suited for single molecule localization microscopy - High performance super-resolution at low cost, *Scientific Reports*, 2017, **7**, 1–10.

[95] I. Smal, M. Loog, W. Niessen and E. Meijering, Quantitative Comparison of Spot Detection Methods in Fluorescence Microscopy, *IEEE Transactions on Medical Imaging*, 2010, **29**, 282–301.

[96] D. Sage, F. Neumann, F. Hediger, S. Gasser and M. Unser, Automatic tracking of individual fluorescence particles: application to the study of chromosome dynamics, *IEEE Transactions on Image Processing*, 2005, **14**, 1372–1383.

[97] H. Kong, H. C. Akakin and S. E. Sarma, A Generalized Laplacian of Gaussian Filter for Blob Detection and Its Applications, *IEEE Transactions on Cybernetics*, 2013, **43**, 1719–1733.

[98] L. Yang, R. Parton, G. Ball, Z. Qiu, A. H. Greenaway, I. Davis and W. Lu, An adaptive non-local means filter for denoising live-cell images and improving particle detection, *Journal of Structural Biology*, 2010, **172**, 233–243.

[99] D. Thomann, D. R. Rines, P. K. Sorger and G. Danuser, Automatic fluorescent tag detection in 3D with super-resolution: application to the analysis of chromosome movement, *Journal of Microscopy*, 2002, **208**, 49–64.

[100] S. Stallinga and B. Rieger, Accuracy of the Gaussian Point Spread Function model in 2D localization microscopy, *Optics Express*, 2010, **18**, 24461.

[101] G. Young, N. Hundt, D. Cole, A. Fineberg, J. Andrecka, A. Tyler, A. Olerinyova, A. Ansari, E. G. Marklund, M. P. Collier, S. A. Chandler, O. Tkachenko, J. Allen, M. Crispin, N. Billington, Y. Takagi, J. R. Sellers, C. Eichmann, P. Selenko, L. Frey, R. Riek, M. R. Galpin, W. B. Struwe, J. L. P. Benesch and P. Kukura, Quantitative mass imaging of single biological macromolecules, *Science*, 2018, **360**, 423–427.

[102] R. Machá and M. Hof, Lipid diffusion in planar membranes investigated by fluorescence correlation spectroscopy, *Biochimica et Biophysica Acta (BBA) - Biomembranes*, 2010, **1798**, 1377–1391.

[103] M. Rose, N. Hirmiz, J. Moran-Mirabal and C. Fradin, Lipid Diffusion in Supported Lipid Bilayers: A Comparison between Line-Scanning Fluorescence Correlation Spectroscopy and Single-Particle Tracking, *Membranes*, 2015, **5**, 702–721.

[104] D. B. Allan, T. Caswell, N. C. Keim and C. M. van der Wel, *Trackpy v0.4.1*.

[105] J. C. Crocker and D. G. Grier, Methods of Digital Video Microscopy for Colloidal Studies, *Journal of Colloid and Interface Science*, 1996, **179**, 298–310.

[106] G. Schütz, H. Schindler and T. Schmidt, Single-molecule microscopy on model membranes reveals anomalous diffusion, *Biophysical Journal*, 1997, **73**, 1073–1080.

[107] Y. Chen, B. C. Lagerholm, B. Yang and K. Jacobson, Methods to measure the lateral diffusion of membrane lipids and proteins, *Methods*, 2006, **39**, 147–153.

[108] L. Guo, J. Y. Har, J. Sankaran, Y. Hong, B. Kannan and T. Wohland, Molecular Diffusion Measurement in Lipid Bilayers over Wide Concentration Ranges: A Comparative Study, *ChemPhysChem*, 2008, **9**, 721–728.

[109] A. Jain, R. Liu, B. Ramani, E. Arauz, Y. Ishitsuka, K. Ragunathan, J. Park, J. Chen, Y. K. Xiang and T. Ha, Probing cellular protein complexes using single-molecule pull-down, *Nature*, 2011, **473**, 484–488.

[110] C. Macias-Romero, I. Nahalka, H. I. Okur and S. Roke, Optical imaging of surface chemistry and dynamics in confinement., *Science (New York, N.Y.)*, 2017, **357**, 784–788.

[111] N. A. C. Cressie, *Statistics for Spatial Data*, John Wiley & Sons, Inc., Hoboken, NJ, USA, 1993.

[112] N. Chenouard, I. Smal, F. de Chaumont, M. Maška, I. F. Sbalzarini, Y. Gong, J. Cardinale, C. Carthel, S. Coraluppi, M. Winter, A. R. Cohen, W. J. Godinez, K. Rohr, Y. Kalaidzidis, L. Liang, J. Duncan, H. Shen, Y. Xu, K. E. G. Magnusson, J. Jaldén, H. M. Blau, P. Paul-Gilloteaux, P. Roudot, C. Kervrann, F. Waharte, J.-Y. Tinevez, S. L. Shorte, J. Willemse, K. Celler, G. P. van Wezel, H.-W. Dan, Y.-S. Tsai, C. O. de Solórzano, J.-C. Olivo-Marin and E. Meijering, Objective comparison of particle tracking methods, *Nature Methods*, 2014, **11**, 281–289.

[113] K. Häußermann, G. Young, P. Kukura and H. Dietz, Dissecting FOXP2 Oligomerization and DNA Binding, *Angewandte Chemie*, 2019, **131**, 7744–7749.

[114] E. A. Abbondanzieri, W. J. Greenleaf, J. W. Shaevitz, R. Landick and S. M. Block, Direct observation of base-pair stepping by RNA polymerase, *Nature*, 2005, **438**, 460–465.

[115] D. Cole, G. Young, A. Weigel, A. Sebesta and P. Kukura, Label-Free Single-Molecule Imaging with Numerical-Aperture-Shaped Interferometric Scattering Microscopy, *ACS Photonics*, 2017, **4**, 211–216.

[116] J. O. Arroyo and P. Kukura, Non-fluorescent schemes for single-molecule detection, imaging and spectroscopy, *Nature Photonics*, 2016, **10**, 11–17.

[117] M. A. Lieb, J. M. Zavislan and L. Novotny, Single-molecule orientations determined by direct emission pattern imaging, *Journal of the Optical Society of America B: Optical Physics*, 2004, **21**, 1210–1215.

[118] X. Brokmann, L. Coolen, J.-P. Hermier and M. Dahan, Emission properties of single CdSe/ZnS quantum dots close to a dielectric interface, *Chemical Physics*, 2005, **318**, 91–98.

[119] K. G. Lee, X. W. Chen, H. Eghlidi, P. Kukura, R. Lettow, A. Renn, V. Sandoghdar and S. Götzinger, A planar dielectric antenna for directional single-photon emission and near-unity collection efficiency, *Nature Photonics*, 2011, **5**, 166–169.

[120] Y. Sowa, B. C. Steel and R. M. Berry, A simple backscattering microscope for fast tracking of biological molecules, *Review of Scientific Instruments*, 2010, **81**, year.

[121] A. Weigel, A. Sebesta and P. Kukura, Dark Field Microspectroscopy with Single Molecule Fluorescence Sensitivity, *ACS Photonics*, 2014, **1**, 848–856.

[122] K. Goto and Y. Hayasaki, Three-dimensional motion detection of a 20-nm gold nanoparticle using twilight-field digital holography with coherence regulation, *Optics Letters*, 2015, **40**, 3344–3347.

[123] Q. D. Pham, Y. Kusumi, S. Hasegawa and Y. Hayasaki, Digital holographic microscope with low-frequency attenuation filter for position measurement of a nanoparticle, *Optics Letters*, 2012, **37**, 4119–4121.

[124] J. Hwang and W. E. Moerner, Interferometry of a single nanoparticle using the Gouy phase of a focused laser beam, *Optics Communications*, 2007, **280**, 487–491.

[125] K. K. Kim, R. Kim and S.-H. Kim, Crystal structure of a small heat-shock protein, *Nature*, 1998, **394**, 595–599.

[126] I. De Vlaminck and C. Dekker, Recent Advances in Magnetic Tweezers, *Annual Review of Biophysics*, 2012, **41**, 453–472.

[127] R. R. Ishmukhametov, A. N. Russell, R. J. Wheeler, A. L. Nord and R. M. Berry, A Simple low-cost device enables four epi-illumination techniques on standard light microscopes, *Scientific Reports*, 2016, **6**, year.

[128] C. Boozer, G. Kim, S. Cong, H. Guan and T. Londergan, Looking towards label-free biomolecular interaction analysis in a high-throughput format: a review of new surface plasmon resonance technologies, *Current Opinion in Biotechnology*, 2006, **17**, 400–405.

[129] R. Walder, D. H. Paik, M. S. Bull, C. Sauer and T. T. Perkins, Ultra-stable measurement platform: Sub-nm drift over hours in 3d at room temperature, *Optics Express*, 2015, **23**, 16554–16564.

[130] S. E. Ahnert, J. A. Marsh, H. Hernández, C. V. Robinson and S. A. Teichmann, Principles of assembly reveal a periodic table of protein complexes, *Science*, 2015, **350**, year.

[131] K. Rottner, J. Faix, S. Bogdan, S. Linder and E. Kerkhoff, Actin assembly mechanisms at a glance, *Journal of Cell Science*, 2017, **130**, 3427–3435.

[132] M. Hemmat, B. T. Castle and D. J. Odde, Microtubule dynamics: moving toward a multi-scale approach, *Current Opinion in Cell Biology*, 2018, **50**, 8–13.

[133] H.-W. Wang and J.-W. Wang, How cryo-electron microscopy and X-ray crystallography complement each other, *Protein Science*, 2017, **26**, 32–39.

[134] A. J. Heck, Native mass spectrometry: A bridge between interactomics and structural biology, *Nature Methods*, 2008, **5**, 927–933.

[135] D. M. Kanno and M. Levitus, Protein oligomerization equilibria and kinetics investigated by fluorescence correlation spectroscopy: A mathematical treatment, *Journal of Physical Chemistry B*, 2014, **118**, 12404–12415.

[136] M. Chakraborty, A. M. Kuriata, J. Nathan Henderson, M. E. Salvucci, R. M. Wachter and M. Levitus, Protein oligomerization monitored by fluorescence fluctuation spectroscopy: Self-assembly of rubisco activase, *Biophysical Journal*, 2012, **103**, 949–958.

[137] S. I. A. Cohen, M. Vendruscolo, C. M. Dobson and T. P. J. Knowles, From macroscopic measurements to microscopic mechanisms of protein aggregation, *Journal of Molecular Biology*, 2012, **421**, 160–171.

[138] C. Arndt, S. Koristka, H. Bartsch and M. Bachmann, in *Protein Electrophoresis: Methods and Protocols*, ed. B. T. Kurien and R. H. Scofield, Humana Press, Totowa, NJ, 2012, pp. 49–53.

[139] B. Schuler and W. A. Eaton, Protein folding studied by single-molecule FRET, *Current Opinion in Structural Biology*, 2008, **18**, 16–26.

[140] W. J. Greenleaf, M. T. Woodside and S. M. Block, High-resolution, single-molecule measurements of biomolecular motion, *Annual Review of Biophysics and Biomolecular Structure*, 2007, **36**, 171–190.

[141] T. L. McMeekin, M. Wilensky and M. L. Groves, Refractive indices of proteins in relation to amino acid composition and specific volume, *Biochemical and Biophysical Research Communications*, 1962, **7**, 151–156.

[142] Y. Harpaz, M. Gerstein and C. Chothia, Volume changes on protein folding, *Structure*, 1994, **2**, 641–649.

[143] M. Liebel, J. T. Hugall and N. F. van Hulst, Ultrasensitive Label-Free Nanosensing and High-Speed Tracking of Single Proteins, *Nano Lett*, 2017, **17**, 1277–1281.

[144] E. G. Marklund, M. T. Degiacomi, C. V. Robinson, A. J. Baldwin and J. L. P. Benesch, Collision cross sections for structural proteomics, *Structure*, 2015, **23**, 791–799.

[145] K. Nakanishi, T. Sakiyama and K. Imamura, On the adsorption of proteins on solid surfaces, a common but very complicated phenomenon, *Journal of Bioscience and Bioengineering*, 2001, **91**, 233–244.

[146] P. C. Weber, J. J. Wendoloski, M. W. Pantoliano and F. R. Salemme1, Crystallographic and Thermodynamic Comparison of Natural and Synthetic Ligands Bound to Streptavidin, *J. Am. Chem. Soc*, 1992, **114**, 3197–3200.

[147] J. P. Overington, B. Al-Lazikani and A. L. Hopkins, How many drug targets are there?, *Nature Reviews Drug Discovery*, 2006, **5**, 993–996.

[148] I. G. Denisov and S. G. Sligar, Nanodiscs in Membrane Biochemistry and Biophysics, *Chemical Reviews*, 2017, **117**, 4669–4713.

[149] I. G. Denisov, Y. V. Grinkova, A. A. Lazarides and S. G. Sligar, Directed Self-Assembly of Monodisperse Phospholipid Bilayer Nanodiscs with Controlled Size, *J Am Chem Soc*, 2004, 3477–3487.

[150] F. Hagn, M. Etzkorn, T. Raschle and G. Wagner, Optimized phospholipid bilayer nanodiscs facilitate high-resolution structure determination of membrane proteins, *Journal of the American Chemical Society*, 2013, **135**, 1919–1925.

[151] M. T. Marty, H. Zhang, W. Cui, R. E. Blankenship, M. L. Gross and S. G. Sligar, Native mass spectrometry characterization of intact nanodisc lipoprotein complexes, *Analytical Chemistry*, 2012, **84**, 8957–8960.

[152] S. Bibow, Y. Polyhach, C. Eichmann, C. N. Chi, J. Kowal, S. Albiez, R. A. McLeod, H. Stahlberg, G. Jeschke, P. Güntert and R. Riek, Solution structure of discoidal high-density lipoprotein particles with a shortened apolipoprotein A-I, *Nature Structural and Molecular Biology*, 2017, **24**, 187–193.

[153] L. A. Lasky, J. E. Groopman, C. W. Fennie, P. M. Benz, D. J. Capon, D. J. Dowbenko, G. R. Nakamura, W. M. Nunes, M. E. Renz and P. W. Berman, Neutralization of the AIDS retrovirus by antibodies to a recombinant envelope glycoprotein, *Science*, 1986, **233**, 209–212.

[154] W. B. Struwe, A. Stuckmann, A.-J. Behrens, K. Pagel and M. Crispin, Global N-Glycan Site Occupancy of HIV-1 gp120 by Metabolic Engineering and High-Resolution Intact Mass Spectrometry, *ACS Chemical Biology*, 2017, **12**, 357–361.

[155] L. Cao, J. K. Diedrich, D. W. Kulp, M. Pauthner, L. He, S.-K. Park, D. Sok, C. Y. Su, C. M. Delahunty, S. Menis, R. Andrabi, J. Guenaga, E. Georgeson, M. Kubitz, Y. Adachi, D. R. Burton, W. R. Schief, J. R. Yates and J. C. Paulson, Global site-specific N-glycosylation analysis of HIV envelope glycoprotein, *Nature Communications*, 2017, **8**, year.

[156] M. D. Swanson, H. C. Winter, I. J. Goldstein and D. M. Markovitz, A lectin isolated from bananas is a potent inhibitor of HIV replication, *J Biol Chem*, 2010, **285**, 8646–8655.

[157] J. T. S. Hopper, S. Ambrose, O. C. Grant, S. A. Krumm, T. M. Allison, M. T. Degiacomi, M. D. Tully, L. K. Pritchard, G. Ozorowski, A. B. Ward, M. Crispin, K. J. Doores, R. J. Woods, J. L. P. Benesch, C. V. Robinson and W. B. Struwe, The Tetrameric Plant Lectin BanLec Neutralizes HIV through Bidentate Binding to Specific Viral Glycans, *Structure*, 2017, **25**, 773–782 e5.

[158] S. Lusvarghi, K. Lohith, J. Morin-Leisk, R. Ghirlando, J. E. Hinshaw and C. A. Bewley, Binding Site Geometry and Subdomain Valency Control Effects of Neutralizing Lectins on HIV-1 Viral Particles, *ACS Infect Dis*, 2016, **2**, 882–891.

[159] C. Galvagnion, A. K. Buell, G. Meisl, T. C. T. Michaels, M. Vendruscolo, T. P. J. Knowles and C. M. Dobson, Lipid vesicles trigger α-synuclein aggregation by stimulating primary nucleation, *Nature Chemical Biology*, 2015, **11**, 229–234.

[160] A. Iyer, N. Schilderink, M. Claessens and V. Subramaniam, Membrane-Bound Alpha Synuclein Clusters Induce Impaired Lipid Diffusion and Increased Lipid Packing, *Biophysical Journal*, 2016, **111**, 2440–2449.

[161] H. Naiki, K. Higuchi, M. Hosokawa and T. Takeda, Fluorometric determination of amyloid fibrils in vitro using the fluorescent dye, thioflavine T, *Analytical Biochemistry*, 1989, **177**, 244–249.

[162] C. Xue, T. Y. Lin, D. Chang and Z. Guo, Thioflavin T as an amyloid dye: fibril quantification, optimal concentration and effect on aggregation, *Royal Society open science*, 2017, **4**, 160696.

[163] C. M. Pickart and M. J. Eddins, Ubiquitin: structures, functions, mechanisms, *Biochimica et Biophysica Acta (BBA) - Molecular Cell Research*, 2004, **1695**, 55–72.

[164] B. Hua, K. Y. Han, R. Zhou, H. Kim, X. Shi, S. C. Abeysirigunawardena, A. Jain, D. Singh, V. Aggarwal, S. A. Woodson and T. Ha, An improved surface passivation method for single-molecule studies, *Nature Methods*, 2014, **11**, 1233–1236.

[165] Y. Zhang, A. K. Buell, T. Müller, E. DeGenst, J. Benesch, C. M. Dobson and T. P. J. Knowles, Protein Aggregate-Ligand Binding Assays Based on Microfluidic Diffusional Separation, *ChemBioChem*, 2016, **17**, 1920–1924.

[166] J. Charmet, P. Arosio and T. P. Knowles, Microfluidics for Protein Biophysics, *Journal of Molecular Biology*, 2018, **430**, 565–580.

[167] M. Woody, J. Lewis, M. Greenberg, Y. Goldman and E. Ostap, MEMLET: An Easy-to-Use Tool for Data Fitting and Model Comparison Using Maximum-Likelihood Estimation, *Biophysical Journal*, 2016, **111**, 273–282.

[168] N. Billington, A. Wang, J. Mao, R. S. Adelstein and J. R. Sellers, Characterization of Three Full-length Human Nonmuscle Myosin II Paralogs, *Journal of Biological Chemistry*, 2013, 33398–33410.

[169] J. R. Sellers, M. D. Pato and R. S. Adelstein, Reversible Phosphorylation of Smooth Muscle Myosin, Heavy Meromyosin, and Platelet Myosin, *Journal of Biological Chemistry*, 1981, **256**, 13137–13142.

[170] C. Tzitzilonis, C. Eichmann, I. Maslennikov, S. Choe and R. Riek, Detergent/Nanodisc Screening for High-Resolution NMR Studies of an Integral Membrane Protein Containing a Cytoplasmic Domain, *PLoS ONE*, 2013, **8**, e54378.

[171] R. W. Sanders, R. Derking, A. Cupo, J.-P. Julien, A. Yasmeen, N. de Val, H. J. Kim, C. Blattner, A. T. de la Peña, J. Korzun, M. Golabek, K. de los Reyes, T. J. Ketas, M. J. van Gils, C. R. King, I. A. Wilson, A. B. Ward, P. J. Klasse and J. P. Moore, A Next-Generation Cleaved, Soluble HIV-1 Env Trimer, BG505 SOSIP.664 gp140, Expresses Multiple Epitopes for Broadly Neutralizing but Not Non-Neutralizing Antibodies, *PLoS Pathogens*, 2013, **9**, e1003618.